A NEW ATOMIZATION PARADIGM: SMART WAVE-AUGMENTED VARICOSE EXPLOSIONS

A Dissertation
Presented to
the Faculty of
Liberty University

In Partial Fulfillment
of the Requirements for the Degree
Doctor of Philosophy
Engineering

---

by
Daniel Wilson
May 2023

Committee:
Dr. Wayne Strasser, P.E., Committee Chair
Dr. Thomas Eldredge
Dr. Andrew McIntosh
Dr. Yue Ling

ABSTRACT

The characterization of viscous, non-Newtonian slurry heating and atomization by means of internal wave excitation is presented for a twin-fluid injector. We detail mechanisms that enhance their disintegration in a novel process called “Wave-Augmented Varicose Explosions” (WAVE). Atomization of such fluids is challenging, especially at low gas-liquid mass ratios. Droplet production is further complicated when slurry viscosity varies widely; if viscosity levels are too high, atomization quality suffers, and an undesirable pressure drop restricts the flow. To mitigate, we introduce and demonstrate “Smart” atomization, a novel implementation of simultaneous proportional integral derivative (PID) control algorithms to accommodate dynamically and extensively changing fluid properties. Unlike a conventional twin-fluid injector, WAVE injects a cold annular slurry flow into a hot core steam flow, encouraging regular slurry waves to form inside the nozzle and producing bulk system pulsation at 1000 Hz. The Kelvin-Helmholtz instability dominates during wave formation, while transonic pressure effects dominate during wave collapse. Numerical simulations reveal three atomization mechanisms that are a direct result of wave formation: 1) wave impact momentum, 2) pressure buildup, and 3) droplet breakaway. The first two are the forces that exploit slurry irregularities to drive rupture. The third occurs as rising waves penetrate the central steam flow and droplets are stripped off. Two effervescent mechanisms are also provided as 1) surface deformation allows steam fingers to force through the wave, and 2) the wave collapses on itself, trapping steam. Both Rayleigh-Taylor and Kelvin-Helmholtz instabilities are self-amplified in a viscosity-shear-temperature instability cycle because the slurry’s viscosity is sensitive to both strain and temperature. Smart atomization is applied to the WAVE framework with two coupled PID controllers to improve atomization robustness. The first controller automates slurry flow based on atomizer pressure drop, while the second compensates for the newly adjusted phase momentum ratio and sets a new steam flow based on droplet size. Three tests with increasingly rigorous models were conducted to capture the response of this coupled controller system to a step increase in viscosity. Though atomization characteristics were drastically altered, for a 100-fold increase in slurry viscosity, the controllers successfully maintained consistent droplet size and slurry flow resistance.

DEDICATION

I dedicate this dissertation to my bride, Abby, my sons Thaddeus and Malachi, and Jesus Christ, King of the Universe.

ACKNOWLEDGMENTS

I thank God, creator of all things, whose world I have the privilege to study.

I thank my bride, Abby, who has been my constant and dearest companion throughout my graduate studies, and my sons, Thaddeus and Malachi, who bring life through their smiles and show me an enchanted view of the world. I also thank my parents, John and Tina, my twin brother Phillip, and my grandmother Sue for their frequent encouragement and support.

I thank my advisor, Dr. Wayne Strasser, for his constant communication, support, guidance throughout my PhD studies. Reid Prichard has also been instrumental for this work, creating multiple high-quality figures and animations to visualize my simulations. My committee members, Dr. Tom Eldredge, Dr. Andy McIntosh, and Dr. Stanley Ling have provided valuable feedback for betterment of my research.

I thank my family at the Church of the Good Shepherd, who has anchored me, prayed for me, and spurred me on in my PhD studies.

Finally, I thank my fellow graduate students here at Liberty for their encouragement and friendship. The many lunches, walks, and office conversations refreshed my spirit and gave me inspiration in my research.

TABLE OF CONTENTS

Page

ABSTRACT....................i

DEDICATION....................iii

ACKNOWLEDGMENTS....................iv

LIST OF TABLES....................vii

LIST OF FIGURES....................viii

CHAPTER

I. INTRODUCTION....................1

II. THE RISE AND FALL OF BANANA PUREE: NON-NEWTONIAN ANNULAR WAVE FORMATION BY TRANSONIC SELF-PULSATING FLOW....................3

- 2.1 Introduction....................3
- 2.2 Methods....................6
  - 2.2.1 Computational Methods....................6
  - 2.2.2 Mesh and Boundary Conditions....................9
- 2.3 Results and Discussion....................14
  - 2.3.1 Wave Cycle Overview....................14
  - 2.3.2 Mesh Independence....................18
  - 2.3.3 Wave Mechanisms....................22
  - 2.3.4 Wave Feedback....................29
  - 2.3.5 Effect of Turbulence....................32
- 3.4 Conclusion....................34

III. A SPRAY OF PUREE: WAVE-AUGMENTED TRANSONIC AIBLAST NON-NEWTONIAN ATOMIZATION....................36

- 3.1 Introduction....................36
- 3.2 Methods....................39
  - 3.2.1 Computational Methods....................39
  - 3.2.2 Mesh and Boundary Conditions....................41
- 3.3 Results and Discussion....................43
  - 3.3.1 Pulsation Characteristics....................43

3.3.2 Atomization Mechanisms 49
3.3.3 Droplet Sizes 54
3.4 Conclusion 57

IV. SPATIOTEMPORAL CHARACTERIZATION OF WAVE-AUGMENTED VARICOSE EXPLOSIONS 60

4.1 Introduction..60
4.2 Methods..64
4.2.1 Computational Methods 64
4.2.2 Mesh and Boundary Conditions..67
4.3 Results and Discussion 70
4.3.1 3D Wave Cycle 70
4.3.2 Droplet Production..78
4.3.3 Point Monitors 84
4.3.4 Adaptive Mesh Refinement 96
4.4 Conclusion 99

V. 'SMART' TRANSONIC VISCOUS LIQUID SHEET HEATING AND DISINTEGRATION..102

5.1 Introduction..102
5.2 Methods..106
5.2.1 Computational Methods 106
5.2.2 PID Control Algorithm Implementation 108
5.2.3 Smart Atomization Test Descriptions 112
5.3 Results and Discussion 115
5.3.1 Test 1...115
5.3.2 Test 2...120
5.3.3 Test 3...123
5.4 Conclusion 131

VI. CONCLUSION..133

REFERENCES 137

LIST OF TABLES

Table Page

Table 2.1 Parameters describing the geometric and flow conditions of the atomizer nozzle. 12

Table 2.2 Mesh size, hardware, and run time (numerics are consistent across models). . 12

Table 4.1 Mean and coefficient of variation (COV) for signals across all five azimuthal angles at the Exit point. 86

Table 4.2 Mean and coefficient of variation (COV) for signals across all point monitors at the 22.5° azimuthal angle. 88

Table 5.1 Summary of setup and differences between the three Smart tests. 115

Table 5.2 Descriptive statistics for SMD and pressure in Test 1 presented as the ratio of a value after the 100x slurry viscosity change to that before the viscosity change (excluding transition regions). 118

Table 5.3 Descriptive statistics for SMD and pressure in Test 2 presented as the ratio of a value after the 100x slurry viscosity change to that before the viscosity change (excluding transition regions). 122

Table 5.4 Dimensionless numbers describing the flow before the viscosity increase (start) and at the end of Test 3. 127

LIST OF FIGURES

Figure Page

Figure 2.1 Isometric view of Ref-3 surface mesh for the pre-filming (wave formation) region of our twin-fluid atomizer. 13

Figure 2.2 Side view of meshes with increasing levels of refinement. 13

Figure 2.3 Side view of the Ref-3-AMR mesh, illustrating the nature of adaptive mesh refinement. 13

Figure 2.4 Sequential side views of banana puree (yellow) through one predominantly 2D wave cycle for the Ref-3 mesh. 15

Figure 2.5 Side view of predominantly 2D banana puree wave a) as it crests and b) after it collapses (where a new wave forms) with major dimensions labelled for the Ref-3 mesh. 17

Figure 2.6 Moving average of velocity magnitude at the point monitor in the Ref-3 mesh (location shown in Figure 2.5) using a 50-point moving window for data collected every 10 time steps. 18

Figure 2.7 Convergence of velocity and turbulent kinetic energy (TKE) statistics at the point monitor (location shown in Figure 2.5) with increasing mesh element count. 20

Figure 2.8 Cumulative mean and standard deviation of velocity magnitude at the point monitor (location shown in Figure 2.5) for the Ref-3 mesh. 20

Figure 2.9 Development of the QSS time-averaged velocity profile at the start of the wave pool (just before the steam interacts with the puree). 21

Figure 2.10 Time-averaged puree volume fraction profiles at the nozzle exit for all meshes. 22

Figure 2.11 Side view of puree-steam interface outline with velocity vectors and contour lines of velocity magnitude through one typical wave cycle for the Ref-3 mesh. 23

Figure 2.12 Sequential side contours of pressure with the puree-steam interface outlined through one typical wave cycle for the Ref-3 mesh. 25

Figure 2.13 Sequential side contours of pressure gradient through one typical wave cycle for the Ref-3 mesh. 26

Figure 2.14 Sequential side contours of surface free energy per unit area for Ref-3. 27

Figure 2.15 Windward side of the puree-steam interface colored by puree viscosity through one typical wave cycle for the Ref-3 mesh. 28

Figure 2.16 Leeward side of the puree-steam interface colored by puree viscosity through one typical wave cycle for the Ref-3 mesh. 29

Figure 2.17 Sequential side contours of steam Mach number through one typical wave cycle for the Ref-3 mesh. 30

Figure 2.18 Contour of time-averaged Mach number for Ref-3. 31

Figure 2.19 Sequential side contours of temperature through one typical wave cycle for the Ref-3 mesh. 31

Figure 2.20 Sequential side contours representing turbulent Weber number (Wt) through one typical wave cycle for the Ref-3 mesh. 33

Figure 2.21 Time-averaged integral length scale (L in meters) contour for Ref-3. 34

Figure 3.1 Illustration of the “original” banana puree production process. 39

Figure 3.2 Side view of the Ref-3 mesh (132 million elements) with important features labelled. 43

Figure 3.3 Sequential side views of banana puree (yellow) through one typical pulsing cycle. 44

Figure 3.4 Sequential views of puree atomization through one typical pulsing cycle, where the puree surface is colored by strain rate. 45

Figure 3.5 Sequential side contours of Mach number through one typical pulsing cycle. 47

Figure 3.6 Sequential side contours of temperature through one typical pulsing cycle. .. 48

Figure 3.7 Contours of time-averaged quantities: (a) puree volume fraction, (b) Mach number, and (c) integral length scale. 49

Figure 3.8 Momentum flow of a typical wave through three stages: 1) wave formation,[61] 2) wave collapse, and 3) radial burst. 51

Figure 3.9 Sequential views of puree atomization through one typical pulsing cycle, where the puree surface is colored by puree viscosity. 52

Figure 3.10 Sequential side contours of pressure through one typical pulsing cycle. 53

Figure 3.11 Sequential side contours of strain rate through one typical pulsing cycle. 54

Figure 3.12 Cumulative mean and standard deviation of SMD demonstrates sufficient sampling time to report time-averaged values. 55

Figure 3.13 Time-averaged axial SMD profiles for all models. 56

Figure 3.14 Actual Ref-3 mesh length scale compared to that required for four cells across each droplet. 56

Figure 3.15 A Hovmöller diagram of SMD showing the spatiotemporal variation in droplet size. 57

Figure 4.1 Oblique view of a representative Ref-3-AMR surface mesh, illustrating the nature of adaptive mesh refinement (AMR). 69

Figure 4.2 Side view of the 132 million element Ref-3 mesh for the pre-filming (wave formation) region of the atomizer. 70

Figure 4.3 Sequential views of unraveled wave with the slurry surface colored by viscosity and contours of strain rate in the background. 73

Figure 4.4 Sequential views of unraveled wave with the slurry surface colored by viscosity and contours of strain rate in the background. 74

Figure 4.5 Sequential views of unraveled wave with the slurry surface colored by pressure with contours of Mach number in the background. 75

Figure 4.6 Sequential views of unraveled wave (gray) with contours of temperature in the background. 76

Figure 4.7 Sequential side contours of baroclinic torque through one representative wave cycle. 77

Figure 4.8 Instability cycle, where the Kelvin-Helmholtz instability (KHI) and Rayleigh-Taylor instability (RTI) cause surface variations that in turn excite the instabilities (T = temperature, SR = strain rate, WL = wave length). 78

Figure 4.9 The ratio of radial velocity to the absolute value of axial velocity through one representative wave cycle. 82

Figure 4.10 The ratio of radial velocity to the absolute value of axial velocity at a fixed time, roughly where the wave peaks (equivalent to frame 4 in Figure 4.9). 83

Figure 4.11 Locations of five points monitors (roughly along the slurry interface trajectory) where certain data quantities are collected. 85

Figure 4.12 Moving average time series of (a) velocity and (b) slurry volume fraction at the Exit point monitors across all five azimuthal angles. 86

Figure 4.13 Moving average time series of (a) velocity and (b) strain rate at all five point monitors at the 22.5° angle. 88

Figure 4.14 Azimuthal coefficient of variation (COV) for frequency at various points along the slurry interface flow path. 90

Figure 4.15 Convergence of FFT peak frequency for the strain rate signal at the Exit point monitor in the 22.5° plane. 91

Figure 4.16 FFTs with peak frequency labeled for (a) velocity at the Inner point and (b) strain rate at the Exit point. 92

Figure 4.17 Normalized cross-correlation between transient velocity magnitude signals from point monitors at five points along the slurry interfacial flow and five azimuthal angles. 94

Figure 4.18 Transient velocity signal time lags from the Inner point at five azimuthal angles. 95

Figure 4.19 Contours across all 25 points for the normalized cross-correlations between 1) velocity magnitude and slurry volume fraction (left), 2) turbulent kinetic energy strain rate (middle), and 3) velocity magnitude and strain rate (right). 96

Figure 4.20 Comparison of slurry surface as computed by the Ref-3 (top row) and Ref-3-AMR (bottom row) meshes at three points in the wave cycle. 98

Figure 4.21 The percent difference between azimuthally-averaged quantities at various points along the slurry interface flow path for Ref-3 and Ref-3-AMR. 99

Figure 5.1 Side view of the WAVE atomizer geometry with an instantaneous sketch of the traveling wave. 103

Figure 5.2 PID controller feedback loop illustrated with a block diagram. 109

Figure 5.3 Despite independent control algorithms, the C1 and C2 controllers are coupled by physical interactions. 112

Figure 5.4 Test 1 controller response plots showing (a) slurry pressure (equivalent to pressure drop), (b) slurry mass flow rate, (c) Sauter mean diameter (SMD), and (d) steam mass flow rate. 118

Figure 5.5 Representative contours of slurry (red) and steam (black) with a slurry viscosity of 0.05 kg/m-s, demonstrating the change in droplet resolution as the mesh is refined. 120

Figure 5.6 Test 2 controller response plots showing (a) slurry pressure (equivalent to pressure drop), (b) slurry mass flow rate, (c) Sauter mean diameter (SMD), and (d) steam mass flow rate. 122

Figure 5.7 Side view of instantaneous pressure contours for half of the axisymmetric geometry (top). 123

Figure 5.8 Test 3 controller response plots showing (a) slurry pressure drop, (b) slurry mass flow rate, (c) Sauter mean diameter (SMD), and (d) steam mass flow rate. 125

Figure 5.9 Representative snapshots from Test 3 showing atomization before the viscosity shift and at the end of the test. 126

Figure 5.10 Representative instantaneous snapshots from Test 3 showing a side view of wave formation inside the nozzle. 128

Figure 5.11 Slurry interfacial pressure drop ($\Delta p2, s$) at the nozzle exit before the viscosity shift (left) and at the end of Test 3 (right). 129

Figure 5.12 Steam interfacial pressure drop ($\Delta p2, g$) at the nozzle exit before the viscosity shift (left) and at the end of Test 3 (right). 129

Figure 5.13 Representative snapshots of the unraveled wave with slurry surface colored by directional derivative of pressure normal to the surface and contours of steam density in the background. 130

CHAPTER ONE

INTRODUCTION

The focus of this research is the introduction and characterization of a new atomization framework called WAVE (Wave-Augmented Varicose Explosions) and the innovation of a “Smart” atomization technology therein. WAVE and Smart atomization labels were both coined as part of this research effort because they have never been studied before. WAVE involves a unique atomizer design and a viscous, non-Newtonian liquid. The twin-fluid atomizer/heater includes a central (rather than the conventional outer) gas flow and significant gas-liquid interaction before the nozzle exit. While the working fluid for this investigation is shear-thinning banana puree, similar benefits can likely be realized with any non-Newtonian slurry; steam is the assisting/heating gas. Periodic waves form inside the nozzle and produce radial bursting events, where the liquid bulges outward before exploding violently. Annular, high blockage ratio waves of this nature, which alone are unique and worthy of study, provide several atomization mechanisms for non-Newtonian slurries. Wave formation, its effect on atomization and heating, and the instabilities driving liquid breakup in WAVE are all focal points for this research.

Smart atomization technology is needed because certain liquids, such as banana puree, can have varying viscosity (compositional changes in time). Since viscosity drives droplet size, an increase in viscosity would hinder the atomization process as well as restrict liquid flow. This scenario presents a challenge: providing consistent atomization of a liquid with dynamically varying viscosity. The novel Smart atomization system presented here uses two independent proportional integral derivative (PID) controllers to mitigate effects of strong temporal viscosity fluctuations. A series of tests demonstrate the feasibility and benefit of such technology while providing guidance for future research efforts.

Again, both WAVE and Smart atomization have never been studied before. WAVE presents a unique physical process of high-blockage ratio annular waves repeating in a periodic wave cycle and providing important atomization mechanisms for non-Newtonian slurry heating and disintegration. Testing Smart atomization reveals the impact of viscosity transition and feed rate changes on atomization characteristics. The impact on atomization could be applicable for gelled propellant atomization in the aerospace industry or manure slurry atomization for waste-to-energy conversion; Smart atomization technology would especially be beneficial for atomizing a highly variable feedstock like manure.

The objective of this research was to reveal new mechanisms and physics of WAVE atomization and its response to Smart atomization. To fulfill this objective, four studies are presented in the following four chapters. The first three studies focus on aspects of WAVE; the fourth focuses on Smart atomization. Chapter II describes mechanisms driving wave formation inside the nozzle. Chapter III reveals the impact of waves on atomization characteristics. Chapter IV evaluates the spatiotemporal aspects of WAVE atomization. Finally, Chapter V presents Smart atomization testing with WAVE. Chapters II-V correspond to four peer-reviewed, published journal articles, each with their independent introduction, methods, results, and conclusions. More introductory details (including literature reviews) are provided in the individual chapter introductions. Many figures throughout this document have corresponding animations that are hosted on the "FLUID Group Research" YouTube channel here or discussed on the FLUID website here.

CHAPTER TWO

THE RISE AND FALL OF BANANA PUREE: NON-NEWTONIAN ANNULAR WAVE FORMATION BY TRANSONIC SELF-PULSATING FLOW

2.1 Introduction

Waves are one of the most widely recognizable fluid phenomena. Many peoples from time immemorial have had a popular level understanding of waves, but the details of wave formation are complex.[1] Lord Kelvin and Hermann von Helmholtz were two key 19th-century players in the modern study of waves, providing a mechanism for wave formation known as the Kelvin-Helmholtz instability (KHI). For a liquid and gas traveling at different velocities, KHI will cause a sufficiently perturbed interface to become unstable via induced pressure gradients. Many other figures in the 20th century built upon the work of Kelvin and Helmholtz, including Sir Harold Jeffreys, John Miles, and Owen Phillips. Jeffreys introduced the concept of wave sheltering, which gives rise to flow separation.[2] Miles and Phillips proposed wave formation mechanisms to account for the mean wind profile and wind turbulence, respectively.[3, 4]

More recently, in the 21st century, wave studies have continued with great vigor in the scientific community. Both internal and external wave motion on sloped surfaces has been studied experimentally, including the effect of undulated inclines on wave evolution.[5-7] Chang and Liu characterized an order of magnitude approximation for the turbulence intensity generated by breaking waves as proportional to the phase speed.[8] 2D simulations have revealed that breaking waves induce vortex-like motion below the surface, and 80% of the wave's energy dissipates within three wave periods.[9] Lin *et al*. described similarities in dimensionless aspects of waves travelling over a slope for waves in the same length scale regime.[10] They noted that at significantly smaller length scales, viscous friction and surface tension play a more prominent role, reducing similarity.

Wave formation takes on different characteristics when the liquid is non-Newtonian. Compared to its Newtonian counterpart, Millet *et al*. found a shear-thinning fluid on a slope to have a greater celerity and tend more readily toward instability.[11] Even at low Reynolds numbers, non-Newtonian fluid layers are prone to instability.[12] Both 2D and 3D effects are important, but Mogilevskiy demonstrates that 2D disturbances grow at a higher rate than 3D disturbances for a falling non-Newtonian film, irrespective of rheological model.[13] Tripathi *et al*. studied the interaction between a highly viscous non-Newtonian oil core and injected water in a pipe (core annular flow), though this does not represent multiphase wave formation.[14] Disturbance waves in an annular liquid film have been studied in vertical gas-liquid flow; such waves are on a small scale relative to the nozzle and propagate in series.[15, 16]

Annular waves in vertical conduits, where the wave height is large relative to the conduit radius (referred to as “high blockage ratio”), have the potential to differ significantly from planar waves. As a planar wave rises in the absence of any adjacent phase shear, the local acceleration and deformation is controlled by windward and leeward inertial effects and refractions caused by surface variations at the bottom of the liquid reservoir. When an annular wave “rises” (radially inward), on the other hand, the area for flow is reduced if the wave height is large relative to the conduit radius. Flow area reduction creates local acceleration approaching the crest (due to liquid phase viscosity) irrespective of any gas stimulation, which in turn will create a wave height increase. This feedback process continues until a new equilibrium is reached, the wave breaks, or some area change is encountered. Any gas phase support for wave production would further complicate the matter.

Given the scarcity of applicable studies, this paper adds to the current body of research a numerical study of viscous, non-Newtonian wave formation by annular injection of liquid into an enclosed, transonic gas flow. Our working non-Newtonian fluid, banana puree, is shear-thinning beyond a yield stress. An annular flow of puree is injected into a central steam pipe before exiting the atomizer nozzle. The proximity of the injection region to the nozzle exit makes for a uniquely brief wave shore, and wave formation is periodic with no wave train and a high blockage ratio. Prior studies do not address annular wave formation in an enclosed channel with a high blockage ratio in the presence of transonic flow, and our work is further distinguished by a highly viscous, non-Newtonian fluid.

The context of the overall wave generation system is a novel "core disrupting" twin-fluid atomization nozzle. Most twin-fluid atomizers inject gas around a central liquid flow, but inverting these feeds disintegrates viscous slurries more effectively and with lower gas flow rates.[17] Such a design could be instrumental for gelled propellants or energy reclamation by atomizing manure slurries with dynamically varying viscosity via smart atomization technology.[18] Another consequence of feed inversion for a non-Newtonian fluid is the formation of periodic waves (object of the present study) inside the nozzle leading to bulk atomizer pulsations and improved atomization downstream of the waves. We refer to the rupturing of puree in this novel atomization process as "wave-augmented varicose explosions" (WAVE). We use CFD to reveal mechanisms, instabilities, and characteristics of wave formation and collapse. Ref. 19 assesses the impact of wave formation on the downstream atomization.[19] While the computational domain is 3D, this paper focuses on the dominant 2D effects; Ref. 20 closely investigates the role of 3D instabilities.[20]

2.2 Methods

2.2.1 Computational Methods

The Navier-Stokes equations, which govern the present system, are presented in Equations 2.1-2.3, formulated for multiphase flow in vector notation. In Equations 2.1-2.3, α is phase volume fraction, ρ is density, t is time, u is the velocity vector, τ is the laminar shear stress tensor, τ_t is turbulent shear stress tensor, p is pressure, g is gravity, F is the surface tension force vector, C_p is constant pressure heat capacity, T is the static temperature, ζ is laminar conductivity, μ_t is the turbulent viscosity, and Pr_t is the turbulent Prantdl number. Properties are arithmetically phase-averaged, and the steam density ρ is set by the ideal gas equation of state. The banana puree was modeled as an incompressible fluid. The effects of compressibility on turbulence and all other sub-grid-scale modeled quantities were ignored, as well as kinetic energy and viscous heating effects. Some authors propose that supersonic/hypersonic boundary layers exhibit close similarities to incompressible boundary layers.[21] Others have found differences between near-wall turbulent fluxes in compressible flow and incompressible scaling laws, but these differences only potentially affect the relatively short low-Mach number region upstream of wave development and can be ignored here.[22]

$$\frac{\partial}{\partial t}(\alpha\rho) + \nabla \cdot (\alpha\rho\bar{u}) = 0 \tag{2.1}$$

$$\frac{\partial}{\partial t}(\rho\bar{u}) + \rho\bar{u} \cdot \nabla\bar{u} = \nabla \cdot (\tau + \tau_t) - \nabla \mathrm{p} + \left(\mathrm{\rho} - \rho_{ref}\right)\bar{g} + \bar{F} \tag{2.2}$$

$$\frac{\partial}{\partial t}(\rho C_P T) + \nabla \cdot [\bar{u}(\rho C_P T)] = \nabla \cdot \left[\left(\zeta + \frac{\mu_t}{Pr_t}\right)\nabla T\right] \tag{2.3}$$

The Reynolds-Averaged Navier-Stokes and volume-of-fluid (VOF) equations were solved with a commercially available CFD solver ANSYS Fluent 2020 R1. The CFD model uses the shear stress transport (SST) formulation of the k-ω turbulence model and the SIMPLE (Semi-IMplicit Pressure Linked Equations) pressure-velocity coupling scheme. SIMPLE is a segregated approach that updates pressure and velocity in sequential steps rather than simultaneously.[23] The discretization schemes are as follows: PRESTO! (PREssure STaggering Option) for pressure; second order upwind for momentum, energy, and density; and first order upwind for turbulence quantities. PRESTO! is a pressure staggering scheme that obtains face pressures by means of continuity balances rather than central differencing.[24] The VOF interface was closely resolved explicitly using the geometric reconstruction technique by Youngs,[25] otherwise known as “piecewise linear interface capturing” (PLIC).[9, 26] The PLIC approach approximates the interface as a plane in each computational cell for 3D solvers. A variable time step size adjusted every 3 time steps to maintain a convective Courant number of about 1, with a maximum of 7 iterations per time step. The average time step size naturally varied with mesh size but stayed on the order of 1×10^{-8} s for the finest meshes. The consequence is approximately 1×10^{5} timesteps within the life of a wave. The same numerics are employed by all models; mesh alone is the distinguishing variable in mesh resolution studies.

Models were deemed at quasi steady state (QSS) when a multitude of point-monitored quantities reached statistically stationary values. Time-averaged statistics were only collected after QSS was reached. Methods for determining convergence of time-averaged quantities will be discussed later. In all presentations of data, flow time is normalized by the wave time scale, which is defined as the time for a wave to proceed through one cycle of formation and collapse (more on this later). Hereafter, flow time will be referred to in units of "wave times" (WTs) rather than flow seconds. The computational techniques employed herein have been extensively validated and analyzed for sensitivity in past transonic wave formation studies.[24, 26-34] In particular, the SST k-ω turbulence model and 90° azimuthal wedge mesh (employed in this present study) were shown to be advantageous for accurately capturing the important physical mechanisms. For example, changing the azimuthal angle from 11.25° to 360° only altered the Sauter mean diameter by 10%.[32] Again, each time step amounts to one-hundred-thousandth of a wave cycle.

Based on the aforementioned citations, the following validation exercises have been carried out on our computational methodology. 1) The experimentally determined globally pulsing nature of an industrial three-stream air-water atomizer was qualitatively demonstrated computationally. 2) The acoustic signature of that injector's pulsations was quantitatively matched computationally. 3) The primary atomization ligament wave positions were quantitatively paralleled numerically. 4) The analytical trajectory of a droplet disintegrating after being exposed to a normal shock wave was quantitively reproduced numerically. 5) The axially decaying droplet size distribution from a non-Newtonian atomizer was quantitatively replicated numerically. 6) A study of azimuthal angle revealed that reduced order models encompassing only 1/32nd of a full 360° azimuth do not significantly degrade the assessment of axial droplet size distribution. Finally, our present study qualitatively demonstrates the expected globally varicose pulsing nature of a recessed, inverted feed atomizer at high gas-liquid momentum ratio.[35]

2.2.2 Mesh and Boundary Conditions

Figure 2.1 provides an overview of the geometry of the system: banana puree is injected into a central steam pipe from an outer annulus, after which the two phases interact and exit the nozzle. Flow is generally from left to right. Hereafter, the region where the puree meets the steam pipe will be referred to as the "wave pool" and the nozzle extension just past this as the "beach" (equivalent to "shore"). We model a 90° azimuthal slice of the full 360° azimuth for computational efficiency (barring one exception with a 45° azimuth). Increasing the azimuthal angle from 45° to 90° was shown to have negligible effect on droplet sizes, which are dictated by wave physics.[19] The domain extends two nozzle diameters past the nozzle exit in the axial direction, but that is beyond the scope of the present study. Both phase conduits extend upstream beyond what is shown. The important geometric and flow parameters describing the nozzle are provided in Table 2.1. This geometry was derived from initial work by Strasser,[36] which showed it to be advantageous for non-Newtonian slurry disintegration, but it has not been optimized. The effect of geometry changes on spray characteristics remains an open question.

The 90° wedge model is bookended by periodic boundary conditions. All walls are adiabatic. The steam and puree inlets were set to constant mass flow rates for a resultant gas-liquid mass ratio (GLR) of 2.7%. Similar GLRs have been used for reduced-GLR airblast atomization of gelled propellants.[37] Effective atomization at lower GLRs is desirable for improved efficiency. Though not addressed in this work, the dependence of spray characteristics on GLR would be useful for optimization. Inlet temperatures are 393 K and 304 K for the steam and puree, respectively, and steam is assumed to remain a vapor (no condensation). Steam inlet turbulence intensity and turbulent viscosity ratio were set to 5% and 10, respectively, which translates to spatially constant values of k = 48 m^2/s^2 and ω = 2.5×10^5 1/s. It is expected that k and ω in the upstream steam pipe will influence steam boundary layer development, which might affect KHI growth rate in the wave pool. Our results should, therefore, be interpreted in light of *this particular* choice of feed turbulence conditions. Other geometries with other flow rates and/or other feed conditions (turbulence quantities or otherwise) can be studied in a future effort.

The non-Newtonian nature of banana puree can be described by the Herschel–Bulkley model; beyond a yield stress, the puree is shear-thinning. Depending on production methods, banana puree might take on a range of properties. For the present study, banana puree is treated according to experimental data of Ditchfield *et al.*, which spans the range of inlet temperatures.[38] The Herschel-Bulkley model was incorporated as a user-defined function (UDF) in Fluent to make the puree viscosity a function of both strain rate and temperature. The UDF follows Equations 2.4-2.7 to compute viscosity, where μ is puree viscosity, $\dot{\gamma}$ is strain rate magnitude, and τ_0 is the yield stress. k and n are both calculated from temperature T for incorporation in Equation 2.4. $\dot{\gamma}_0 = 10s^{-1}$ is the minimum strain rate that we have data for and is used as a lower bound to prevent the viscosity from diverging at low strain rates. μ_0 represents a bounding value of viscosity calculated using

$\dot{\gamma}_0$. Puree density is assumed to be constant at 1028 kg/m^3 (323 K at °Brix of 22.1), although density can vary minimally as a function of temperature for a given solids concentration.[39]

$$\mu = \begin{cases} \mu_0, \ \dot{\gamma} \le \dot{\gamma}_0 \\ \frac{\tau_0}{\dot{\gamma}} + k\dot{\gamma}^{n-1}, \ \dot{\gamma} > \dot{\gamma}_0 \end{cases} \tag{2.4}$$

$$\tau_0 = 99.8 - 0.53T \tag{2.5}$$

$$k = 1.2 \times 10^5 T^{-2.5} \tag{2.6}$$

$$n = 0.069T^{0.41} \tag{2.7}$$

A Base mesh with a 90° azimuth was refined three times to create a serious of four increasingly fine meshes, as presented in Table 2.2 and Figure 2.2 (flow from left to right). Refinement cuts each cell length in half in all three dimensions (within a prescribed region), effectively splitting a given cell into eight smaller cells. The refinement region is a majority subset of the entire domain that includes all areas except farther back into the steam pipe and puree annulus. Importantly, the refinement region includes all steam/puree interaction. All meshes are composed almost entirely of hexahedral elements, with a very small fraction of triangular prims. To produce a "Ref-*n*" mesh, the Base mesh was refined *n* times. Two additional meshes deviate from this simple pattern: Ref-2-45 entails a 45° azimuth, and Ref-3-AMR uses adaptive mesh refinement (AMR).

AMR dynamically refines the mesh only in localized areas around the gas-liquid interface and has been used before in direct numerical simulations of waves.[40] The obvious benefit of AMR is computational efficiency: the Ref-3-AMR mesh has a Ref-3 refinement level but only as needed to adequately resolve the interface. While the exact number of elements fluctuates between ~26 and ~30 million during a simulation, Ref-3-AMR consistently utilizes less than a quarter of the Ref-3 cell count. Figure 2.3 provides a snapshot to illustrate the nature of AMR. To adequately follow the constantly moving interface, including all droplets, the AMR region was updated every 5 time steps based on a stringent volume fraction gradient criterion.

Hardware and run rates for all models are presented in Table 2.2. The hardware configuration (including node counts and cores/node utilized) was optimized, producing the highest possible run rate, for all models except the Base case, according to a novel in-house methodology.[41] The influence of mesh, convergence, and sampling time for time-averaged statistics will be further discussed throughout this paper.

Table 2.1 Parameters describing the geometric and flow conditions of the atomizer nozzle.

Parameter	Value	Units
Nozzle Diameter	16	mm
Wave Pool Width	6.8	mm
Beach Width	3	mm
Puree Annular Gap	9.8	mm
Inner Angle	29	degrees
Outer Angle	60	degrees
Steam Mass Flow	0.021	kg/s
Puree Mass Flow	0.79	kg/s

Table 2.2 Mesh size, hardware, and run time (numerics are consistent across models).

Model Name	Cell Count [10^6]	Core Type	Node Count	Core Loading	Run Rate [WT/day]	QSS WT	TA WT
Base	0.3	AMD EPYC 7742	1	117/120	27	11	14
Ref-1	2.1	AMD EPYC 7763	1	120/120	5.2	99	37
Ref-2-45	8.3	AMD EPYC 7742	1	117/120	0.52	4.4	
Ref-2	17	AMD EPYC 7742	4	118/120	0.91	24	7.5
Ref-3-AMR	~28	AMD EPYC 7763	12	64/120	0.29	8.6	5.4
Ref-3	132	AMD EPYC 7763	16	120/120	0.18	12	8.5

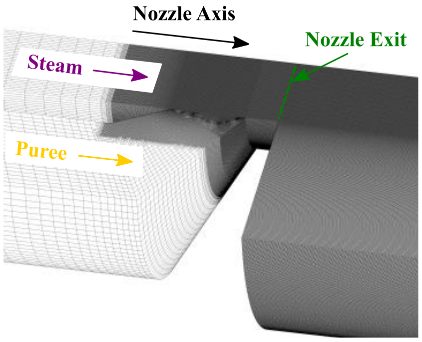

Figure 2.1 Isometric view of Ref-3 surface mesh for the pre-filming (wave formation) region of our twin-fluid atomizer.

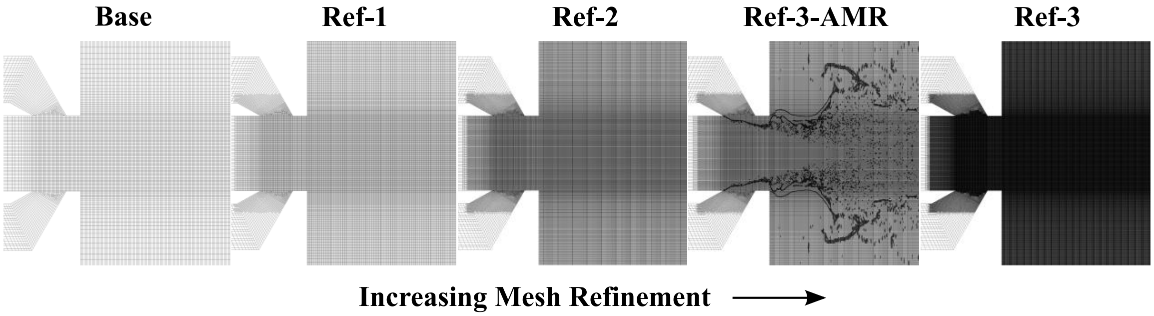

Figure 2.2 Side view of meshes with increasing levels of refinement.

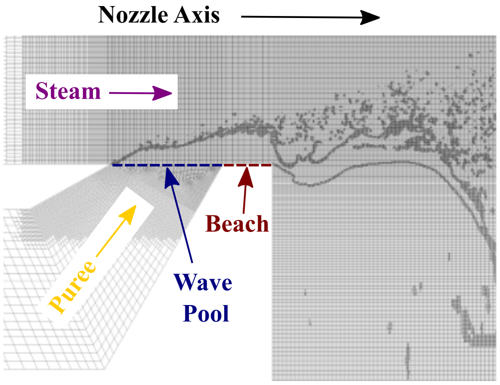

Figure 2.3 Side view of the Ref-3-AMR mesh, illustrating the nature of adaptive mesh refinement.

2.3 Results and Discussion

2.3.1 Wave Cycle Overview

As banana puree is injected into the central steam pipe, waves develop in a cyclical pattern. An overview of a single wave cycle is provided in Figure 2.4. No train of waves exists. Rather, a new wave rises only in the wake of a dying wave. When both a newly forming wave and a dying wave can be seen together, the former may be referred to as the "daughter" wave and the latter as the "parent" wave to provide distinction. The life of a wave in a "wave cycle" is divided into two stages: formation and collapse. In Figure 2.4, frames 1-5 show the formation of a wave as it rises out of the relatively stagnant puree wave pool. Note that the wave thickness is fairly large relative to the steam pipe radius; therefore, as the wave rises, the puree flow area is reduced. The viscosity of the puree causes a velocity gradient (vorticity) to develop inside the wave, and the crest is accelerated more. The shear-thinning nature of the puree reduces the viscosity approaching the crest, allowing it to accelerate even more.

As the wave base approaches the beach, its base is decelerated by the no-slip boundary at the nozzle wall. This produces vorticity as the wave wants to curl over. A shear stress imbalance exists where the gas is attempting to accelerate on top of the wave while the beach is attempting to decelerate the wave. Frames 6-8 show the wave collapse, starting roughly where the wave crest reaches the nozzle exit and attains its maximum height. Synchronous with the collapse of the parent wave is the bulging of puree radially outward just past the nozzle exit (starts in frame 6, but clearer in frames 7 and 8). It is evident that the collapse of a given wave corresponds precisely to the formation of a new wave, thereby beginning another wave cycle. The enclosed channel environment with high-speed, transonic steam truncates the natural growth and breaking of the wave and accelerates disintegration (see free-surface waves simulated by Mostert *et al.*, for example, where disintegration and droplet formation largely happen after breaking with splash-up).[40] More on atomization is discussed in Ref. 19. It is for this reason that we describe the wave as collapsing" rather than the conventional "breaking" towards the end of its life.

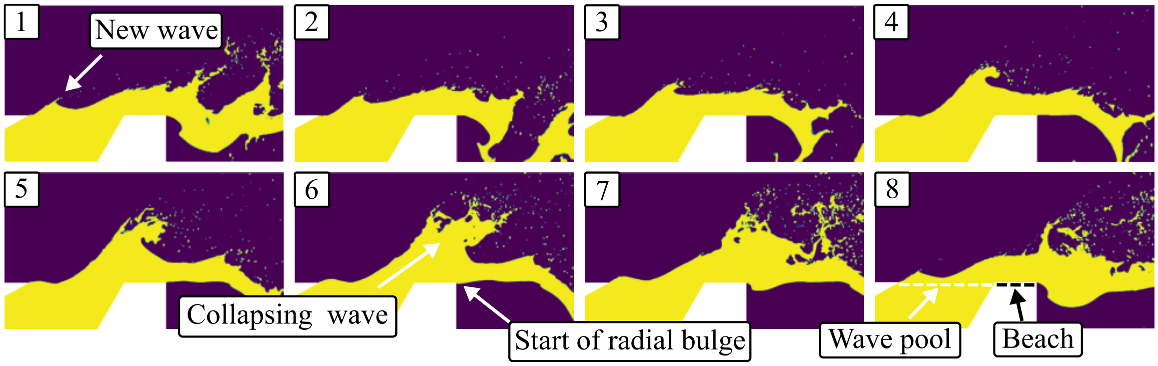

Figure 2.4 Sequential side views of banana puree (yellow) through one predominantly 2D wave cycle for the Ref-3 mesh.

Figure 2.5 labels major dimensions for the geometry and a given wave. Here, r is the steam pipe (and nozzle) radius, d is the depth of puree injected, p is the width of the wave pool, and b is the width of the beach (distance from injection zone to nozzle exit). We expect azimuthal curvature in the nozzle geometry to influence wave formation, but that is beyond the scope of this study. Because the puree injection annular walls are angled, we consider d to be the distance from the outer edge of the steam pipe to the radial center of the puree annulus (d extends below the bottom of Figure 2.5). A puree wave is described by its height (h), puree thickness at the nozzle exit (e), the wave angle (θ), the wavelength (λ), and the wave speed (c). In the absence of wave trains, the wavelength is considered the axial distance between a newly forming wave peak and the outermost point of the radial bulge resulting from the collapse of the previous wave. The average wavelength was measured for three sampled independent wave cycles to be 0.7 nozzle diameters with only a 0.57% coefficient of variation (COV), demonstrating remarkable consistency. Wave angles before collapse were around 50°. The measured wave speed is greater than the natural wave speed $\sqrt{gd}$ by a factor of 37. We suggest several dimensionless ratios to describe the system: $\epsilon = \frac{\lambda}{p} = 1.6$, $\phi = \frac{h}{p} = 0.59$, $\psi = \frac{\lambda}{b} = 3.6$, $\beta = \frac{h}{r} = 0.5$, and $\eta = \frac{e}{p} = 0.17$. Here, h is the peak wave height, and e is the approximate time-averaged value for all meshes except the Base case. ψ highlights the abbreviated beach, which is 0.28 times smaller than the wavelength. β represents the wave blockage ratio, the percentage of the steam pipe that is blocked by the wave. These ratios are likely themselves functions of governing dimensionless numbers, such as Reynolds, Mach, Ohnesorge, and Weber numbers, and could be especially useful when considering geometry changes and their impact on wave formation. The ratio $\alpha = \frac{b}{p} = 4.4$ is expected to be an important geometric ratio, and its impact on wave formation is of great interest. However, effects of geometry are relegated to a future study.

These particularly well-known dimensionless numbers will be used to characterize waves in this system: Weber number ($We = \rho_l c^2 \lambda / \sigma$), Reynolds number ($Re = \rho_l c \lambda / \mu_l$), and Strouhal number ($St = f\lambda / V$). Our characteristic length scale is λ. Rather than using the deep-water wave velocity for We and Re,[42] wave speed c is more appropriate for our system. ρ_l is the density of puree, σ is surface tension, μ_l is the lowest puree viscosity observed in the wave, f is frequency, and V is bulk velocity of the steam and puree. The wave Weber number, which captures the ratio of inertial to surface tension effects, is 2.0×10^4. The Reynolds number, which captures the ratio of inertial to viscous effects, is 1.2×10^4. The Strouhal number here is effectively the ratio of wave velocity to bulk velocity in the channel and is 0.08. The wave We and Re are respectively higher and lower by an order of magnitude than those reported by Chan *et al.* for free-surface water waves.[42] The waves in this system have a high inertia, which overcomes surface tension to disintegrate more rapidly than is usually the case for free-surface waves. A lower Re stems largely from the high viscosity of the banana puree.

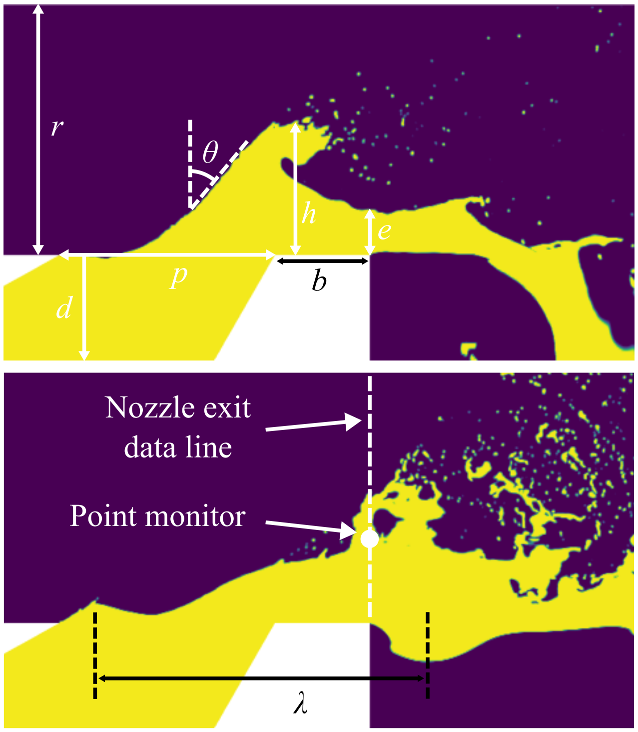

Figure 2.5 Side view of predominantly 2D banana puree wave a) as it crests and b) after it collapses (where a new wave forms) with major dimensions labelled for the Ref-3 mesh.

Select quantities were collected at a point monitor in line with the nozzle exit, 1/3 of the way in from the outer steam pipe radius, and at a 22.5° azimuthal angle within the 90° wedge (see Figure 2.5). Each wave moves through this point, and the nozzle exit is of particular interest as the point of transition from wave growth to collapse. This point will hereafter be referred to simply as the "point monitor."

A study of multiple wave cycles reveals two characteristics: 1) wave formation and collapse occur at very regular intervals, and 2) instabilities result in distinctly unique waves each cycle. To illustrate these dynamics, the moving average of the velocity magnitude at the point monitor is presented in Figure 2.6. Nine wave cycles are evident, repeating approximately every WT = 0.001 s. We therefore expect the dominant frequency of the system to be 1/WT = 1000 Hz.

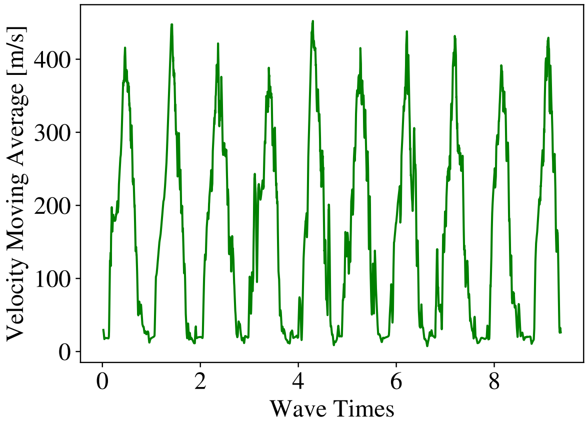

Figure 2.6 Moving average of velocity magnitude at the point monitor in the Ref-3 mesh (location shown in Figure 2.5) using a 50-point moving window for data collected every 10 time steps.

2.3.2 Mesh Independence

The Ref-3 mesh is sufficient for the purposes of this study based on the convergence shown in Figure 2.7, where the abscissa is the cell count relative to the Ref-1 mesh. Both mean and standard deviation of velocity and turbulent kinetic energy (TKE), as measured at the point monitor at QSS, are reasonably close to convergence by Ref-3 (highest element count on the right). We conclude that the Ref-3 mesh is sufficient for identifying major wave mechanisms and characteristics. Ref-3-AMR falls as an outlier to all power law trends; consequently, *the lines connecting the points do not include AMR results*. Further investigation is needed to fully assess the effects and implications of the AMR technique for wave formation, and Figure 2.7 suggests caution. We observe 83% and 128% transient variability in velocity and TKE, respectively. Fast Fourier Transforms (FFTs) reveal similar peak frequencies across all meshes, including Ref-3-AMR, except for Base. Besides the Base mesh, all peak frequencies are within 7% of 1000 Hz, which corresponds to the inverse of WT = 0.001 s. FFT analysis highlights an important point: the general physics of wave formation are similar in meshes Ref-1 through Ref-3, but the Base mesh physics are distinctly different. In particular, very little wave formation and periodicity is evident in the prohibitively coarse Base mesh.

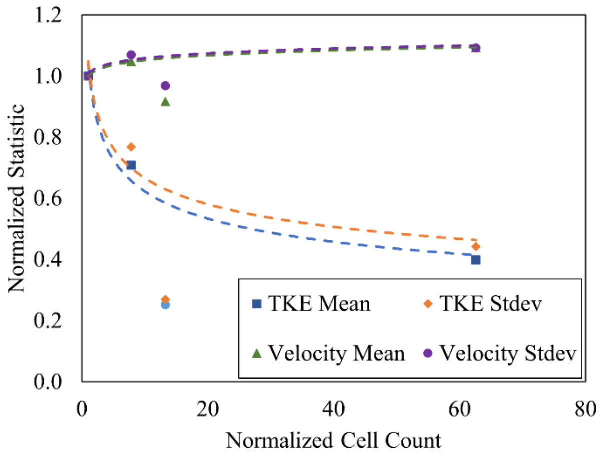

Figure 2.7 Convergence of velocity and turbulent kinetic energy (TKE) statistics at the point monitor (location shown in Figure 2.5) with increasing mesh element count.

The cumulative mean and standard deviation of velocity in Figure 2.8 (for Ref-3) have largely settled within the QSS sampling period used to calculate statistics in Figure 2.7. Though not shown, peak frequencies from FFTs also converged within the sampling period. The error associated with insufficient sampling time for a transient model scales with $1/\sqrt{T}$, where T is a convective time scale.[43] We thus conclude that our QSS sampling time is sufficient for time-averaged quantities and statistics.

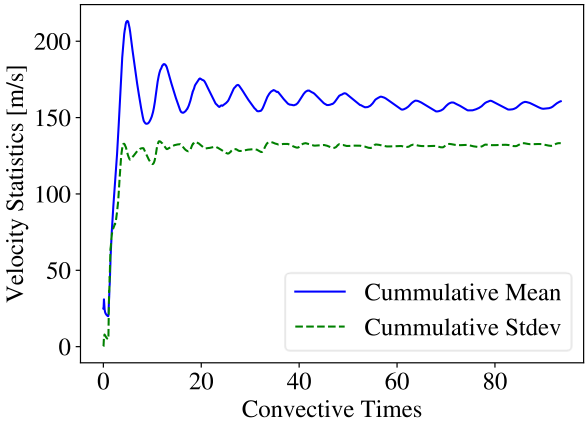

Figure 2.8 Cumulative mean and standard deviation of velocity magnitude at the point monitor (location shown in Figure 2.5) for the Ref-3 mesh.

We consider 3 WTs sufficient to produce time-averaged profiles. The series of velocity profiles in Figure 2.9 illustrate the mixture boundary layer profile at the start of the wave pool. They become reasonably invariant within 3 WTs. The time-averaged WTs for all models are well above this range (see Table 2.2).

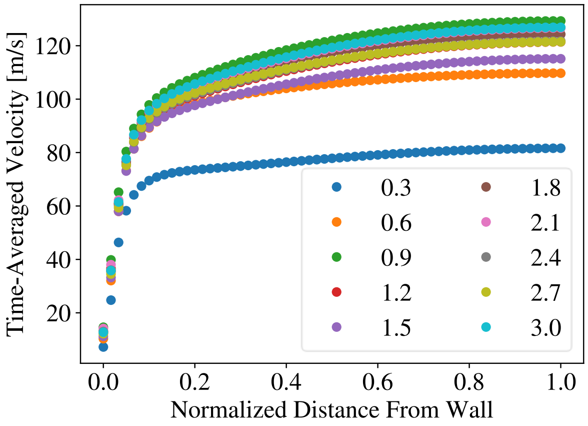

Figure 2.9 Development of the QSS time-averaged velocity profile at the start of the wave pool (just before the steam interacts with the puree).

An important measure is the TA radial puree thickness on the beach at the nozzle exit, which results from the collective effect of the aforementioned forces over time, and the response of the puree's viscosity, at the beach. The TA puree volume fraction profiles at the nozzle exit in Figure 2.10 are largely similar except for the Base mesh. These profiles essentially communicate the puree depth *e* in Figure 2.5, and the time-averaged exit velocity of the puree sheet is about 10 m/s. Wave crests produce the bulges on the left; more pronounced bulges correspond to more pronounced waves. Again, we observed that the Base case's physics are not consistent with other models. The other models are reasonably uniform, and the primary differentiating factor is the wave crest on the left. Interestingly, Ref-2 has a more pronounced crest than Ref-3 and Ref-3-AMR. Visual inspection reveals a slightly earlier start to wave disintegration for the finer meshes. Still, from Figure 2.10 and other metrics (pulsation frequency and wavelength, for example), we note that the essential wave physics of Ref-3 were captured by Ref-1 at the first refinement level. Ref-3, then, is sufficiently close to Ref-2 and Ref-1 for the purposes of this study.

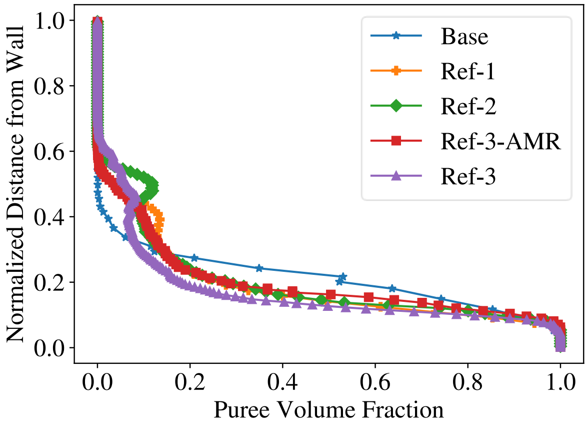

Figure 2.10 Time-averaged puree volume fraction profiles at the nozzle exit for all meshes.

2.3.3 Wave Mechanisms

Each wave starts forming by the KHI, which is induced by velocity gradients. Gravitational effects are irrelevant for this study, as the Froude number ($Fr = V/\sqrt{g\lambda}$) is 425. The two competing forces, then, are surface tension (stabilizing) and the Bernoulli effect (destabilizing). It follows that there exists some steam velocity below which waves will not form. Unlike free-surface waves, the mass flow of puree into the steam pipe provides an additional mechanism for deforming the interface. The decrease in pressure associated with the increase in velocity as the streamlines curve around the protruding puree (i.e., the Bernoulli effect), lifts the puree from the wave pool into the steam flow. After initial rising, the wave continues to climb radially inward due to KHI, shear lifting, puree injection, and acceleration from reduced flow area.

The mechanism of streamline deflection by the interfacial geometry, which produces flow separation and sheltering, was first introduced and defended by Sir Harold Jeffreys.[2] Figure 2.11illustrates this phenomenon in our system. The reader will notice a low-velocity region on the windward side of a newly forming wave (first noticeable in frame 2), what we refer to as the "well" behind the parent wave. As the wave travels to the right, it leaves a surface dip in its wake where steam decelerates (frames 2-4). Lower velocity will induce higher pressure in the well, which could explain why the next wave begins to rise behind the well (frame 5). While the geometry of the daughter wave is a rounded hump (frames 6-7), the flow continues to decelerate on its leeward side. We hypothesize the following: flow separation from the new wave first occurs in frame 8, where steam shear alters the geometry from a rounded hump to a more pointed peak. At this point, the low-velocity well disappears. The effect of shear in transitioning the geometry is marked by droplets being stripped off the wave (first seen in frame 8 for the new wave). Towards the later stages of wave life, the wave disrupts steam flow in more complex ways as it begins to disintegrate.

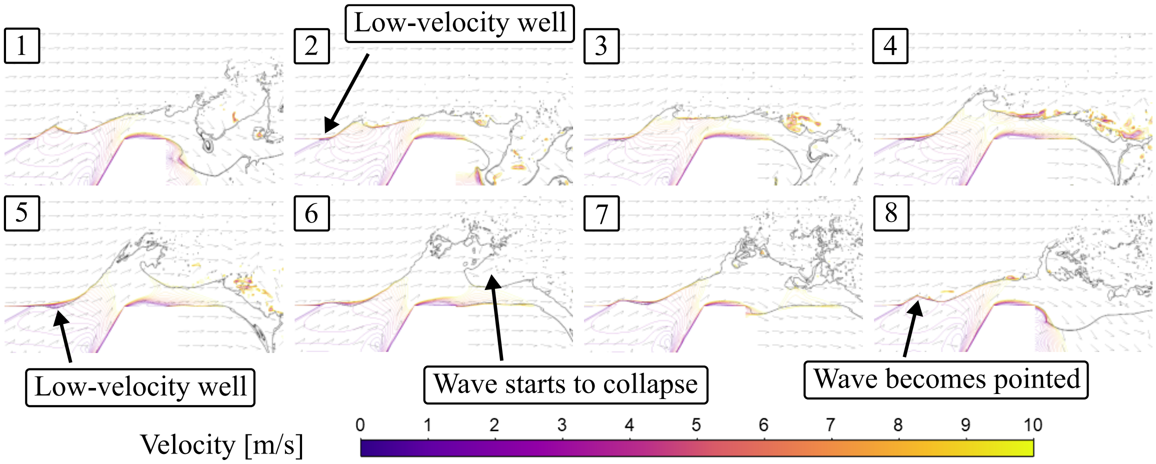

Figure 2.11 Side view of puree-steam interface outline with velocity vectors and contour lines of velocity magnitude through one typical wave cycle for the Ref-3 mesh.

As the wave approaches the nozzle exit (frame 5), some disintegration is observed on the windward side of the wave crest. In frame 6 of Figure 2.12, the wave crests and transitions from formation to collapse around the nozzle exit. At the same time, puree starts to bulge radially just outside the nozzle exit. In frames 2-5, no pressure gradient exists to alter the direction of puree flow. Consequently, puree stretches from the nozzle in an annular sheet. This sheet will be non-uniform from Rayleigh-Tayler instabilities (RTI) induced by density gradients, but that is beyond the scope of this document (see Ref. 20 for more details). The windward pressure acts normal to the surface of the wave and propagates through the wave (see frames 5-7), highlighting the significance of wave angle. By the time the wave reaches the nozzle exit, the pressure has sufficient magnitude and acting area to move the puree radially outward (well before the wave collapses into the annular puree sheet).

The difference between windward and leeward pressure (reduced by sheltering) drives the wave to collapse by overcoming puree inertia. We note again that free-surface waves experience no such windward pressure build-up, which is a direct result of steam compression in the enclosed space. Pressure also overcomes surface tension to partially disintegrate the wave. After collapse, the pressure distributes, leaving a stark pressure difference across the bulging puree sheet (frame 8). RTI, wave collapse induced imperfections, and viscosity gradients create weak points where the pressure is most likely to rupture the puree sheet.[19] The cycling of pressure produces axial steam pressure fluctuations that most probably superimpose on other effects to influence wave physics, in particular adding to the Bernoulli effect pulling on the wave pool surface. In summary, a given wave starts to grow by KHI (formation stage) but is later dominated by pressure effects (collapse stage). The vectors in Figure 2.11 show the rise and fall of a wave to follow a roughly parabolic trajectory.

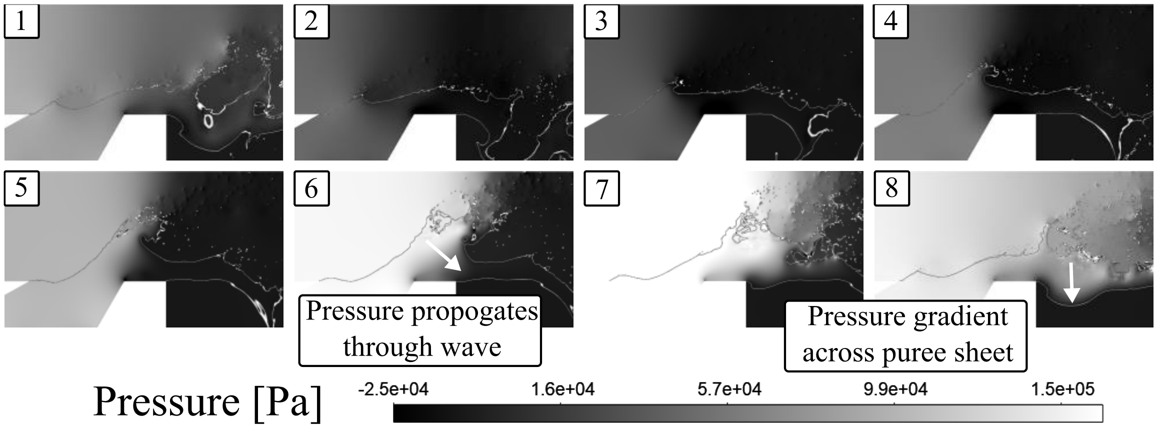

Figure 2.12 Sequential side contours of pressure with the puree-steam interface outlined through one typical wave cycle for the Ref-3 mesh.

Pressure gradient in Figure 2.13 reveals areas of high steam compression. Droplets stripped off the wave obstruct the steam flow, locally compressing the steam. Pressure gradients behind the wave start relaxing as the wave collapses (frames 8 and 1) and build back up as the next wave rises (frames 2-7). A region of high pressure gradient appears in the puree on the leeward side of a newly forming wave (frames 1-4). By frame 5, this region appears only on the leeward side of the next wave.

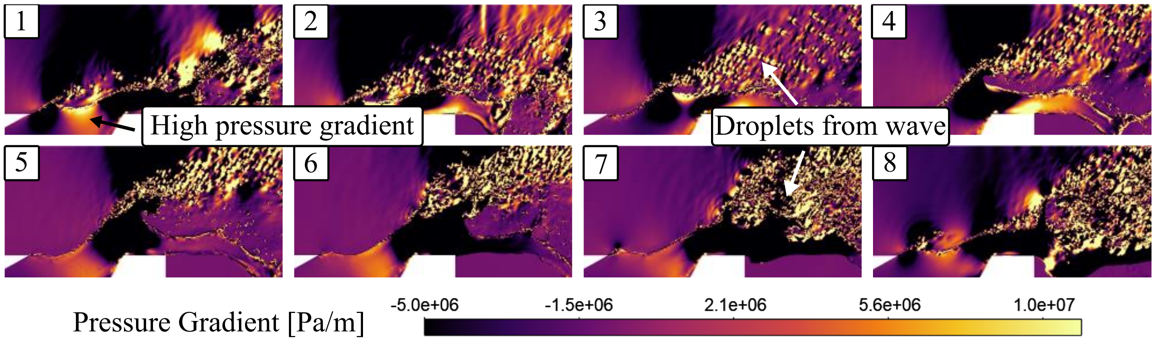

Figure 2.13 Sequential side contours of pressure gradient through one typical wave cycle for the Ref-3 mesh.

The change in puree surface free energy per unit area is estimated as the product of surface tension and strain rate at the interface.[44] Figure 2.14 illustrates the evolution of surface energy during wave formation and collapse. As the wave crests (frame 5), there is a distinct lack of surface energy at the beginning of the wave pool, where the next wave will form. A gradual increase in surface energy marks the rise of a new wave (frames 6 and 7), increasing until droplets start stripping away (frame 8). The distribution of surface energy up to the nozzle exit is relatively uniform in frame 8, before sheltering occurs.

Sheltered regions, particularly when the wave rises to shelter its leeward side (frames 1-6), contain less surface energy. The breaking away of droplets and general disintegration of the wave occurs, as expected, in regions of high surface energy. The exception to this is the windward side of the wave, where the steep slope of the wave and the curvature of the streamlines leave droplets nowhere to go, despite relatively high surface energy. It is only after the slope of the windward side decreases in the wake of wave collapse (frames 7-8) that droplets break away from this surface.

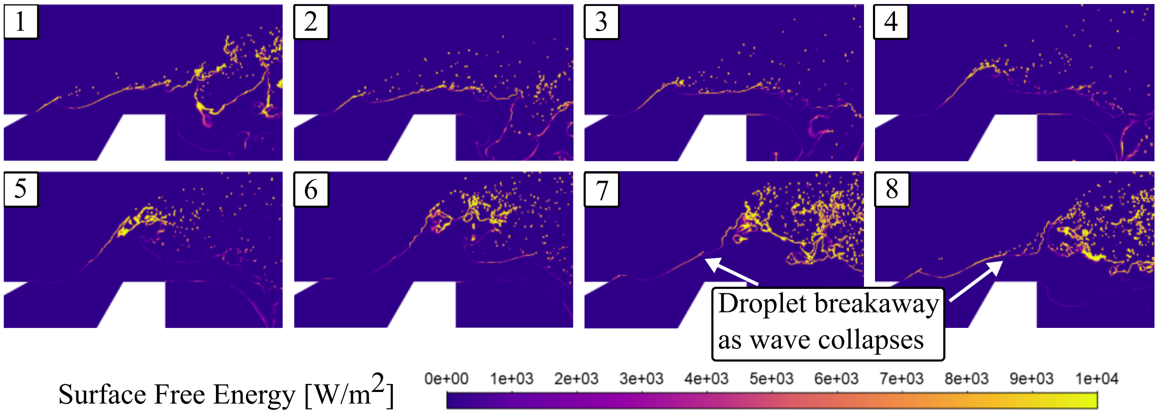

Figure 2.14 Sequential side contours of surface free energy per unit area for Ref-3.

We expect the non-Newtonian nature of banana puree to affect wave formation and increase fluid instability.[11] Figure 2.15 shows the puree-steam interface colored by viscosity looking towards the windward side of the wave (only a 90° azimuth is shown). Significant Rayleigh-Taylor variability is evident across the azimuth, which indicates that 90° is sufficient to capture azimuthal effects.[20] A high-viscosity region appears behind the rising wave (frames 3-7), which corresponds to the low-velocity well in Figure 2.11 and is a low strain-rate zone. As the gentle hump of a new wave (frames 5-6) transitions to a more pointed wave with a steeper slope (frames 7-8), the high-viscosity region largely disappears, corresponding to the disappearance of the well in Figure 2.11. Viscosity variation could contribute to the rising of a new wave and the location at which this occurs. The clear reduction in puree viscosity caused by upward penetration into the steam flow enables increased wave speed and enhanced disintegration. The reader will notice that the wave is axisymmetric (2D) through much of its life. There are obvious azimuthal instabilities and breakup which drive droplet production, but those are beyond the scope of this paper; they are discussed in Ref. 19 and Ref. 20. We continue to focus on the life of the contiguous wave itself.

Figure 2.16 shows the puree-steam interface colored by viscosity looking towards the leeward side of the wave. As the wave crests, the annular puree sheet stretching past the nozzle exit downstream develops significant viscosity gradients (frames 4-6, particularly frame 5). Viscosity gradients, in addition to RTI, increase the instability of the annular sheet, "priming" it for disintegration upon wave collapse.[19] It is difficult to say to what degree shear-dependent viscosity affects wave formation, growth, and collapse without a comparison to a Newtonian fluid in the same system. Such a comparison is relegated to a future study.

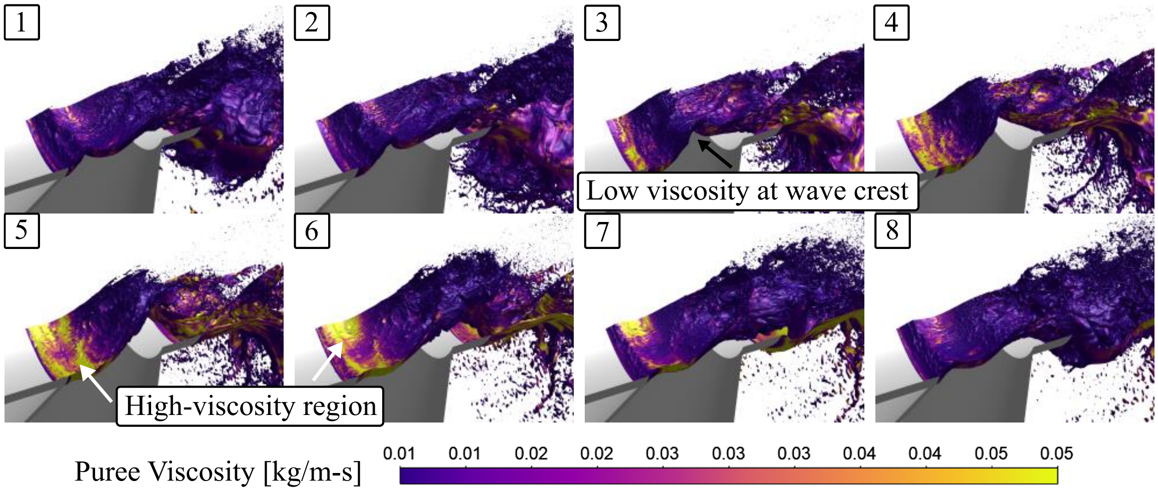

Figure 2.15 Windward side of the puree-steam interface colored by puree viscosity through one typical wave cycle for the Ref-3 mesh.

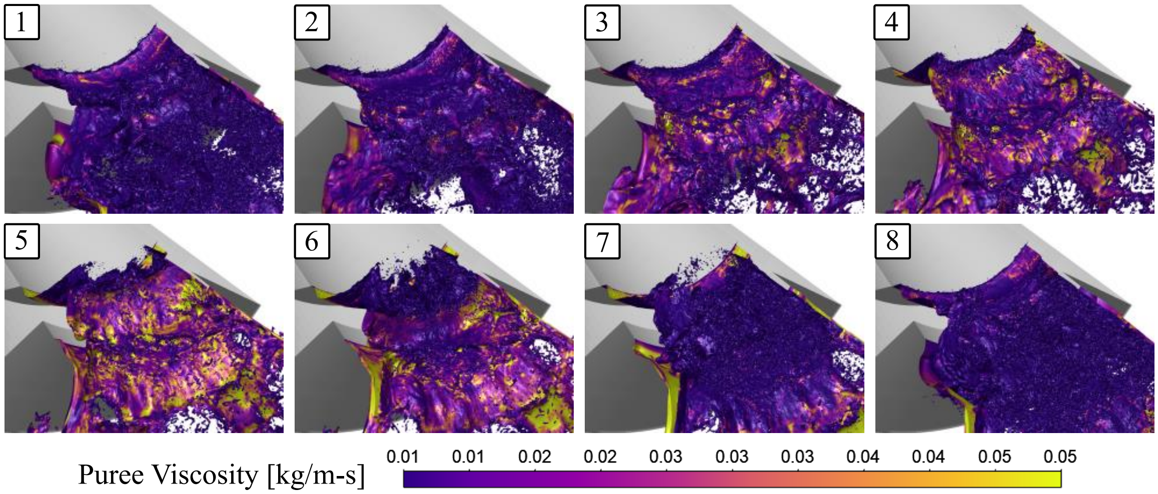

Figure 2.16 Leeward side of the puree-steam interface colored by puree viscosity through one typical wave cycle for the Ref-3 mesh.

2.3.4 Wave Feedback

Wave formation and collapse cause both Mach number and temperature to fluctuate periodically. The cycling of these quantities is largely a consequence of wave cycling rather than a driving factor. However, both provide feedbacks that influence the wave physics. As a wave rises, steam decelerates on its windward side and accelerates through the reduced-area opening above the wave crest (

Figure **2.17**). Droplet shedding and wave disintegration visibly disrupt the steam flow. Though not explicit in

Figure **2.17**, small portions of the flow reach Mach 1. Steam acceleration further decreases pressure above the wave crest, which enhances the wave-lifting force. The transition of daughter wave geometry from rounded to pointed in frame 8 leads to a zone of low Mach number on the leeward side. As the parent wave is still accelerating the steam, the daughter wave causes the steam to accelerate further upstream. The time-averaged

Mach number contour in Figure 2.18 confirms an average nozzle effect, and it is only because of this effect that the steam reaches transonic speeds. For the current geometry, the vena contracta is located halfway across the beach; this may shift as the geometry or flow conditions are altered. The Mach number profile at this location is displayed in Figure 2.18.

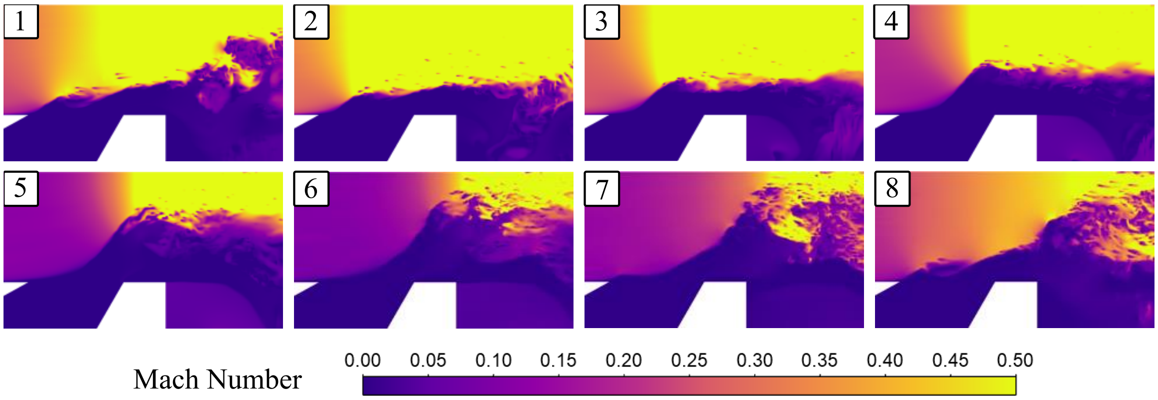

Figure 2.17 Sequential side contours of steam Mach number through one typical wave cycle for the Ref-3 mesh.

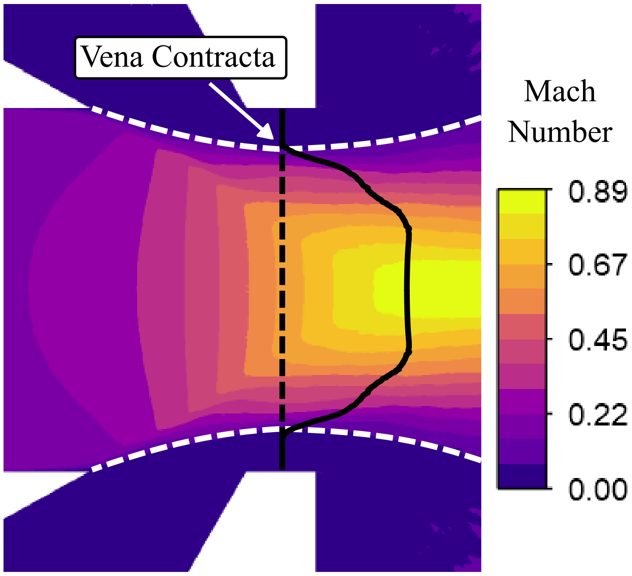

Figure 2.18 Contour of time-averaged Mach number for Ref-3.

Rapid compression and decompression of steam through a wave cycle causes thermal cycling in the windward side (Figure 2.19). Wave formation leads to steam heating (frames 3-7) while collapse leads to cooling (frames 8-2). Increase in puree temperature will lower its viscosity. Apparently, strain rate primarily drives puree viscosity; the high-viscosity region in the well (Figure 2.15) does not generally correspond to any low-temperature regions. However, higher temperatures would contribute to early disintegration by viscosity reduction. Sheltering by a newly forming wave reduces temperature locally (see low-temperature leeward regions in frames 8 and 1). It is possible that steam condensation occurs at the lower temperatures, but this is not accounted for in the CFD model and is a limitation of our simulations.

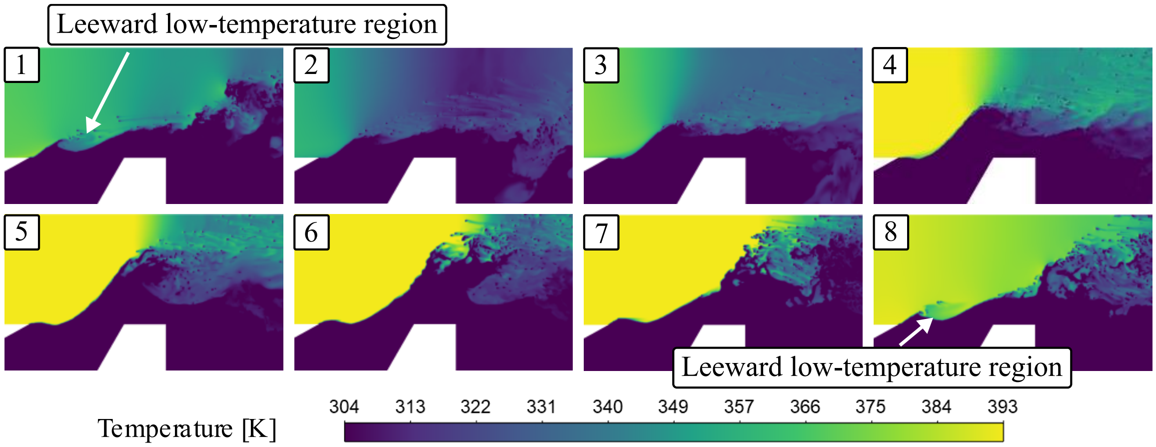

Figure 2.19 Sequential side contours of temperature through one typical wave cycle for the Ref-3 mesh.

2.3.5 Effect of Turbulence

The battle between surface tension (stabilizing) and turbulent forces (destabilizing) is largely won by surface tension for our feed turbulence conditions. Figure 2.20 shows contours of the turbulent Weber number (W_t), which is the ratio of these two forces and defined in Equation 2.8. Here, ρ_g is the density of the gas phase (steam), u' is the rms of the velocity fluctuations, L is the integral length scale, and σ is again the surface tension of the liquid phase (puree). These approximations are used: $u' = 2k$ and $L = \sqrt{k}/\omega$, where k and ω are the TKE and specific dissipation rate, respectively.

$$W_t = \frac{\rho_g {u'}^2 L}{\sigma} \tag{2.8}$$

W_t is highest on the windward side of the rising wave (frames 1, 2, and 8), just after the daughter wave geometry transitions from rounded to pointed and flow separation occurs. It appears that the wave is shear sheltering beginning in frame 8, stagnating TKE production and increasing L. TKE production in the free stream shear layer increases u' and thus W_t. Since W_t is largely less than 1, surface tension is balancing RANS modelled fluctuation inertial effects, indicating that other mechanisms besides turbulence (primarily KHI) are responsible for wave formation for our turbulence feed conditions.

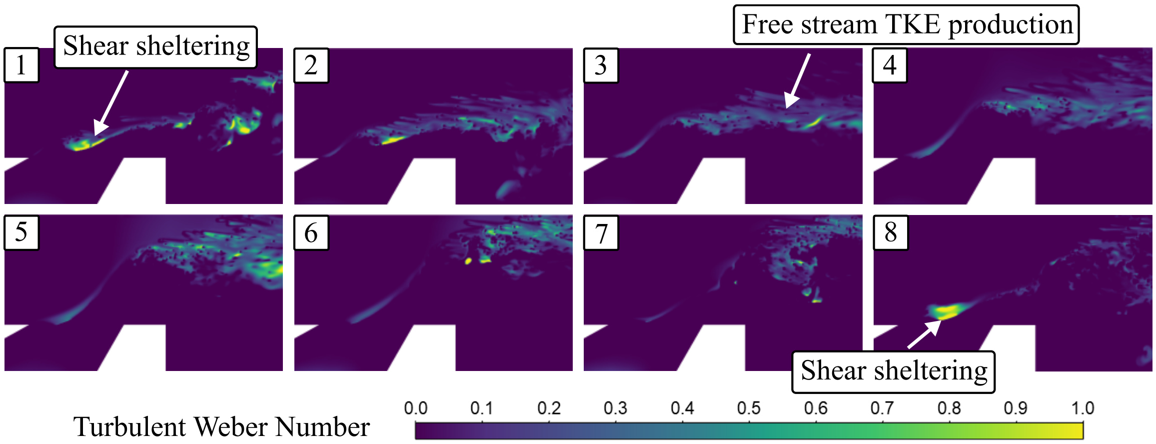

Figure 2.20 Sequential side contours representing turbulent Weber number ($\boldsymbol{W_t}$) through one typical wave cycle for the Ref-3 mesh.

Also, for our particular turbulence feed state, the integral length scale near the wave (see Figure 2.21) is more than two orders of magnitude smaller than the wavelength. In other words, the approximate length scales of the largest, anisotropic, energy-containing structures are too small to influence the birth and death of a wave. From this we conclude that the effect of turbulent structures on wave formation is minimal, confirming that our previously validated RANS approach is sufficient for the present study. The relevance of turbulent structures is, however, expected to depend on the GLR. According to the Phillips mechanism, turbulent eddies can play a significant role in the initial formation of free-surface waves,[4] but we remind the reader that this system does differ from that of free-surface waves.

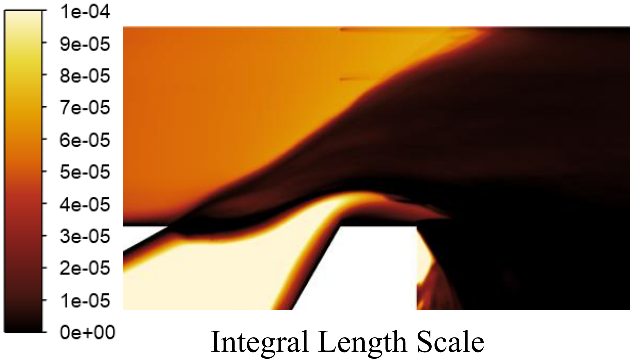

Figure 2.21 Time-averaged integral length scale (***L*** in meters) contour for Ref-3.

2.4 Conclusion

We have performed a numerical investigation of wave formation inside a twin-fluid atomizer nozzle. The context for wave formation in this study is unique in multiple ways, and to our knowledge, this work represents the first study of non-Newtonian transonic periodic wave formation in an enclosed channel with a high blockage ratio. With a GLR of 2.7%, injection of banana puree into a central steam pipe leads to periodic wave formation, which has important implications for atomization systems. No train of waves exists; the formation of one wave corresponds to the collapse of the prior wave. Though each wave is unique, wave cycle frequency, angle, and wavelength are consistent at 1000 Hz, 50° and 0.7 nozzle diameters, respectively.

Wave formation is initiated by KHI, where the puree wave pool provides a vehicle for interfacial deformation. In addition to steam shear and KHI, the reduction in steam flow area and reduced puree viscosity encourages accelerated wave growth. Sheltering by the developing wave compresses the steam, which generates considerable pressure build-up and truncates wave life. As the wave passes the nozzle exit and peaks in height, pressure overcomes inertia and surface tension. The wave begins to collapse and disintegrate, and pressure propagates through the wave to move puree radially outwards. The periodic compression and decompression of the steam produces pressure, temperature, and velocity cycling and feedback. Axial steam pressure fluctuations most probably contribute to wave formation, adding to the Bernoulli effect, and higher temperatures reduce puree viscosity. The reduction in effective orifice exit area by waves produces a nozzle effect to accelerate the outgoing steam above the wave crest, decreasing pressure and increasing the lifting force. Turbulence was shown to have minimal effect on wave formation, though this is undoubtedly a function of GLR and feed turbulence conditions.

We have revealed for the first time what we term “wave-augmented varicose explosions” (WAVE). Now that it has been demonstrated, the dependency of WAVE on various parameters can be investigated. Future efforts might explore the general dependence of wave formation on GLR. The response of a Newtonian fluid in this system might also be of interest to determine the precise role of viscosity in wave formation. Finally, an evaluation of wave dependence on geometric parameters could enable nozzle design optimization.

CHAPTER THREE

A SPRAY OF PUREE: WAVE-AUGMENTED TRANSONIC AIRBLAST NON-NEWTONIAN ATOMIZATION

3.1 Introduction

Atomization is as ubiquitous as it is useful. The disintegration of liquids in sprays finds application in a wide range of industries, touching many aspects of modern life. Such importance makes the underlying physics a significant object of research. Various methods are used to disintegrate liquids, but at the heart of each is a means to destabilize the liquid. Two significant means are the Kelvin-Helmholtz instabilities (KHI) and Rayleigh-Taylor instabilities (RTI). KHI is a shear-flow instability that amplifies interfacial irregularities via induced pressure gradients, while density gradients induce RTI, leading to fingering. Both contribute to destabilization, ligament formation, and droplet breakaway.

A plethora of techniques are employed to enhance liquid destabilization and atomization in spray processes. Swirl[45-47] and effervescence[48, 49] have both been shown to be useful for atomization. Zhang *et al.* found that adjusting the misalignment of impinging jets could provide an effective means to optimize propellant mixing and atomization.[50] Surface acoustic waves have been used to generate aerosol droplets. The experimental and numerical work of Qi *et al.* elucidated interfacial destabilization mechanisms driving this process.[51] Meacham et al. investigated droplet formation from a micromachined ultrasonic droplet generator.[52] Twin-fluid (or airblast) atomizers are widely employed and use an assisting gas to facilitate liquid disintegration. Twin-fluid designs typically involve a central liquid flow surrounded by a co-axial gas flow. Charalampous *et al.* found the complexity of the full spray in co-axial airblast atomizers (measured by energy of PID modes) to be inversely proportional to the gas-to-liquid momentum ratio.[53] In their study of internal-mixing twin-fluid atomization, Zu *et al.* showed that the spray far-field is dominated by coalescence, resulting in a linear increase in droplet size in the axial direction.[54] Kumar and Sahu used shadowgraphic imaging to demonstrate that near-nozzle unsteadiness in a twin-fluid injector can affect spray characteristics far downstream.[55] Turbulence can also drive atomization and dictate droplet sizes by the Hinze scale. Ling *et al.* explored the effect of turbulence in their numerical study of a two-phase mixing layer.[56] Droplet sizes did not match the Hinze scale, leading them to conclude that turbulent velocity fluctuations were not the dominant breakup mechanism.

Atomization takes on different characteristics when the fluid is non-Newtonian. For example, Zhao *et al.* reported a different breakup mode for secondary atomization of coal water slurries that does not appear for Newtonian fluids.[57] Non-Newtonian fuels have been atomized effectively in an annular jet rather than ejection as a liquid core. A study of power-law fuel in an annular jet by Guo *et al.* found that for high-speed jets, the central gas flow promotes instability.[58] Two additional factors that enhance breakup, according to the study, are a thinner annular fuel film and increased gas density. In general, they note increased instability in pseudoplastic fluid annular jets. Successful atomization is made more challenging when the fluid is also highly viscous, as additional resistance must be overcome. Strasser found that there is a balance between annular sheet thickness and gas momentum for a given external nozzle diameter.[36] Among other applications, understanding the breakup of non-Newtonian visco-elastic sheets is important for propulsion systems using gelled propellants.[59] The gas-liquid mass ratio (GLR) might be increased to maximize disintegration, but that reduces atomizer efficiency.[60] Methods of increasing atomization effectiveness at lower GLRs (higher efficiency) are desirable, such as the internal mixing design proposed by Padwal and Mishra.[37, 61]

This paper presents unique mechanisms to enhance atomization of viscous, non-Newtonian fluids by means of internal wave generation in a pre-filming twin-fluid atomizer. Banana puree is the working fluid and is shear-thinning beyond a yield stress. The “original” banana puree production process (by means of an infant) is humorously illustrated in Figure 3.1. In the twin-fluid atomizer, an annular puree flow surrounds a central steam flow into which the puree is injected just before the nozzle exit. The inversion of feeds (that is, an annular liquid flow surrounding a core gas flow), has been shown to effectively atomize viscous, non-Newtonian waste slurries with reduced gas flow rates and accommodate variable-viscosity biosludge via smart atomization technology.[18, 36] The atomizer geometry employed for the present study was first presented by Strasser and was shown to facilitate superior atomization of viscous slurries compared to other configurations tested.[36] The GLR of 2.7% used here is equivalent to the lowest studied by Padwal and Mishra for reduced-GLR atomization of gelled propellants.[37] Puree waves form inside the nozzle that cause a pulsing flow and serve to accelerate disintegration in what we term “wave-augmented atomization.” The physics and mechanisms driving initial wave formation have been described in Ref. 61.[62] The KHI dominates during wave formation until pressure forces overcome inertia resulting in wave collapse. Understanding the resulting pulsing cycle and how waves enhance atomization is the central feature of this paper. Spatiotemporal correlations are discussed in Ref. 20.[20]

1. Intrigue 2. Consumption 3. Processing

3. Delight 4. Shear 6. Puree

Figure 3.1 Illustration of the “original” banana puree production process.

3.2 Methods

3.2.1 Computational Methods

The computational methods employed in this study have been presented in detail in Ref. 61, but they will be summarized here. ANSYS Fluent 2020R1 was used to numerically solve the compressible Reynolds-Averaged Navier-Stokes and volume-of-fluid (VOF) equations. Steam is treated like an ideal gas, and puree is considered incompressible. Turbulence was approximated using the shear stress transport (SST) k-ω model, and Geometric Reconstruction (PLIC) was utilized to explicitly reconstruct the puree-steam interface.[26] A SIMPLE pressure-velocity coupling scheme was employed with a largely second order discretization scheme. A Courant number of around 1 was maintained by a variable time step that remained on the order of 1×10^{-8} s for most rigorous mesh, which amounts to about one-hundred-thousandth of an atomizer pulsation cycle. The method employed herein has been extensively validated for transonic atomization of a different non-Newtonian fluid.[24, 26-34] Validation efforts include both qualitative and quantitative reproduction of experimental results, such as the globally pulsing nature of the system, the acoustic signature, and the primary atomization ligament wave positions.[62] Furthermore, the results presented here correspond to the globally varicose pulsing nature expected for similar atomization systems (recessed, inverted feed, high gas-to-liquid momentum ratio).[35] More discussion on validation can be found in Ref. 61.

Volume-averaged Sauter mean diameter (SMD) was collected across 10 axially-segmented volumes equally divided along the atomizer axis from the nozzle exit to the far end of the domain.[29] These volumes will hereafter be referred to as "buckets." We considered models at quasi steady state (QSS) when all 10 SMD signals stabilized, as well as various point-monitored quantiles like velocity and turbulent kinetic energy. Any time-averaged quantities presented have only been averaged across QSS data. The approximate time between each pulsing sequence, what we call the pulsing cycle time scale, is used to normalize flow time. "Pulsing times" (PTs) in this document are equivalent to "wave times" (WTs) in Ref. 61; both waves and pulses are part of the same general cycling phenomenon. The final Ref-3 mesh (further detailed below) ran for 12 WTs at QSS with 8.5 WTs of time-averaged data. Further details of run time and hardware utilized for each mesh evaluated is presented in Ref. 61.

3.2.2 Mesh and Boundary Conditions

Again, the reader is encouraged to reference Ref. 61 for details regarding geometry, mesh, and boundary conditions, but a summary is provided here. The twin-fluid atomizer follows an unconventional (for two-stream atomizers) design: steam flows inside a central pipe into which puree is injected from an outer annulus. The nozzle is extended to force the steam and puree to interact *before* exiting, termed "forced interaction."[36] Beyond the nozzle exit, the computational domain extends 2 and 1.5 nozzle diameters in the axial and radial directions, respectively. Though we do expect continued droplet breakup (secondary atomization) beyond the end of the computational domain, the focus of this work is on primary atomization near the nozzle. Banana puree viscosity is described by the Herschel-Bulkley model, shear-thinning beyond a yield stress, based on experimental data.[38] The computational domain includes a 90° azimuthal slice with periodic boundary conditions to represent the entire 360° azimuth. Constant mass flow rates at the steam and puree inlets are set to a GLR of 2.7%. Relatively simplistic boundary feed turbulence quantities are chosen for the purposes of this study: spatially constant values of k = 48 m^2/s^2 and ω = 2.5×10^5 1/s. Given that the steam feed conditions may influence atomization, the results of our study should be interpreted in light of these conditions; sensitivity analyses could be conducted should one want to study other feed conditions, such as fully developed steam pipe flow.

A 132 million element mesh, labelled Ref-3 and shown in Figure 3.2, was found to provide reasonably mesh independent results after assessing a range of refinement levels. Several metrics were evaluated, including turbulent kinetic energy, velocity, and puree volume fraction at the nozzle exit, all of which show the Ref-3 mesh close to convergence. The Ref-3 mesh, then, is sufficient for the purpose of identifying the major patterns and mechanisms at work in this wave-augmented atomization process. Additionally, the primary mechanism of interest, wave formation in the nozzle, was shown using a mesh that is two refinement levels below Ref-3 with essentially the same physics (for example, system pulsation frequency, wavelength, and time-averaged volume fraction at the nozzle exit). Although mesh independence has largely been addressed in Ref. 61 with a focus on wave physics, it will be revisited here in the context of SMD. The vast majority of computational elements are hexahedral, while there is a small fraction of triangular prism cells. Unless otherwise noted, all results presented in this paper were obtained with the Ref-3 mesh. To assist in our continued mesh independence discussion, however, "Ref-3" indicates a Base mesh that was refined 3 times, with intermediate meshes Ref-1 and Ref-2. When a given mesh is refined, each cell length is cut in half, effectively increasing the total mesh element count by a factor of eight. Element counts range from 0.3 million for the Base mesh up to 132 million for the Ref-3 mesh. Other mesh variations considered were Ref-2-45 and Ref-3-AMR. Ref-2-45 is equivalent to Ref-2 but with 45° rather than a 90° azimuth. Ref-3-AMR is equivalent to Ref-3 but uses adaptive mesh refinement (AMR) instantaneously while the solver proceeds for the third refinement level, maintaining around 28 million elements on average. AMR saves computational cost by dynamically refining the mesh only in localized areas to resolve the puree-steam interface and has been used to study atomization.[50] However, Ref-3-AMR was found to produce outliers to the trend of numerical results with mesh size; for this reason, it was not considered a sufficient substitute for Ref-3, despite its computational savings. A detailed comparison of Ref-3 and Ref-3-AMR is presented in Ref. 20. Hardware was optimized according to a novel methodology developed by Prichard and Strasser.[41]

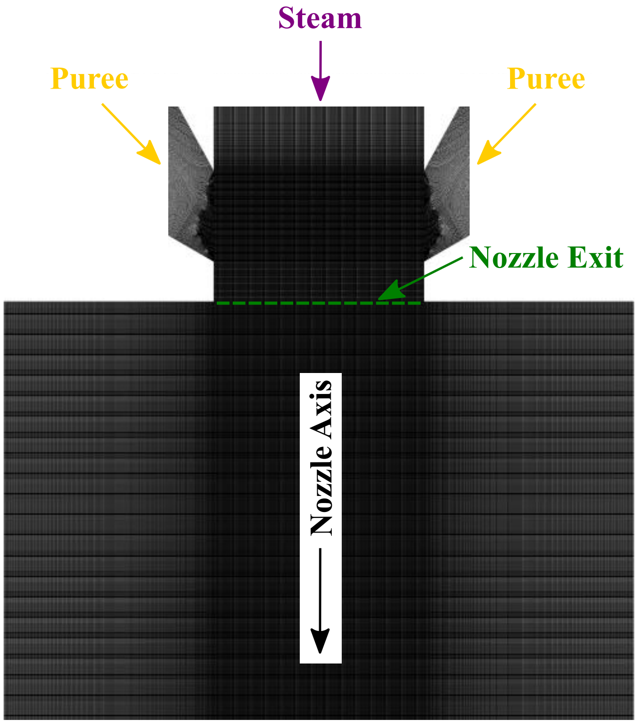

Figure 3.2 Side view of the Ref-3 mesh (132 million elements) with important features labelled.

3.3 Results and Discussion

3.3.1 Pulsation Characteristics

Annular injection of banana puree into the central steam flow leads to a unique pulsing sequence. An overview of the general pulsing sequence is provided in Figure 3.3, and it consistently operates with a frequency of 1000 Hz. The formation of waves inside the nozzle plays a crucial role in this atomization process, which we refer to as "wave-augmented atomization." A given pulsing sequence includes three stages: stretch, bulge, and burst. First, the puree stretches down from the nozzle in an annular sheet (frames 1-3). The stretch stage roughly corresponds to wave formation inside the nozzle. Second, the puree is pushed radially outward, causing a bulge in the puree sheet and corresponding to wave collapse (frames 4-5). Finally, the puree sheet ruptures in a radial burst (frames 6-8), enhancing puree disintegration and droplet formation. Puree chunks continue to disintegrate as they move farther away from the nozzle.

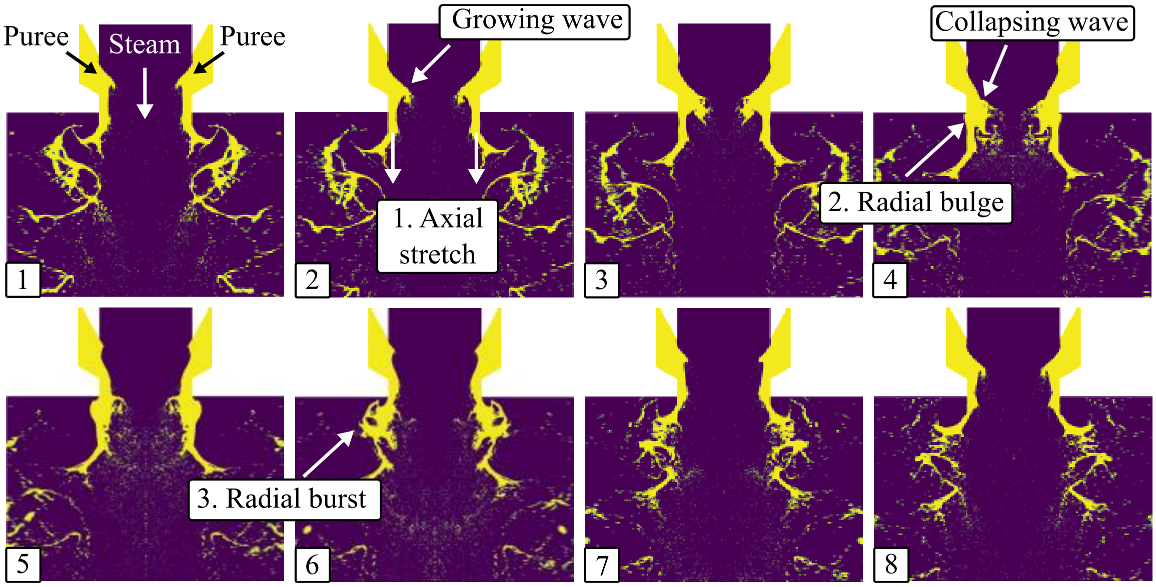

Figure 3.3 Sequential side views of banana puree (yellow) through one typical pulsing cycle.

The pulsing cycle viewed in three dimensions from outside the nozzle is presented in Figure 3.4, where the banana puree surface is colored by strain rate. The same three stages are observed: stretching in frames 3-5, bulging in frames 6-7, and bursting in frames 8-2. The non-uniformity of the annular puree sheet is visually evident and leads to significant azimuthal variability during the radial burst event (frame 8). As one would expect, strain rate is highest closest to the central steam flow. The contrast in strain rate between the inside and outside of the puree sheet is particularly clear in frame 7, and by frame 8, high strain rate is propagating radially outwards. As a precursor to the primary radial burst event, portions of the puree sheet begin rupturing below the bulge line, likely because the puree sheet has thinned out. As the sheet bulges, gradients in strain rate increase around the bulging area, culminating in the radial burst.

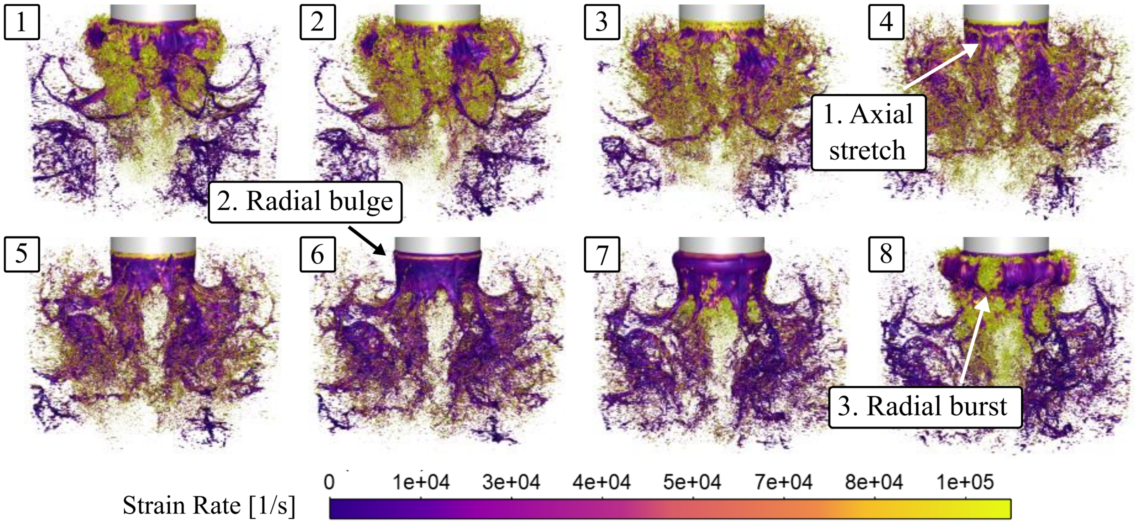

Figure 3.4 Sequential views of puree atomization through one typical pulsing cycle, where the puree surface is colored by strain rate.

Reynolds, Weber, Ohnesorge, and Strouhal numbers characterize the flow and atomization process. It was shown in Ref. 61 through non-dimensional analysis that gravitational effects are not important for this system. Reynolds number ($Re = \rho V_b D_o / \mu_l$), which compares inertial to viscous effects, is 1.1×10^5. The majority contribution to the bulk velocity is from the steam, highlighting its importance in overcoming the retarding effect of puree viscosity. The Weber number ($We = \rho_g V_g^2 SMD / \sigma$), which compares inertial to surface tension effects, is 102. The cohesive surface tension force is largely dominated by disruptive inertial forces for puree disintegration, and $We = 102$ indicates the likelihood of secondary breakup via "bag-and-stamen" or "sheet stripping" mechanisms.[63] The Ohnesorge number ($Oh = \mu_l/\sqrt{\rho_l SMD \sigma}$), equivalent to $\sqrt{We}/Re_{SMD}$, is 0.05, indicating that viscous effects on secondary breakup are relatively small for our droplet sizes. Oh has been correlated with the critical We, below which no droplets will experience secondary breakup, with $Oh < 0.1$ indicating a critical We of around 12.[63] As droplet sizes decrease axially way from the injector, We decreases while Oh increases. The Strouhal number ($St = fD_o/V_b$), which is a non-dimensional frequency, is 0.1. St essentially compares the system time scale to the pulsation time scale; the low value of St indicates that the system likely has time to re-equilibrate between pulses. Here, ρ_l is the puree density, ρ_g is a representative steam density, ρ is the average density across phases, D_o is the orifice diameter, V_b is the bulk velocity of both phases, V_g is the inlet steam velocity, μ_l is the puree dynamic viscosity, and f is pulsation frequency. Re_{SMD} is the Reynolds number calculated using SMD as the characteristic length rather than orifice diameter. For puree viscosity in each of these expressions, a representative value is used that approximates μ_l in the highly atomized region. SMD close to the nozzle outlet is used as a representative droplet diameter. V_g approximates the relative velocity between steam and droplets around the nozzle exit.

Mach number cycles with the pulsing sequence as shown in Figure 3.5. Steam accelerates as banana puree reduces the effective nozzle exit flow area and reaches transonic velocities. Thought not explicitly shown in Figure 3.5, small portions of the flow reach Mach 1 at times. Contact with puree lowers the temperature of the steam, which in turn reduces the local speed of sound. Consequently, puree in Figure 3.5 is effectively outlined by high Mach regions. Frame 5, the peak of bulging, marks the low point of Mach number throughout the domain. By the radial burst in frame 6, high Mach steam flow is propagating axially. Also observed are high Mach numbers around the radial burst as puree accelerates radially outward.

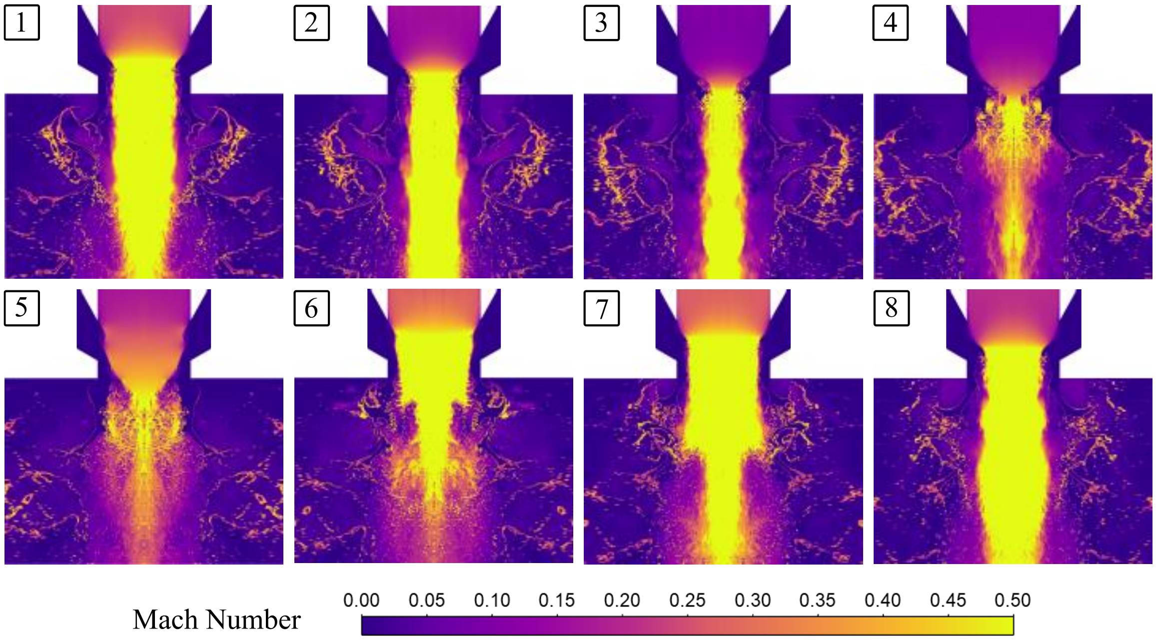

Figure 3.5 Sequential side contours of Mach number through one typical pulsing cycle.

Temperature also cycles with the pulsing sequence as steam is compressed and interacts with puree. Higher temperatures will reduce puree viscosity to enhance atomization. The central steam flow downstream of the orifice reaches an overall peak temperature in frame 2 of Figure 3.6 during the stretch stage. It is in frame 2 that the balance between steam compression and steam flow restriction is optimal for propagating high temperature steam downstream of the orifice in the central flow. The quantity of puree droplets in the central steam flow is also lowest in frame 2, so puree-steam interaction is minimal. After exiting the nozzle, central steam flow temperature is significantly lower than the steam pipe inlet temperature of 393 K, and steam temperature has largely been reduced to that of the puree radially beyond the nozzle width.

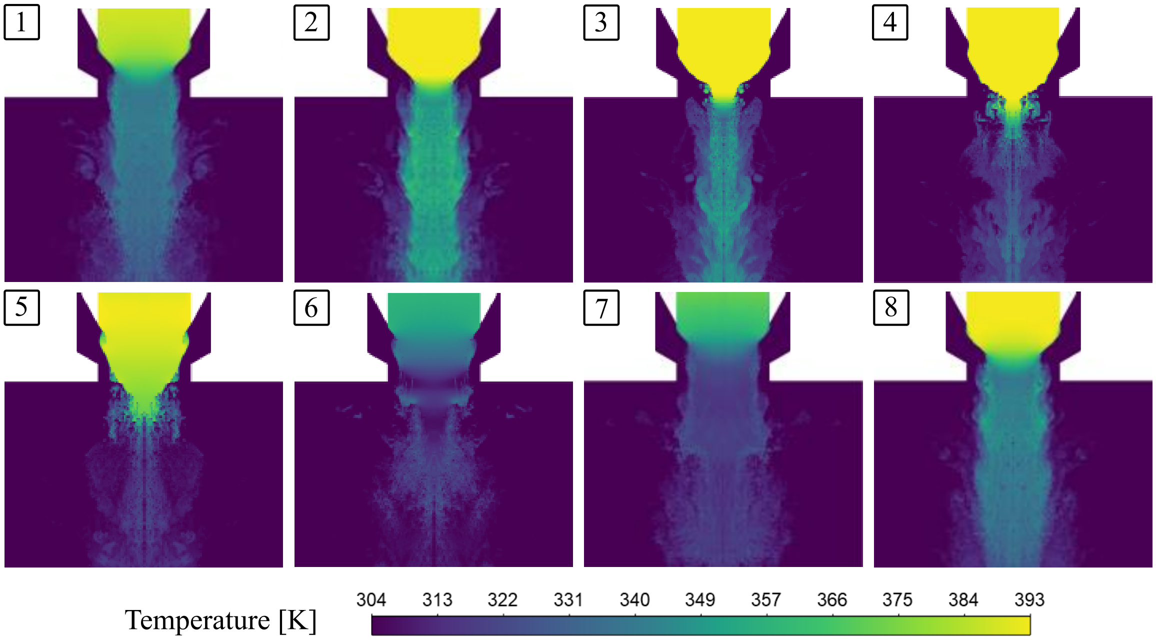

Figure 3.6 Sequential side contours of temperature through one typical pulsing cycle.

Three time-averaged contours are shown in Figure 3.7. From left to right, they are contours of puree volume fraction, Mach number, and the turbulence integral length scale (L). As is evident from earlier in Figure 3.3, beyond the nozzle exit, only the smallest droplets follow the central steam flow, and the majority of puree moves in the annular region outside of it. The time-averaged spray angle is about 64°. On average, the steam accelerates through the nozzle exit, though the high-Mach region gradually diffuses moving axially away from the injector. In the central flow downstream of the orifice, L is an order of magnitude lower than the droplets at their smallest in the model for our particular set of feed conditions. This would indicate that turbulence is not a dominant mechanism in droplet formation. However, our estimation of *L* could be off by an order of magnitude, in which case the largest structures could still influence droplet physics. Therefore, we are ignoring smaller droplets, secondary breakup, and any interactions between droplets and large eddies. These conditions are acceptable since our focus is on primary atomization. A large eddy simulation (LES) is possible for a future effort, but it would likely require 1/10th the mesh length scale.

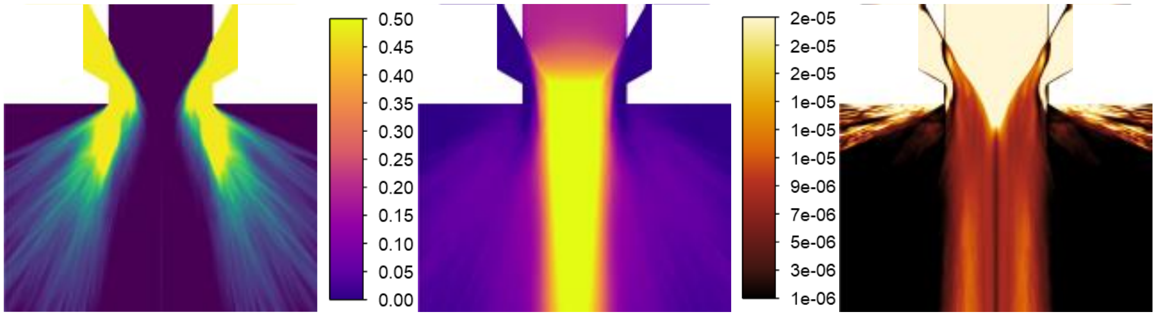

(a) Puree Volume Fraction (b) Mach Number (c) Integral Length Scale

Figure 3.7 Contours of time-averaged quantities: (a) puree volume fraction, (b) Mach number, and (c) integral length scale.

3.3.2 Atomization Mechanisms

Wave formation inside the nozzle is crucial to disintegrate the viscous banana puree. Each wave augments the atomization process via at least three mechanisms: 1) internal pressure buildup, 2) wave impact momentum, and 3) droplet breakaway. A fourth mechanism, effervescence, is speculated to contribute (and would be a direct consequence of wave collapse), though this is not able to be confirmed by visual inspection. Each of these mechanisms will be detailed in the proceeding discussion. Since banana puree is shear-thinning, any disturbance that involves shear is going to be enhanced by a reduction in viscosity. Geometric features must contribute to wave formation and therefore atomization,[62] but that is not the focus of this study. Evaluations of wave-shaping geometry is needed to fully understand the effect on atomization.[27]

As a wave peaks, its momentum is largely directed axially. Wave collapse is marked by a shift in momentum towards the radially outward direction by about 30°. Figure 3.8 illustrates this momentum flow. The average momentum flux rate in the radial direction as a given wave collapses is 1.7×10^5 kg/m-s^2. There is only steam outside of the puree sheet, leaving the targeted sheet free to bulge and burst from the wave impact. It is well-known that bubbles form in breaking waves.[42, 64] Effervescence would accentuate instability by pre-breaking up the puree. Additionally, heat transfer from steam bubbles would reduce viscosity *within* the puree sheet. It is hypothesized that puree droplets around the ruptured sheet provide an order of magnitude estimate for bubble size, which is 0.5 mm.

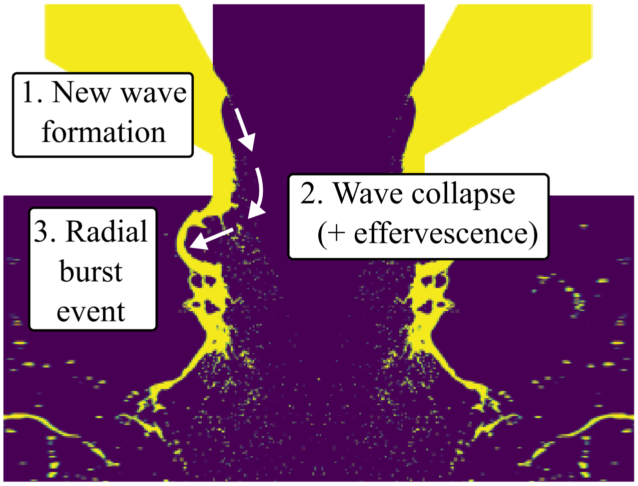

Figure 3.8 Momentum flow of a typical wave through three stages: 1) wave formation,[62] 2) wave collapse, and 3) radial burst.

In addition to effervescence, several other mechanisms “prime” the annular puree sheet for rupture. The impact of the wave itself will cause irregularities in the sheet. RTI, which are induced by density gradients, cause azimuthal excitement of perturbations (see azimuthal ripples in Figure 3.9, which is a zoomed in 90° azimuthal view. The strong azimuthal variation in Figure 3.9 confirms the sufficiency of a 90° wedge model.) Temperature-induced puree density variations (which are not included in our CFD model) would affect RTI, but we expect this to be minimal, as any puree density variation would be small relative to the difference in steam and puree densities.[39] RTI also cause fingering, both from the puree sheet and the “arms” stretching from it in Figure 3.9. Furthermore, since the puree is shear-thinning, viscosity gradients increase instability to prime the sheet for rupture. Puree viscosity is lowest inside the puree sheet (adjacent to the central steam flow) due to high strain rate. Viscosity outside the puree sheet peaks during the stretch stage but with significant gradients (frame 6). As a radial burst event occurs, rapid shear-thinning is evident.

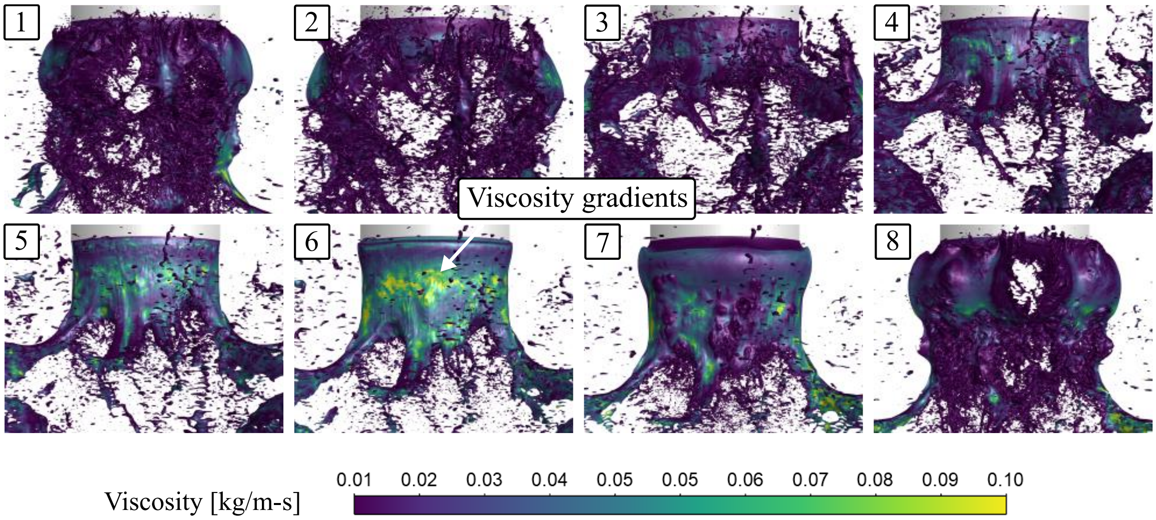

Figure 3.9 Sequential views of puree atomization through one typical pulsing cycle, where the puree surface is colored by puree viscosity.

High pressure inside the puree sheet compliments wave impact (pulsing events introduced in Ref. 61); these are the two driving forces behind the radial burst event. Pressure contours in Figure 3.10 show pressure cycling in the nozzle. As puree stretches out from the nozzle, steam compresses and builds pressure upstream inside the nozzle (frames 2-3). As the wave collapses, the high pressure spreads out of the nozzle to the inside of the puree sheet (frames 4-5). The transition from frame 5 to frame 6 marks the radial burst, driven by the pressure difference across the puree sheet. Pressure is rapidly diffused, exploiting the irregularities and instabilities of the puree sheet.

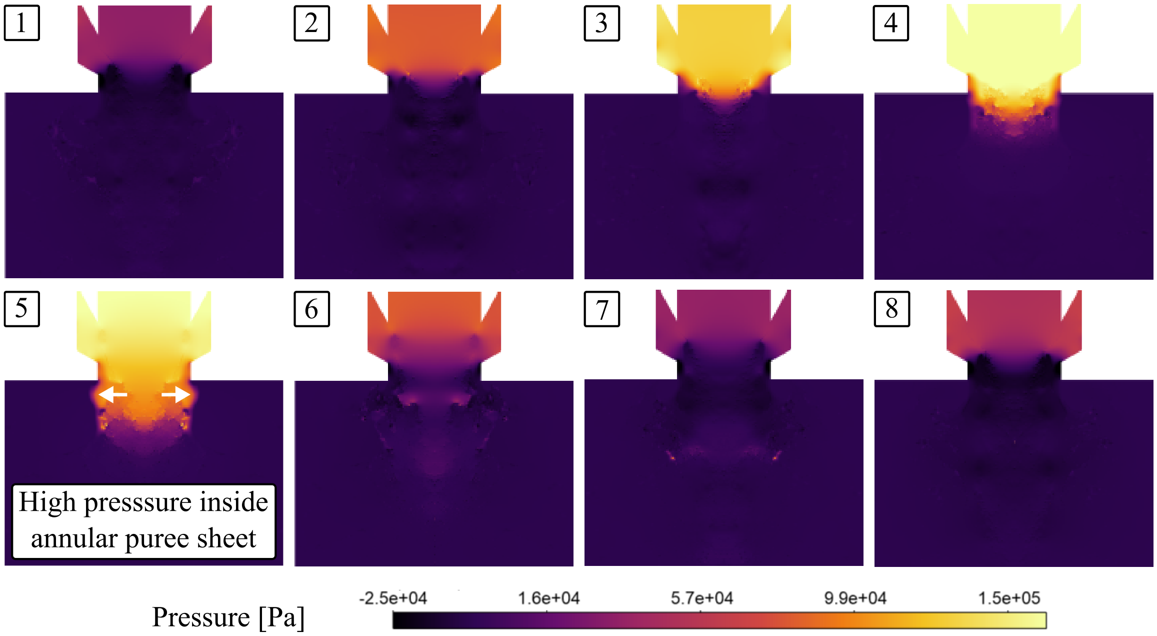

Figure 3.10 Sequential side contours of pressure through one typical pulsing cycle.

Apart from disintegration of the puree sheet, which is the primary atomization process of interest, droplets also break away from the tips of the waves as they penetrate into the steam flow. Some droplets are stripped off by shear while the wave is forming,[62] but most break away during wave collapse and disintegration. Strain rate is highest where the high-velocity steam flow encounters puree droplets. Consequently, contours of strain rate in Figure 3.11 highlight where droplets break away from the waves. The most prominent regions of high strain rate are in frames 4 and 5 during wave collapse. Although the central steam flow is largely devoid of puree compared to other regions downstream of the orifice, each time a wave collapses, a group of droplets passes through the central flow. In frame 5, the strain rate of any magnitude is largely concentrated in the central steam flow, but the radial burst in frame 6 starts the radial spread of strain rate, which continues through frame 3. High strain rate lowers viscosity, which encourages atomization.

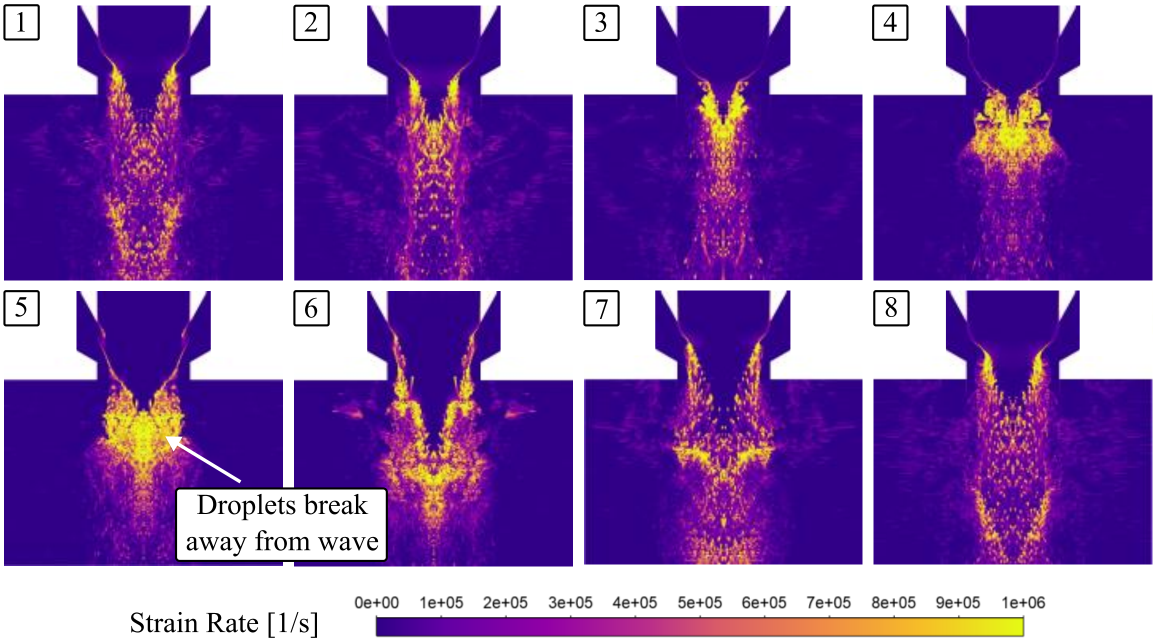

Figure 3.11 Sequential side contours of strain rate through one typical pulsing cycle.

3.3.3 Droplet Sizes

Our sampling time for SMD signals is sufficient based on the convergence in Figure 3.12. The cumulative mean and standard deviation of SMD in bucket 1 have reasonably converged within the QSS sampling window (note that this is not the total number of pulsing times since the start of the model). Bucket 1, which is adjacent to the nozzle, displays the greatest temporal variability in SMD, making its convergence of the greatest importance.

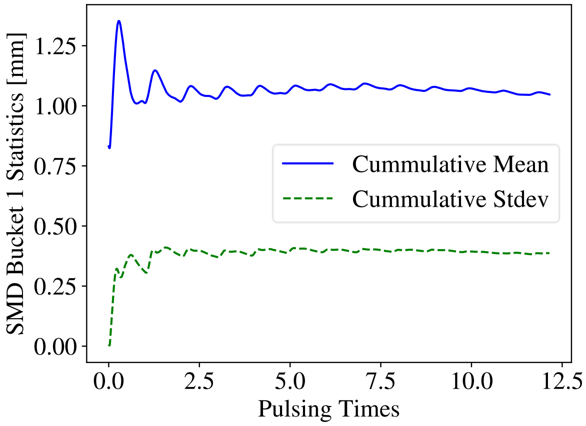

Figure 3.12 Cumulative mean and standard deviation of SMD demonstrates sufficient sampling time to report time-averaged values.

The time-averaged axial SMD profiles in Figure 3.13 for all meshes are remarkably consistent in shape, indicating similar atomization physics. SMD steadily decreases moving away from the nozzle due to wave-augmentation and then secondary breakup. The Base profile conforms the least to the general trend with a gentler slope at the nozzle exit. This corroborates our visual inspection of a marked change in physics from Base to Ref-1, where Base does not produce a periodic pulsing sequence.[62] Reducing the azimuthal domain extent from 90° to 45° makes no difference to the axial SMD profile, indicating that 90° is more than enough to capture this atomization process. Though similar, the Ref-3-AMR profile differs from that for Ref-3. AMR seems to slightly alter droplet formation, which was suggested in Ref. 61 (in terms of wave physics) and is explored more thoroughly in Ref. 20. The successive decrease in difference between Base, Ref-1, Ref-2, and Ref-3 demonstrates sufficient mesh independence for the purposes of this study. An additional level of refinement would be expected to produce very small reductions in droplet size. Ref. 61 details mesh independence by additional metrics.

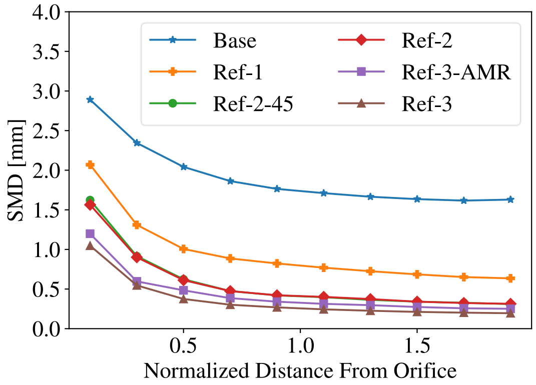

Figure 3.13 Time-averaged axial SMD profiles for all models.

Even towards the end of the modeled domain, Ref-3 maintains at least four cells across each droplet.[32] Figure 3.14 shows the mesh length scale (MLS) required for four cells across each droplet for Ref-3, which follows the shape of the SMD profile in Figure 3.13. Mesh size is axially uniform from the nozzle exit to the end of the domain and remains below the required 4-cell MLS threshold, especially in the near-nozzle region.

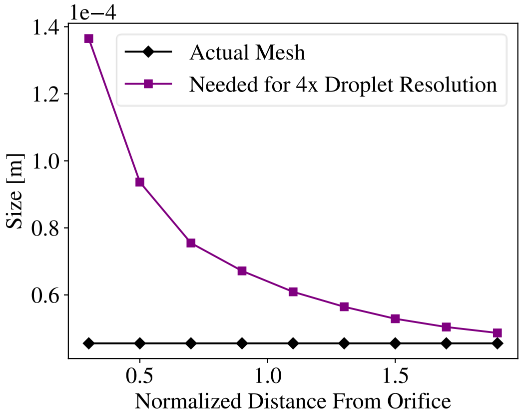

Figure 3.14 Actual Ref-3 mesh length scale compared to that required for four cells across each droplet.

Spatiotemporal variation in SMD is captured by the Hovmöller diagram in Figure 3.15. Periodic fluctuations move axially through the domain in a wave pattern caused by the parent wave. The strong pattern on the left illustrates the periodicity of pulsing near-nozzle atomization physics. Mid-domain fluctuations are less regular, and towards the end of the domain, SMD fluctuates very little. Unsteadiness at the nozzle exit has been shown to maintain some level of influence on the spatiotemporal development of droplets far downstream.[55] After about 1.5 orifice diameters, droplet sizes no longer fluctuate with the pulsing sequence; therefore, wave-augmentation effects are diffused by 1.5 D_o.

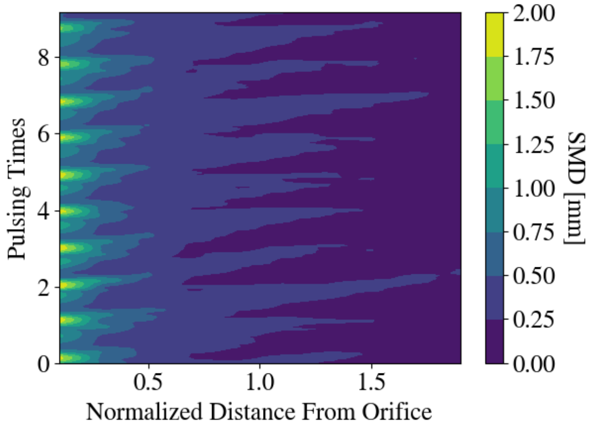

Figure 3.15 A Hovmöller diagram of SMD showing the spatiotemporal variation in droplet size.

3.4 Conclusion

The mechanisms driving inverted-feed, transonic, non-Newtonian atomization augmented by pre-filming wave formation were revealed using computational fluid dynamics. Our working fluid was viscous, shear-thinning banana puree. Injecting puree into a central steam pipe leads to wave formation inside the nozzle and a regularly pulsing puree flow that accelerates disintegration. Such a design is opposite of the conventional two-stream airblast atomizer, where a high-speed gas flow surrounds a liquid core. Wave-augmentation could enhance atomization of other viscous, non-Newtonian fluids, such as manure slurries for energy conversion and fertilizer production or gelled propellants.

A summary of the pulsing sequence and atomization mechanisms is provided here. Pulsing cycles repeat with a frequency of 1000 Hz and are composed of three primary stages: 1) stretch, 2) bulge, and 3) burst. As a wave forms inside the nozzle, an annular puree sheet stretches down from the nozzle around the central steam flow. Ripples and irregularities caused by RTI and viscosity gradients prime the sheet for rupture. When the wave collapses onto the puree sheet, it bulges radially outward, reducing the puree viscosity. Finally, the bulging puree sheet ruptures in a radial burst. Waves drive droplet formation via at least three mechanisms: 1) wave impact momentum, 2) pressure buildup, and 3) droplet breakaway. The first two are driving forces behind the radial burst event; collapsing waves impact the annular puree sheet with an average radial momentum flux of rate of 1.7×10^5 kg/m-s^2. The third results from wave penetration well into the steam flow, where droplets break away from the waves to a lesser degree by steam shear and to a greater degree during wave collapse and disintegration. It is suspected that steam is entrained by the collapsing wave, which would further destabilize the puree sheet. Steam compression inside the nozzle builds pressure on the windward side of a wave. Wave collapse allows the pressure to propagate axially, creating a large pressure gradient across the puree sheet. The instabilities in the sheet are exploited in a violent rupture.

The pulsing nature of the system causes periodic fluctuations in SMD to propagate axially along the atomizer axis in a wave pattern. By 1.5 nozzle diameters from the orifice, however, periodicity is largely diminished. Puree movement was generally outside of the central steam flow, with a time-averaged spray angle of 64°. Future work should assess how geometry changes affect wave-augmented atomization and provide the complete droplet size distribution (rather than merely SMD).

CHAPTER FOUR

SPATIOTEMPORAL CHARACTERISTICS OF WAVE-AUGMENTED VARICOSE EXPLOSIONS

4.1 Introduction

The relevance of atomization for modern life cannot be overstated. Those atomization processes found in nature's designs have been successfully exploited for applications in many industries, such as automotive, aerospace, chemical, and agricultural. Though widely employed, atomization is a complex and diverse process that continues to be studied with great vigor. Various fluid instabilities lead to atomization, and the nature of droplet formation makes atomization an inherently three-dimensional (3D) process. The Kelvin-Helmholtz instability (KHI), induced by velocity gradients, is often a contributor to atomization but is only two-dimensional (2D). For a moving surface, KHI operates in the longitudinal direction to excite the interface, creating perforations, tongues, and waves. Variation in the transverse direction can arise from Rayleigh-Taylor instabilities (RTI), which are induced by a misalignment between the density and pressure gradient vectors; RTI arise from the extra term $\frac{1}{\rho^2}\frac{\partial\rho}{\partial x_i}\times\frac{\partial P}{\partial x_i}$ in the vorticity equation, where ρ is density, P is pressure, and x_i is the direction vector. Additionally, surface curvature can induce Rayleigh-Plateau capillary instabilities (RPI). KHI, RTI, and RPI can be important and simultaneous players in the disintegration of liquids.

Controlled atomization processes utilize a range of methods. Some common types of atomization-enhancing techniques include swirl,[45-47] effervescence,[48, 49] and an assisting gas stream.[53-55] Twin-fluid atomization utilizes a high-speed co-flowing gas stream to disrupt the liquid. Typical designs involve a central liquid stream surrounded by a co-axial gas flow. The gas-liquid shear encourages destabilization of the bulk liquid for disintegration and droplet production. Gas-Centered Swirl Coaxial (GCSC) injector designs have been used for propellant atomization with inverted the feeds.[65] A central gas flow is then surrounded by a co-axial liquid flow, and pulsing characteristics can develop at certain gas-to-liquid momentum ratios.[35] Alekseenko *et al.* studied disturbance waves in vertical annular liquid flow around a central gas stream, but these waves are small relative to the nozzle.[66]

A Newtonian fluid is typical for atomization processes, and non-Newtonian fluids will alter atomization characteristics. Although KHI, RTI, and RPI are, fundamentally, inviscid instabilities, variations in viscosity can both 1) modify the growth of these perturbations and 2) further destabilize the interface. Non-Newtonian fluid layers can be prone to instability even when operating at low Reynolds numbers.[12] When studying a shear-thinning fluid on a slope, Millet *et al.* reported increased celerity and likelihood of instability compared to the Newtonian counterpart.[11] A unique breakup mode for secondary atomization was discovered in the study of non-Newtonian coal water slurries.[57] Guo *et al.* report that the central gas flow promotes instability of high-speed annular power-law fuel jets and that a thinner fuel film and higher gas density also encourage breakup.[58] Both inverted feeds and an extended nozzle orifice ("forced interaction" region) have been shown to be useful for atomization viscous, non-Newtonian waste slurries.[17] Applications could include waste-to-energy conversion via "Smart Atomization" technology[18] and gelled propellant atomization.[37, 59-61]

It has been shown that a certain inverted-feed, forced interaction atomizer design produces periodic, high-blockage-ratio waves inside the nozzle when a viscous, shear-thinning fluid present.[62] Two past numerical studies have investigated aspects of this phenomenon with hot, subsonic steam as the assisting gas and banana puree as the working fluid.[19, 62] Banana puree is both viscous and shear-thinning, with well-recorded viscosity data in the literature.[38] WAVE atomization could be instrumental for manure slurries (energy reclamation) and gelled propellants. A predominantly 2D analysis revealed basic mechanisms driving liquid wave formation and collapse.[62] An investigation of atomization downstream of the nozzle highlighted the importance of waves for transonic disintegration of puree via periodic radial bursting.[19] Since the characteristic wave cycling leads to bursting (that in turn enhances atomization), the process has been termed “Wave-Augmented Varicose Explosions” (WAVE). However, major gaps in understanding the WAVE phenomenon remain. Most importantly, the 3D nature of the interior waves and related instability cycle are almost entirely unexplored. Among the many questions that arise are the following: Where and how do RTI form in the wave prior to rupture, and is enough time in a wave cycle allotted for RTI to develop? To what degree are waves azimuthally uniform? If not, where does the uniformity break down? What mechanism drives droplet breakaway inside the nozzle before the radial burst – is it wave stripping or wave flicking? Do quantities at all locations fluctuate with wave cycles? Do flow metrics correlate with one another at various times and locations?

Adaptive mesh refinement (AMR) was considered as a numerical technique, but initial results showed AMR to be an outlier to numerical trends.[62] Because of the complexity and small scales in these atomization phenomena, it can be computationally expensive to resolve explicitly the gas-liquid interface using CFD. To increase computational efficiency, AMR has been used to model both waves and atomization.[40, 50] Rather than refine all cells within the computational domain, AMR locally and dynamically refines the mesh only around the interface as the simulation proceeds. Despite the benefits of AMR, the aforementioned results indicate a need to further understand how AMR affects simulations. It remains unclear how AMR differs qualitatively and which quantities are most affected by AMR.

In this paper, a numerical study is presented to reveal for the first time the spatiotemporal aspects of WAVE; azimuthal instabilities are a primary focus. Careful evaluation of adaptive mesh refinement (AMR) and how it affects the modeling of banana puree slurry atomization is also an important contribution. Our new findings are communicated in four distinct sections, each of which seeks to address unanswered questions from previous studies. Section 4.1 includes cartesian (unraveled from cylindrical) pictures and animations of the wave (so that the azimuthal variation and onset of RTI is evident), as well as calculations of baroclinic torque and discussion of the liquid viscosity-shear-temperature instability cycle. Section 4.2 presents contours of radial versus axial velocity to elucidate mechanisms for droplet breakaway from the liquid wave inside the nozzle. Section 4.3 provides extensive frequency and correlation analyses across 100 spatially diverse signals, including demonstration of Fast Fourier Transform (FFT) convergence. An analysis of wave cycle timing is also included, showing leading and lagging responses. Finally, Section 4.4 presents a qualitative and quantitative assessment to clarify the effect of AMR on WAVE simulations.

4.2 Methods

4.2.1 Computational Methods

The governing Navier-Stokes equations, formulated for multiphase flow in vector notation, are presented in Equations 4.1-4.3. Symbols in Equations 4.1-4.3 are defined as follows: t is time, u is the velocity vector, T is the static temperature, α is phase volume fraction, ρ is density, C_p is constant pressure heat capacity, ζ is laminar conductivity, μ_t is the turbulent viscosity, Pr_t is the turbulent Prantdl number, p is pressure, g is gravity, F is the surface tension force vector, τ is the laminar shear stress tensor, and τ_t is turbulent shear stress tensor. Properties are arithmetically phase-averaged, the banana puree slurry is modeled as incompressible, and the ideal gas equation of state is used to compute steam density. Temperature effects on puree density are not included.

$$\frac{\partial}{\partial t}(\alpha\rho) + \nabla \cdot (\alpha\rho\bar{u}) = 0 \tag{4.1}$$

$$\frac{\partial}{\partial t}(\rho\bar{u}) + \rho\bar{u} \cdot \nabla\bar{u} = \nabla \cdot (\tau + \tau_t) - \nabla \mathrm{p} + (\rho - \rho_{ref})\bar{g} + \bar{F} \tag{4.2}$$

$$\frac{\partial}{\partial t}(\rho C_P T) + \nabla \cdot [\bar{u}(\rho C_P T)] = \nabla \cdot \left[\left(\zeta + \frac{\mu_t}{Pr_t}\right)\nabla T\right] \tag{4.3}$$

The compressible Reynolds-Averaged Navier-Stokes and volume-of-fluid (VOF) equations were discretized and solved using double precision segregated ANSYS Fluent 2020R1 software. The gas-liquid interface was reconstructed explicitly by means of the geometric reconstruction technique (also known as piecewise linear interface capturing or PLIC).[25, 26] Turbulent effects were included via a homogeneous shear stress transport (SST) k-ω model. SIMPLE (Semi-IMplicit Pressure Linked Equations) was used for pressure-velocity coupling, and mostly second order discretization stencils were employed. With the segregated approach of SIMPLE, pressure and velocity are updated sequentially instead of simultaneously.[23] Time step was varied to preserve a Courant number of 1 throughout the entirety of the simulation. For the finest mesh, the time step was generally on the order of one-hundred-thousandth of a wave/pulsation cycle (1×10^{-8} s).

The Herschel-Bulkley model was used to describe the shear-thinning (beyond a yield stress) and temperature-thinning nature of the slurry. Banana puree viscosity was modeled as a function of both strain rate and temperature according to the data of Ditchfield *et al.*[38] A user define function (UDF) in Fluent computes viscosity (μ) according to Equations 4.4-4.7 from strain rate magnitude ($\dot{\gamma}$) and temperature (T in °C) values. In Equation 4.4, τ_0 is the yield stress, k and n are calculated according to Equations 4.6 and 4.7, $\dot{\gamma}_0 = 10s^{-1}$ is the lower strain rate bound, and μ_0 is the corresponding upper viscosity bound. Although our implementation method used herein matches that of the validated method used in Ref. 66,[67] we sought to further verify our calculations. Instantaneous cell-centered values of strain rate and temperature were collected at five locations (to be discussed more in a future section) within the model for a single moment in time. The viscosity observed in Fluent matched excellently that calculated by hand with Equations 4.4-4.7 (less than 0.005% difference), verifying correct implementation of the viscosity UDF.

$$\mu = \begin{cases} \mu_0, \; \dot{\gamma} \le \dot{\gamma}_0 \\ \frac{\tau_0}{\dot{\gamma}} + k\dot{\gamma}^{n-1}, \; \dot{\gamma} > \dot{\gamma}_0 \end{cases} \tag{4.4}$$

$$\tau_0 = 99.8 - 0.53T \tag{4.5}$$

$$k = 1.2 \times 10^5 T^{-2.5} \tag{4.6}$$

$$n = 0.069 T^{0.41} \tag{4.7}$$

Extensive validation of the methods here employed for transonic wave formation and atomization has already been conducted over the course of the last 10 years.[24, 26-33] The SST k-ω turbulence model, which is employed here, was sufficient to reveal important physical mechanisms. Experimental results were reproduced both quantitatively and qualitatively, and the primary validation exercise are summarized as follows. First, computations revealing the globally pulsing nature of an industrial three-stream air-water atomizer as qualitatively observed in experiments. Second, the experimental acoustic signature of pulsations and primary atomization ligament wave positions were quantitatively reproduced with numerical simulations. Third, the axial droplet size distribution in a non-Newtonian injector from experiments aligned quantitatively with numerical results. Additionally, assessment of droplet size distribution did not significantly alter with changing azimuthal angle, even for 1/32nd of a full 360° azimuth. Fourth, the numerical trajectory of a disintegrating droplet (after exposure to a normal shock wave) matched the analytical trajectory for said droplet. Furthermore, broadly similar atomization systems have been studied (recessed with a high gas-to-liquid momentum ratio and an inverted feed), and we find that the results presented here correspond to the globally varicose (but locally sinuous from the Lagrangian perspective of the flapping annular waves) pulsing nature expected of such systems.[35]

Models were considered to be at quasi steady state (QSS) when various point monitor signals (discussed later) were statistically stationary. Unless otherwise noted, all results presented in this paper are using QSS data, and quantities were only time-averaged across QSS data. Since the system experiences bulk pulsation, flow time is normalized by the time elapsed between pulses. This is referred to as a “pulse time” (PT) or, equivalently, as a “wave time” (WT). Waves and the general pulsing phenomenon are operating together in the same cyclic pattern. The mesh used for the majority of results, Ref-3, was run for 12 PTs of QSS data and includes 8.5 PTs of time-averaged data. A recently developed methodology was used to optimize the hardware utilization.[41]

4.2.2 Mesh and Boundary Conditions

A summary of the geometry, mesh, and boundary conditions is provided here. Rather than the typical twin-fluid atomizer design with a central liquid flow surrounded by a coaxial gas flow, the streams are reversed. An outer slurry annulus surrounds a central steam flow. The slurry pool is exposed to the hot subsonic center steam flow before the nozzle exit, and the nozzle orifice is extended to encourage significant steam-slurry interaction before exiting the nozzle. The full 360° domain is simulated by a 90° azimuthal slice bookended by periodic boundary conditions. Changing the angle from 45° to 90° produced no noticeable change in the axial droplet size profile,[19] and the sufficiency of the 90° azimuth will be further discussed among the results presented here. The downstream atomization domain spans 1.5 nozzle diameters in the radial direction and extends 2 nozzle diameters in the axial direction. Constant mass flow rates of 0.021 kg/s for steam and 0.79 kg/s for the slurry resulted in a gas-liquid mass ratio of 2.7%. Inlet temperatures for the slurry and steam were set to 304 K and 393 K, respectively. The steam inlet feed turbulence is set by defining a turbulent kinetic energy (k) and specific dissipation rate (ω), where k

= 48 m^2/s^2 and ω = 2.5×10^5 1/s. Both k and ω are spatially constant and were chosen arbitrarily. All results presented in this paper should be understood with these inlet conditions in mind, and other inlet conditions could be studied to determine the influence of GLR and turbulence feed conditions on wave formation and atomization.

Figure 4.1 provides an overview of the geometry and shows an example of the Ref-3-AMR mesh. The r, x, and θ represent the radial, axial, and azimuthal directions, respectively. In total, six distinct meshes were evaluated. A Base mesh was refined *n* times to produce Ref-1, Ref-2, and Ref-3 meshes. The total element count increases by a factor of nearly eight during refinement, as each cell length is cut in half. Note that the Base mesh was not refined farther back in the slurry annulus and steam pipe, but all regions of gas-liquid interaction were included in the refinements. The additional two meshes are Ref-2-45, which replaces the 90° azimuth with a 45° azimuth, and Ref-3-AMR, which utilizes adaptive mesh refinement (AMR). AMR provides the same refinement level as Ref-3 but increases computational efficiency by refining dynamically only around the gas-liquid interface while the rest of the domain remains at a Ref-2 refinement level. To closely track the gas-liquid interface, the mesh is refined every 5 time steps, and a stringent VOF gradient criterion is used. Ref-3-AMR maintained around 28 million elements compared to the 132 million elements in the Ref-3 mesh.

The Ref-3 mesh was found to be reasonably mesh independent across a range of metrics, including turbulent kinetic energy, velocity, and slurry volume fraction at the nozzle exit.[62] Furthermore, wave physics comparable to those produced by Ref-3 (pulsation frequency and wavelength, for example) were revealed by Ref-1, two refinement levels below Ref-3. We acknowledge that all relevant length scales are not resolved, but Ref-3 maintains the requirement of at least four cells across each droplet,[19] which was shown to be sufficient for viscous slurry atomization using our computational methods.[36] Strasser and Battaglia provide more discussion on implications of mesh resolution for atomization.[32] The trend of numerical results versus mesh size showed Ref-3-AMR to be an outlier. For these reasons, Ref-3 is used for all results presented in this paper unless otherwise noted. The difference in numerical output from the Ref-3 and Ref-3-AMR meshes is an important point; a comparison of the two meshes will be presented later. Figure 4.2 presents a side view of the pre-filming (wave formation) region of the Ref-3 mesh. The region where slurry meets steam will be referred to as the "wave pool" (this is where slurry waves rise into the steam flow) and the extension of the nozzle orifice as the "beach" over which waves travel before exiting the nozzle.

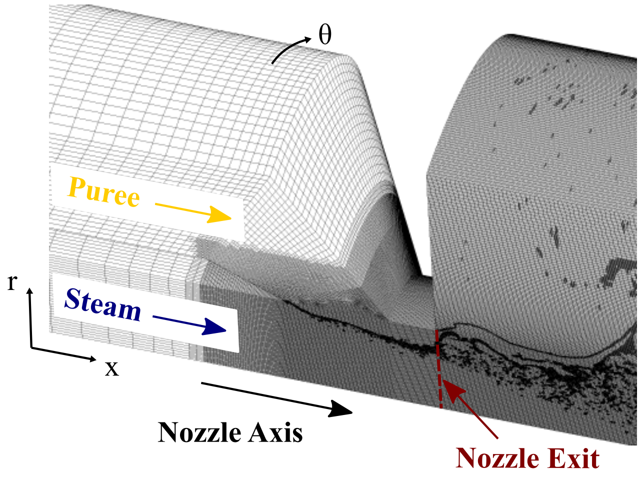

Figure 4.1 Oblique view of a representative Ref-3-AMR surface mesh, illustrating the nature of adaptive mesh refinement (AMR).

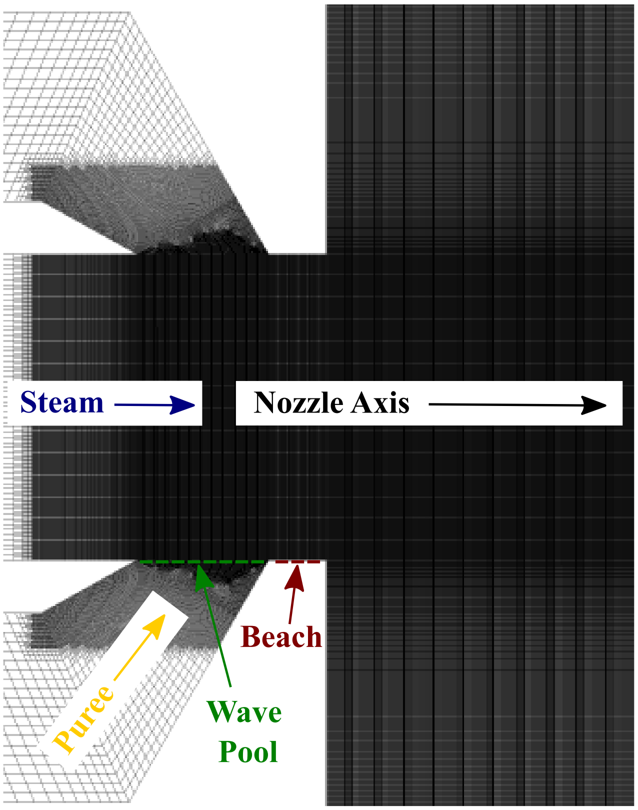

Figure 4.2 Side view of the 132 million element Ref-3 mesh for the pre-filming (wave formation) region of the atomizer.

4.3 Results and Discussion

4.3.1 3D Wave Cycle

The inverted-feed, forced interaction nozzle design leads to highly regular bulk pulsations in the system. These pulsations may be looked at from two perspectives: inside and outside the nozzle. We will examine both in this paper. Inside the nozzle, annular waves form at regular intervals (corresponding to bulk system pulsation), rising out of the wave pool (labeled in Figure 4.2). One wave forms at a time, where the wave “rises” radially toward the center of the steam flow and collapses while exiting the nozzle. Previous studies have mostly considered 2D aspects of these waves (KHI, which is integral to the wave formation process, is 2D),[62] leaving important 3D characteristics uninvestigated (RTI, for example, manifests in the azimuthal dimension). We seek to clarify how azimuthal variation develops in the wave and leads to atomization downstream.

Outside the nozzle, regular radial bursting of slurry is observed. This bursting manifests as a three-part sequence: 1) stretch, 2) bulge, and 3) burst. While a wave is forming inside the nozzle, an annular sheet of slurry stretches from the nozzle exit. As the wave collapses, the windward pressure build-up propagates through the wave, and the slurry sheet bulges radially. Finally, the slurry sheet ruptures altogether. Both wave cycling and radial bursting occur at a frequency around 1000 Hz (more on this later). The wave formation is a sinuous instability manifestation (from a Lagrangian perspective of an observer moving with the wave leaving the nozzle), but the bulk pulsation outside of the nozzle (radial bursting) is a varicose manifestation. Wave formation and collapse are integral to this "wave-augmented" atomization process by forcing the wave to crash into itself and enhance the disintegration of viscous, non-Newtonian fluids with radial explosions. The Weber ($We = \rho_l c^2 \lambda / \sigma$), Reynolds ($Re = \rho_l c \lambda / \mu_l$), and Strouhal ($St = f\lambda / V$) numbers characterizing the wave are 2.0×10^4, 1.2×10^4, and 0.08, respectively. Here, λ is wavelength, c is wave speed, f is wave frequency, V is the steam-slurry bulk velocity, ρ_l is slurry density, σ is surface tension, and μ_l is the lower end of slurry viscosity.

To better understand cross-wave variation during the 3D wave cycle, Figures 3-6 present a unique view of the annular wave: the 90° azimuthal slice has been unraveled to show a "flattened" (rather than annular) visualization of the slurry interfacial motion with a superimposed contour in the background. The result is more comparable to what ocean waves on a beach look like and provides insight into 3D aspects of the wave physics. Wave formation is illustrated in frames 1-3 and wave collapse in frames 4-6. Figure 4.3 shows the unraveled slurry surface colored by viscosity, and the background contour is colored by strain rate. This view is from the perspective of inside the nozzle to observe wave formation. High strain-rate regions appear as the hot steam contacts the slurry both at the wave and with droplets in the free stream. Viscosity reduces according to the shear-thinning nature of the slurry where strain rate is highest and the temperature-thinning effect by the hotter steam. Viscosity reduction causes ligaments to flick up into the steam, compounding the shear-thinning effect. Some azimuthal variation in viscosity is evident, although spatial variability fluctuates throughout the wave cycle. Azimuthal variation in the slurry is present, though minimal, in frames 1-3 but becomes very pronounced as the wave crashes in frames 4-6. Frames 4 and 5 show irregular valleys and ridges forming across the azimuth. The RTI time scale, as approximated with a low-Re method[68] for the low end of the slurry viscosity spectrum, is an order of magnitude lower than the wave time scale. This suggests that sufficient time is available for RTI development.

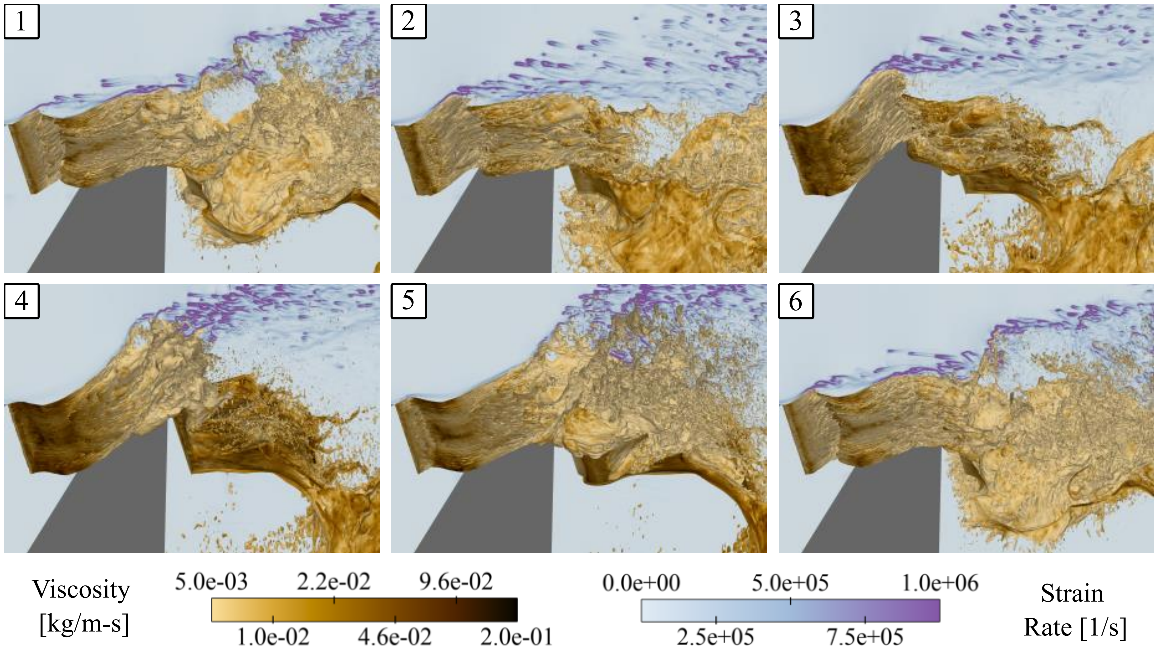

Figure 4.3 Sequential views of unraveled wave with the slurry surface colored by viscosity and contours of strain rate in the background.

Figure 4.4 presents a similar visualization as that in Figure 4.3 but viewed from outside the atomizer (looking underneath the wave). This perspective shows the annular slurry sheet (now flattened) stretching out from the nozzle as a wave rises. In this view, the wave is rising underneath the slurry sheet. The point of maximal extension before rupture (frame 4) corresponds to the highest viscosity of the slurry sheet, as it experiences minimal shear outside the nozzle radius. The sheet is destabilized by both azimuthal variation from RTI (heavier slurry being accelerated by the lighter steam) and azimuthal variation in viscosity. Frame 4 reveals significant and azimuthally variant bulging underneath the wave, which corresponds to valleys in the wave surface. Clearly, the wave is not impacting the slurry sheet uniformly. We also note that the multiple bulges across this 90° azimuthal slice indicates that 90° is a sufficient angle to capture variation in the azimuth. Parts of the wave contact local portions of the slurry sheet before others, contributing to “pre-rupture” of the slurry sheet. Frame 5 marks the pre-rupture of the slurry sheet, where small portions begin to break apart. The collapse of the wave and the instability of the slurry sheet both likely contribute to pre-rupturing. The further destabilized slurry sheet completely ruptures in frame 6 in a violent radial burst.

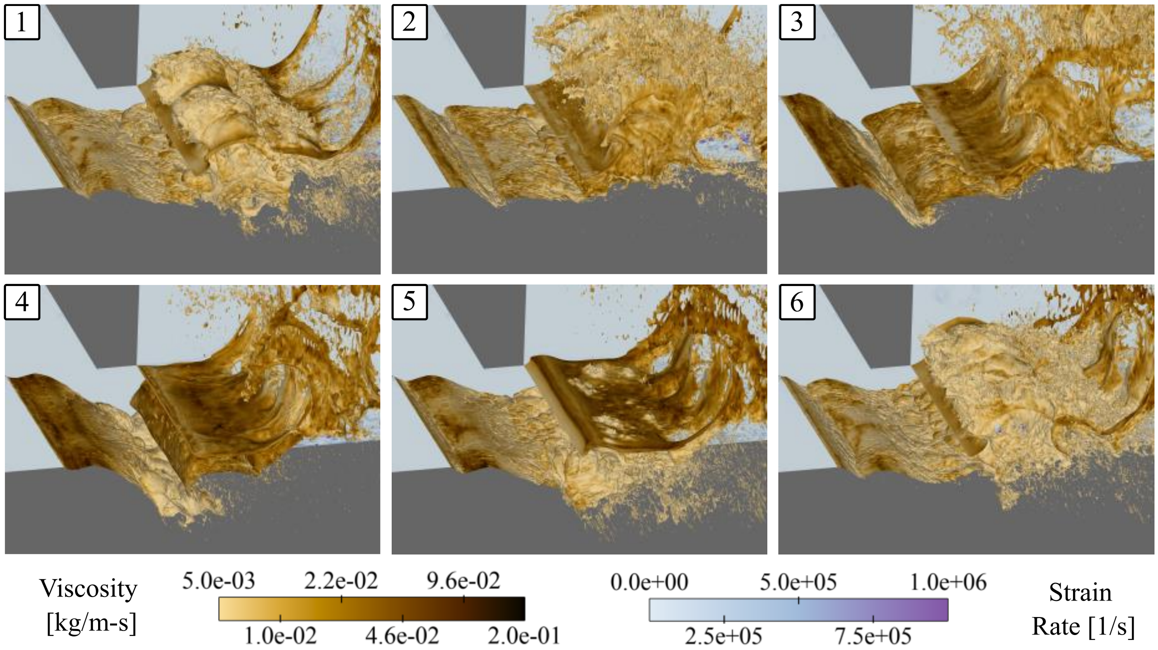

Figure 4.4 Sequential views of unraveled wave with the slurry surface colored by viscosity and contours of strain rate in the background.

Waves have a high blockage ratio that significantly affects the steam pressure and velocity via local acceleration; both fluctuate periodically with the pulsing cycles. Figure 4.5 illustrates these effects by showing the unraveled wave surface colored by pressure with a steam Mach number contour in the background. As the wave rises, it shelters its leeward side from the oncoming steam flow, thereby reducing the flow area for the steam exiting the nozzle. Steam is then accelerated to transonic velocities. Though not explicitly shown in Figure 4.5, small regions are supersonic. Consequently, steam compresses on the windward side of the wave to build up pressure, and the steam accelerates above the wave crest through the reduced-area opening. Both phenomena have implications for wave formation. The windward high-pressure zone exploits irregularities in the slurry surface caused by RTI and viscosity gradients. The transition from wave formation to wave collapse (frame 3 to frame 4) is significant: pressure increases sufficiently to overcome inertia and surface tension, and the increase in azimuthal variability is marked. We observe in frame 5 the propagation of the windward high-pressure zone axially as the wave collapses, which is a driving force in the radial bursting.

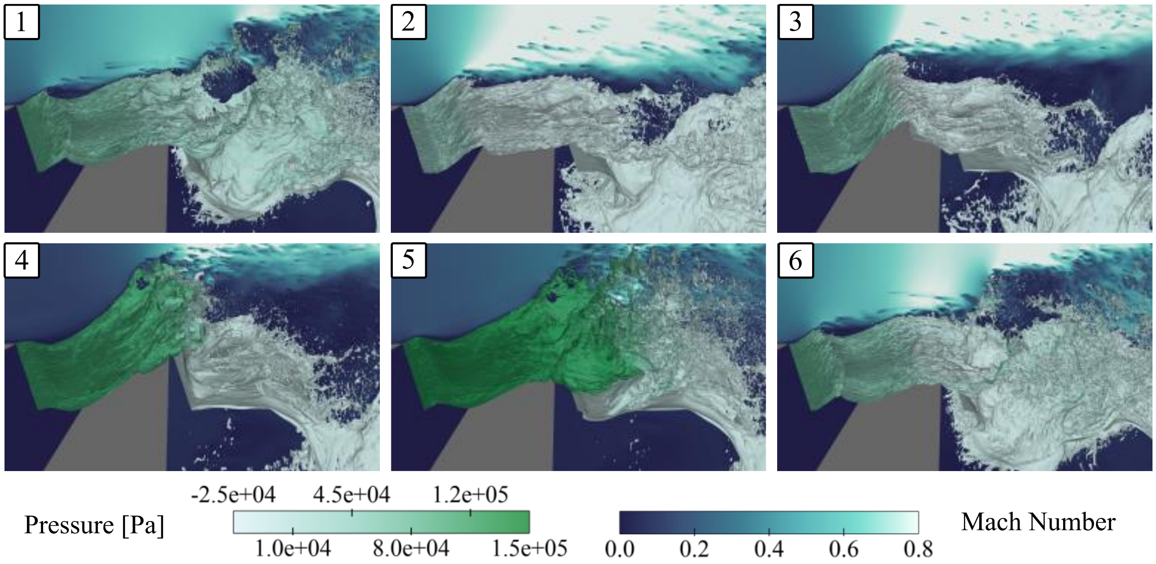

Figure 4.5 Sequential views of unraveled wave with the slurry surface colored by pressure with contours of Mach number in the background.

Figure 4.6 provides a side view to of the wave cycle (gray interface) with a contour of temperature in the background. Much like pressure, temperature cycles as the steam periodically compresses on the windward side of the wave. Highest steam temperatures occur in frames 4 and 5 and will contribute to surface destabilization and wave disintegration by reducing slurry viscosity, although shear is undoubtedly the dominant driving force behind viscosity changes. The wave appears to be largely 2D as it rises and approaches the nozzle exit. As it reaches the nozzle exit in frame 4, the wave is transitioning to a more 3D surface. This corresponds to the dramatic increase in azimuthal irregularity as pressure exacerbates existing surface variations and temperature thins the slurry.

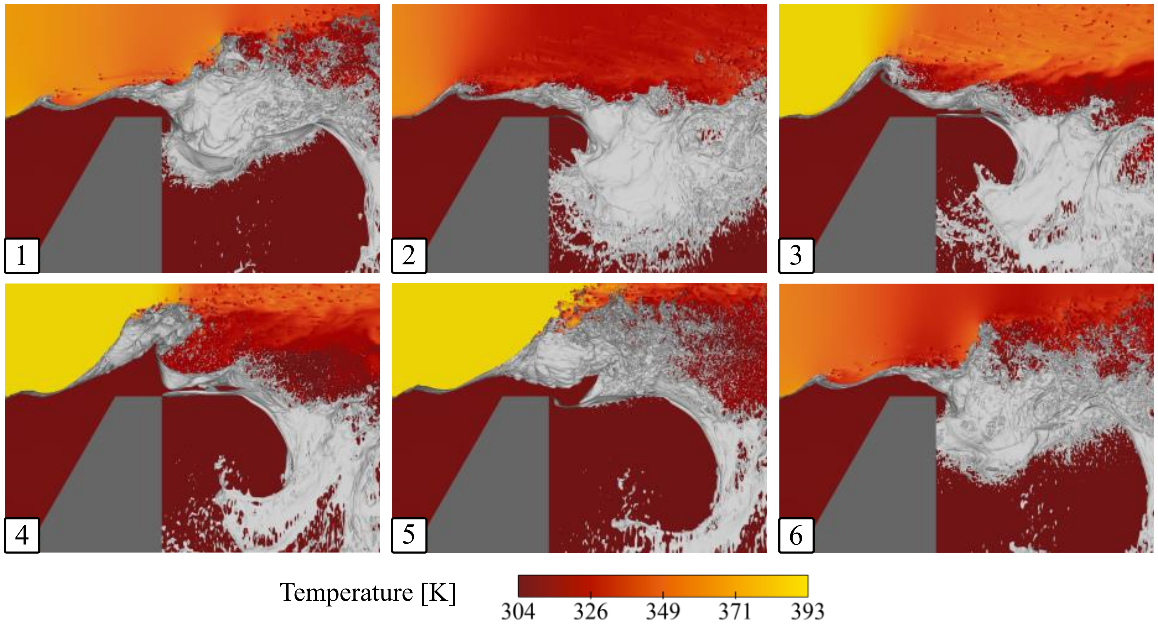

Figure 4.6 Sequential views of unraveled wave (gray) with contours of temperature in the background.

It has already been noted that RTI is driven by the baroclinic torque term $\left(\frac{1}{\rho^2}\frac{\partial \rho}{\partial x_i} \times \frac{\partial P}{\partial x_i}\right)$ in the vorticity equation. Density-based torque on the interface creates vorticity that will tend to increase the misalignment of pressure and density gradient vectors. This in turn creates additional vorticity, leading to further misalignment. Figure 4.7 presents contours of baroclinic torque. The highest values are on the order of 1×10^{13}

$1/s^2$, indicating significant misalignment of gradient vectors and strong RTI activity in the wave. Baroclinic torque is greatest at the steam-slurry interface, where density gradients are highest. Aside from directly at the interface, baroclinic torque is highest in the regions where droplets are being stripped off the wave and interacting with the steam. This indicates that as the shear layer forms, RTI becomes important very early in the wave life.

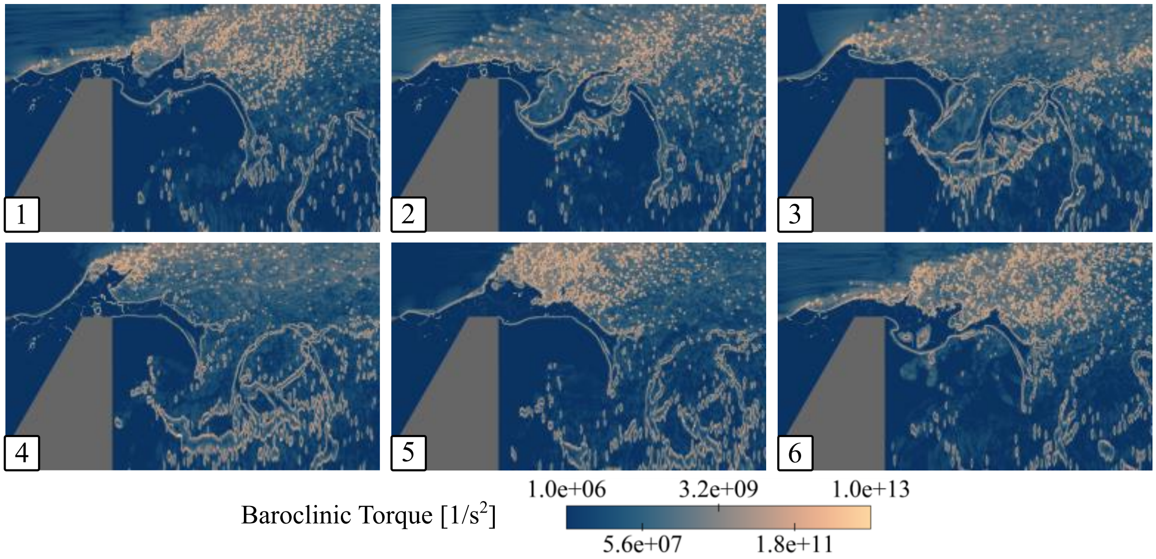

Figure 4.7 Sequential side contours of baroclinic torque through one representative wave cycle.

RTI and KHI are present early in the wave and lead to minute interfacial deformation. As the approaching steam navigates the newly roughened surface, spatial variations in temperature and strain rate occur across the wave. The shear- and temperature-dependent slurry responds accordingly, producing local variations in viscosity across the surface. Because of viscosity variation, the steam-slurry interface develops axial and azimuthal wavelength spatial variability. Also, due to viscosity variation, the interfacial stress develops spatial variation. Finally, the process is repeated as the surface deformation excites RTI and KHI. Figure 4.8 illustrates the cycle, where T is temperature, SR is strain rate, and WL is wavelength. Note that we are not utilizing linear instability analysis but rather the local momentum balance to reveal these instabilities.

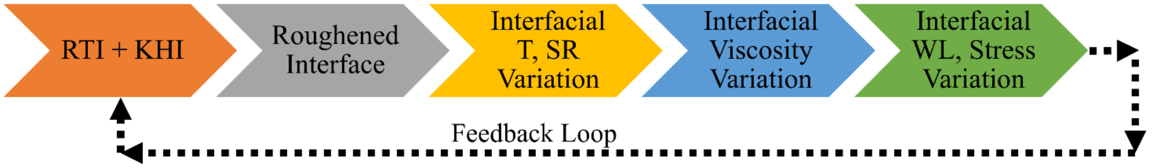

Figure 4.8 Instability cycle, where the Kelvin-Helmholtz instability (KHI) and Rayleigh-Taylor instability (RTI) cause surface variations that in turn excite the instabilities (T = temperature, SR = strain rate, WL = wave length).

4.3.2 Droplet Production

In a previous study, the effect of the wave on droplet production was largely addressed from the perspective of bursting *outside* the nozzle,[19] but questions remain regarding the role of 3D surface instabilities in droplet production *inside* the nozzle. It has been noted that small droplets break away from the wave inside the nozzle, and this was primarily attributed to steam shear (and later the collapse of the wave).[19] A more thorough investigation of this phenomenon is presented here, but we will first put the atomizer and its droplet production mechanisms in context.

The Wave-Augmented Varicose Explosions (WAVE) design is essentially a combination of a Gas-Centered Swirling Coaxial (GCSC) and Effervescent atomizer which capitalizes on the advantages of both and incorporates an additional element of radial momentum generation. Effervescence is introduced when the wave crashes onto the annular slurry sheet at regular intervals. Steam is sandwiched between the wave and sheet, introducing bubbles into the liquid phase. The Gas-Centered feature of GCSC is preserved, though swirl is not included in the current design. The lack of swirl necessity is a benefit of the current WAVE design because swirl increases internal geometric complexity and could require maintenance of fouled swirl elements. Besides, a previous study showed the impact of swirl in a multi-stream non-Newtonian atomizer to be minimal.[24] Future research may include revisiting this idea.

The “WAVE” title reminds of the fact that the atomization is augmented by wave generation due to at least three mechanisms. 1) The momentum of the crashing wave creates radial bulges in the liquid film, bursting droplets outward at regular intervals. 2) The high blockage ratio of the wave causes an intense pressure increase behind the wave that assists the wave momentum in driving liquid film rupture and slurry disintegration. 3) The extension of the slurry as a wave into the steam flow increases the interfacial area, providing more space for the steam to peel off droplets. “Varicose”[69] refers to the fact that, from a fixed external observatory frame, the atomization process takes on (to a large degree) an axisymmetric bulging pattern. Finally, “Explosion” refers to the radial blasting of droplets caused by wave crashing.

The first two mechanisms have been thoroughly investigated.[19] It is the third mechanism that will be explored here. Droplets clearly break away from the wave as it penetrates into the steam flow inside the nozzle (before the wave completely collapses), but what factors contribute to this outcome? It remains unclear whether the steam is merely stripping droplets off an axially moving wave surface or if slurry ligaments are being flicked up into the steam with significant radial velocity. To address this question, we present contours of radial velocity divided by the absolute value of axial velocity in Figure 4.9 and Figure 4.10. The outline of the steam-slurry interface is marked in black. Blue represents movement inward towards the central steam flow, and red represents movement outward toward the beach and beyond. For the purposes of this discussion (and from the perspective of Figure 4.9 and Figure 4.10), we will refer to blue regions as moving "upward" and red regions as moving "downward."

The time sequence in Figure 4.9 reveals the temporal development of radial versus axial velocity through a given wave cycle. By frame 3, the wave is penetrating significantly into the steam flow. Consequently, the wave develops a "hump" of dark blue on its back, corresponding to the deflection of steam upward. This deflection is significant close to the wave but less so further upstream. Just behind the wave jet, much of the slurry is directed axially (white), but the wave jet itself has significant radial thrust pushing upward into the steam flow. Radial velocity is at least 50% of the axial velocity in dark blue regions, which is the limit of the scale. By frame 4, where the wave height peaks, much of the wave base is moving in the axial direction. However, we still observe strong upward movement at the top of the wave, and some ligaments are present. In other words, we observe the slinging of ligaments upward as the main body of the wave is moving forward. Steam around the wave tip and ligaments also has strong upward motion. Non-axial flow in an atomizer has been found to correlate with higher droplet production efficiency.[32] As an aside, the beginning of the radial bulge is quite evident as the red patch just at the end of the beach in frame 4. The flicking up of ligaments in frame 4 helps explain what we term the "residual ligaments." For example, there is a nearly vertical ligament around the nozzle exit in frame

5, which is unexpected because of the high-velocity steam directed toward it. This appears to be a residual ligament derived from the windward ligament in frame 4. We call the windward ligament a “secondary” ligament, as it follows the primary wave tip. By frame 5, the ligament is moving downward, but it is an enduring form of the upward moving ligament in frame 4, and its position enables steam to disintegrate the slurry more effectively. Curiously, the steam on the leeward side of the residual ligament is moving upward, opposite the direction of the ligament and most of the surrounding slurry. This upward moving steam is likely helping strip away droplets via shear. By the time the wave has collapsed (frame 6), a clear divide is observed around the middle of the beach. To the left, slurry is moving upwards, and to the right, slurry is moving downwards. The primary exception to this trend is the downward moving slurry in the sheltered region on the leeward side of the newly formed wave.

Figure 4.10 shows contours at the moment in time roughly where the wave peaks in height (equivalent to frame 4 in Figure 4.9) at 6 azimuthal angles. The base of the wave is generally uniform across the various azimuthal slices, but the wave tips differ significantly across angles, even at 6° increments. What is consistent across angles is this: while the wave base is moving with a largely axial velocity, the wave tip has a significant radial velocity component. In frames 1 and 6 especially, we see a distinct secondary ligament form behind the wave tip, which also has a high radial velocity. Most frames include some level of a steam gap between the wave tip and a secondary ligament or wave base. The resulting wave tips can take on something of a “hammerhead” shape before breaking away (for example, frames 2, 4, and 6) as the slurry connecting the tip to the base is thinned. We direct the reader to notice particularly the penetration of steam into the wave as the tip rises. In frames 2-4, the steam is pushing down into the wave, creating significant necking to break off the tip. Frame 5 shows smaller pockets of steam inside the wave, where steam fingers have forced through the deformed surface. The upward movement of the wave, then, provides an effervescence mechanism in addition to the trapping of steam as the wave crashes.

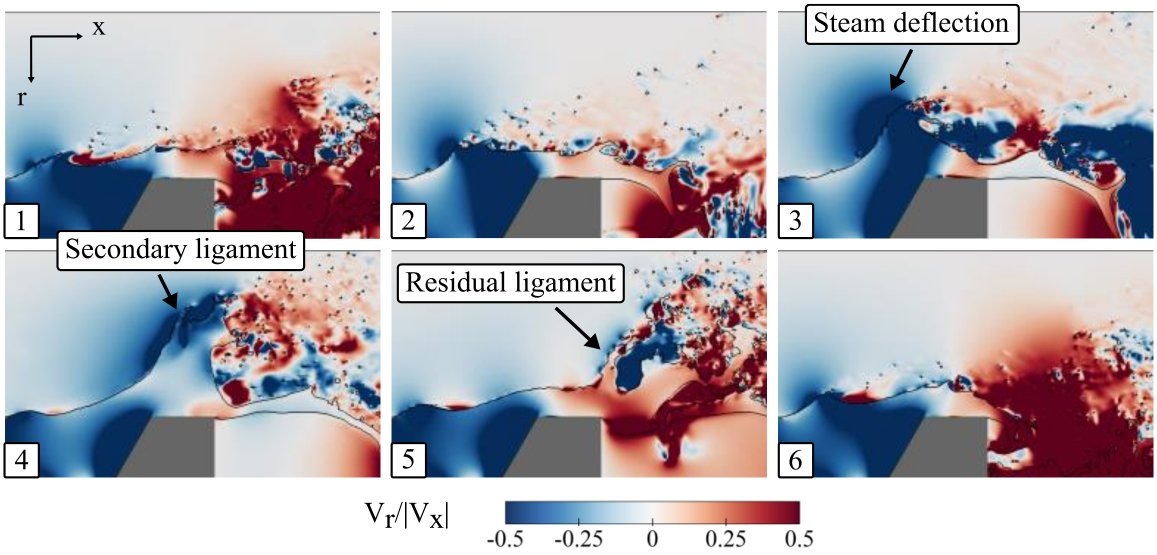

Figure 4.9 The ratio of radial velocity to the absolute value of axial velocity through one representative wave cycle.

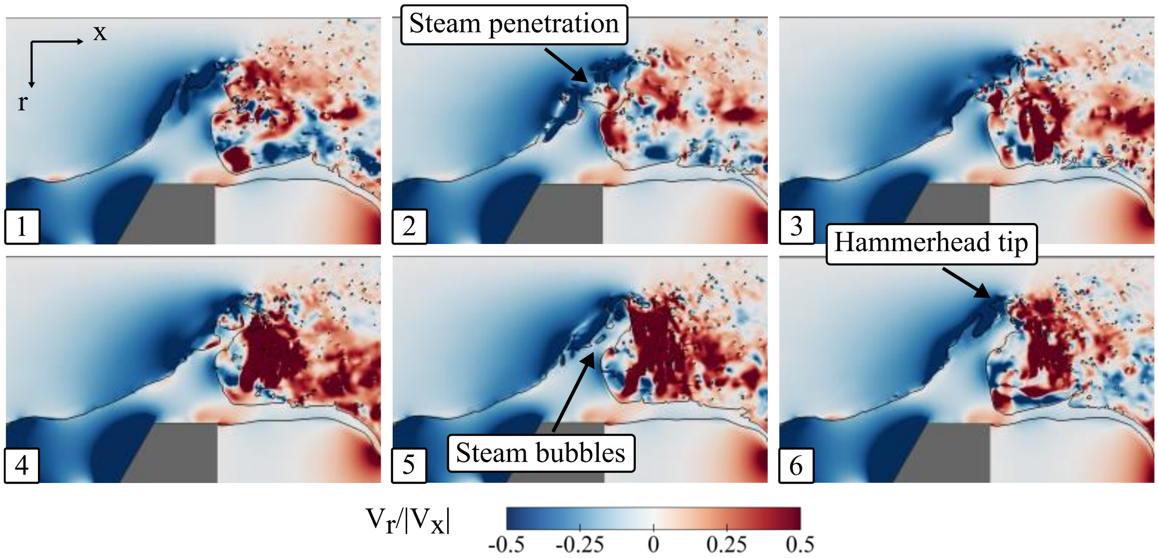

Figure 4.10 The ratio of radial velocity to the absolute value of axial velocity at a fixed time, roughly where the wave peaks (equivalent to frame 4 in Figure 4.9).

It is clear that flicking is an important mechanism for droplet production in the nozzle, but is stripping also important? While flicking involves ligaments rising perpendicular to the steam flow, by stripping, we mean droplets breaking away from the slurry surface or a ligament stretching in the direction of steam flow (parallel). A close look at Figure 4.9 seems to show stripping towards the beginning of wave growth, but this is made clearer in the animation for Figure 4.10. This animation shows stripping early on where droplets break free from *both* the surface and parallel ligaments. As the wave matures, the primary droplet production mechanism transitions to flicking. Finally, outside the nozzle, effervescence and the collapse of the wave lead to its complete disintegration. In summary, droplet production inside the nozzle is dominated by stripping in the early wave and later by flicking as the wave crests.

To conclude our discussion, we note several consequences (and benefits) of slurry ligaments flicking radially up into the gas stream. Effervescence is introduced via a second mechanism before the wave crashes and sandwiches steam. While the slurry wave jet is accelerated by the steam and thinned by shear, causing the jet to buckle upwards and sling the liquid tips[40] up into the gas stream as ligaments, the gas infiltrates the liquid as bubbles. The thin fingers from the liquid sheet make it easier for the steam to peel off droplets,[70] and this avoids the need for a forcibly thinned sheet using a thin slurry annulus with high pressure drop and risk of plugging. Additionally, the shearing and thinning of the fingers lowers the timescale for RTI to take effect, making RTI more active and sooner.

4.3.3 Point Monitors

4.3.3.1 Overview

In a previous study, only two quantities were tracked at a single point monitor.[62] We greatly expand point monitor analysis here to include 100 signals for the purpose of understanding the spatial and temporal variation of quantities, both azimuthally and along the slurry flow path. Velocity magnitude, slurry volume fraction (VF), strain rate, and turbulent kinetic energy (TKE) were tracked at five point monitors placed roughly along the trajectory of the slurry interface as it interacts with the steam. Each point monitor is present at five different azimuthal angles (4.5°, 13.5°, 22.5°, 31.5°, and 40.5°), spaced evenly within a 45° azimuth, which is half of the total 90° azimuth. In total then, 100 individual signals were recorded (4 quantities across 25 points) for the entirety of the QSS window. Due to the extensive nature of this temporal data collection, we provide only select plots and summary statistics. The locations of the five point monitors in a given azimuthal slice are shown in Figure 4.11. The labels of Inner, Middle, Exit, Tip, and Outer, will continue to be used in reference to these points, along with their azimuthal angles. The

Inner, Middle, Exit, Tip, and Outer points are located 1, 0.75, 0.67, 1.25, and 1.5 nozzle radii from the nozzle axis (bottom edge of Figure 4.11), respectively. The Inner point is centered axially on the wave pool. The Middle and Exit points are positioned axially at the start and end of the beach. The Tip and Outer points are located 0.25 and 1.25 nozzle radii downstream of the nozzle exit, respectively. The output data monitored at these five points will be discussed throughout the remainder of the paper, revealing the spatiotemporal characteristics of the system.

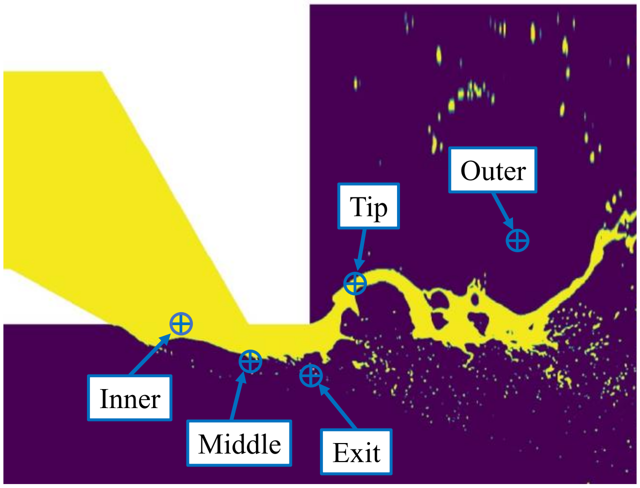

Figure 4.11 Locations of five points monitors (roughly along the slurry interface trajectory) where certain data quantities are collected.

Comparing the Exit point monitors across azimuthal angles reveals aspects of the wave interface as it exits the nozzle. Figure 4.12 shows a moving average time series for (a) velocity and (b) slurry volume fraction through 12.5 pulsing cycles. Velocity signals are fairly uniform across angles and from wave to wave. In other words, the general *motion* of the wave seems to vary minimally as it exits the nozzle, both azimuthally and temporally. However, slurry volume varies significantly in the azimuthal and temporal dimensions. We attribute this variability largely to the work of RTI, which is exacerbated by windward pressure buildup. We note again that it is around the nozzle exit that the wave collapses, marking a transition from a somewhat 2D wave to a more azimuthally diverse 3D wave. Table 4.1 provides the mean and coefficient of variation (COV) for each signal in Figure 4.12 as well as the other quantities that are not displayed graphically. Note that this is a small subset of all point monitor data. The COV is a normalized standard deviation, where the standard deviation is divided by the mean and converted to a percentage.

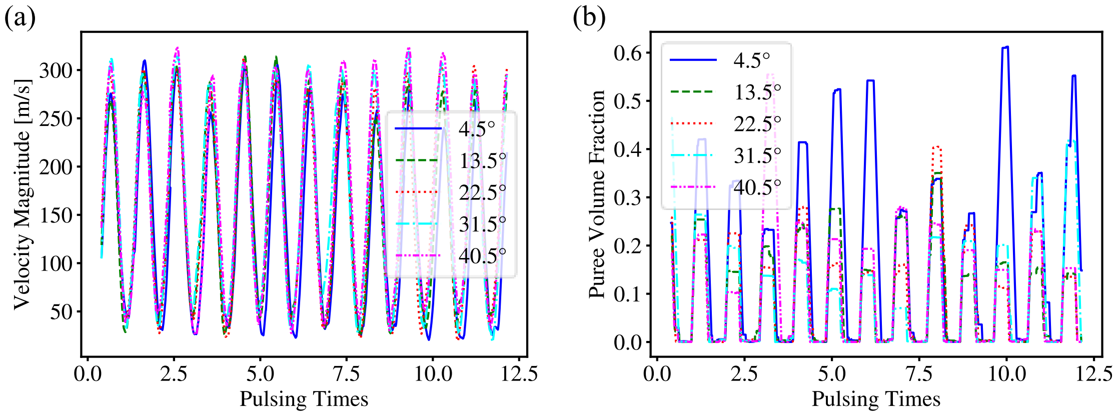

Figure 4.12 Moving average time series of (a) velocity and (b) slurry volume fraction at the Exit point monitors across all five azimuthal angles.

Table 4.1 Mean and coefficient of variation (COV) for signals across all five azimuthal angles at the Exit point.

	Velocity [m/s]		Slurry VF		Strain Rate [1/s]		TKE [m^2/s^2]	
Angle	Mean	COV	Mean	COV	Mean	COV	Mean	COV
4.5	142	94	0.17	219	4.5×10^5	156	412	142
13.5	157	83	0.09	312	4.5×10^5	141	414	129
22.5	161	83	0.09	311	3.6×10^5	152	345	131
31.5	167	82	0.10	301	3.0×10^5	170	325	144
40.5	171	79	0.10	299	2.9×10^5	166	312	148

On the other hand, we can reveal the axial (roughly) development of quantities by examining all five point monitors at a given azimuthal angle. Figure 4.13 shows the moving average time series for (a) velocity and (b) strain rate for all point monitors at the 22.5° azimuthal angle. Velocity magnitudes increase significantly as the wave moves from the pool to the nozzle exit but decreases at the Tip and Outer point monitors. The slurry is disintegrating at these last two points, so the monitors are picking up both slurry droplets and relatively stagnant steam. Periodicity is much more evident inside the nozzle than outside the nozzle. This is indicative of the relatively uniform wave motion inside the nozzle and the chaotic rupture outside the nozzle. Strain rate follows a similar pattern through the slurry motion, increasing to the nozzle exit and then decreasing outside the nozzle. However, the difference between the Middle/Exit points and the Tip/Outer points is less marked than velocity. Compared to velocity, the temporal periodicity of strain rate is less pronounced for the middle Middle/Exit points and more pronounced for the Tip/Outer points. In other words, velocity gradients are fluctuating more consistently than velocity magnitude outside the nozzle. Strain rate also shows more wave-to-wave variation than velocity within the nozzle. Table 4.2 provides the mean and COV for each signal in Figure 4.13 as well as the other quantities that are not displayed graphically.

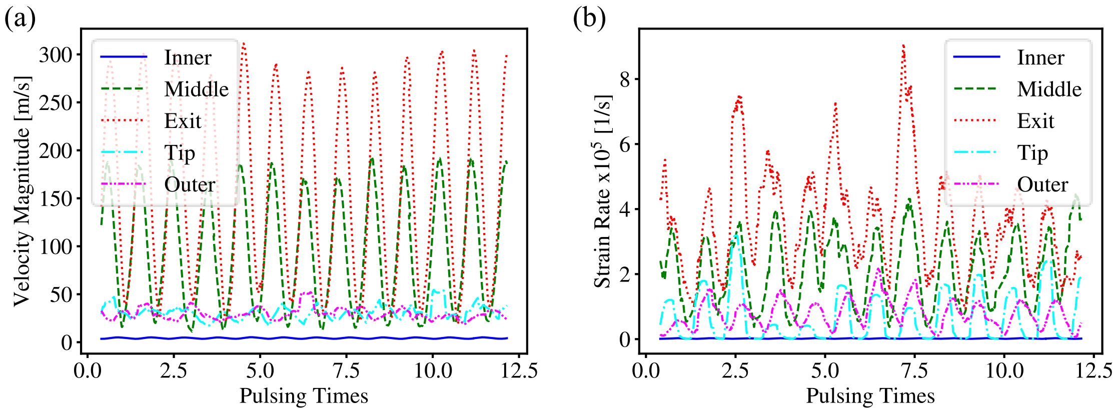

Figure 4.13 Moving average time series of (a) velocity and (b) strain rate at all five point monitors at the 22.5° angle.

Table 4.2 Mean and coefficient of variation (COV) for signals across all point monitors at the 22.5° azimuthal angle.

	Velocity [m/s]		Slurry VF		Strain Rate [1/s]		TKE [m^2/s^2]	
Point	Mean	COV	Mean	COV	Mean	COV	Mean	COV
Inner	4.2	18	1.0	0.0	1.9×10^3	54	1.1	60
Middle	98	86	0.241	176	2.2×10^5	136	255	147
Exit	161	83	0.090	311	3.6×10^5	152	345	131
Tip	31	67	0.064	367	6.8×10^4	257	28	326
Outer	30	46	0.026	550	7.7×10^4	137	14	320

4.3.3.2 Frequency Analysis

FFTs were performed to determine the dominate frequencies in the atomizer at various locations. Because of the pulsing nature of the system, we expect most quantities to cycle at a consistent overall pulsing frequency (frequency of wave formation). Velocity magnitude, strain rate, slurry volume fraction, and turbulent kinetic energy were tracked at all 25 point monitor locations. FFTs reveal frequencies around 1000 Hz for the vast majority of these quantities and point monitors. 83% of signals show a 1068 Hz peak frequency (note that slurry volume does not fluctuate at any Inner point locations). 8%

show a 2060 Hz peak frequency, and one shows 3128 Hz, illustrating the higher mode harmonics. Strain rate is the most consistent quantity: all 25 point monitors show a dominate frequency of 1068 Hz. The most prominent frequencies across point monitors for the Ref-1 and Ref-2 meshes are 963 Hz and 992 Hz, respectively. Frequencies vary wildly for the Base mesh, and no prominent frequency is evident. This corresponds to previous findings: major wave characteristics are present, and consistent, with progressively increased mesh resolution, beginning with the resolution of Ref-1.[62] The characteristic pulsing of the system is largely absent from the Base case, and the Ref-3 mesh is two refinement levels above Ref-1.

To understand how FFT peak frequencies vary across the azimuth, the COV was computed, which shows azimuthal point-to-point variation as a percentage. For a given point location, such as Inner, a single peak frequency was computed at each azimuthal angle, and the COV was computed from these 5 frequencies. Figure 4.14 shows the azimuthal frequency COV from the Inner to the Outer points (effectively along the interfacial trajectory). Most frequencies are consistent inside the nozzle, but the variation increases significantly outside the nozzle. The only quantity that continues to fluctuate uniformly in the azimuth outside the nozzle is strain rate. Figure 4.14 illustrates again the consistency of strain rate as a pulsating quantity.

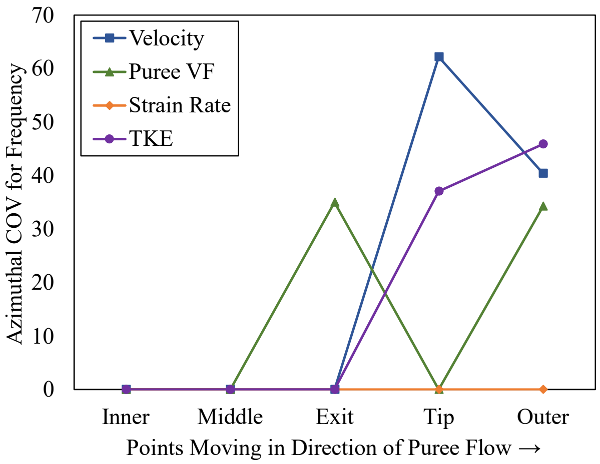

Figure 4.14 Azimuthal coefficient of variation (COV) for frequency at various points along the slurry interface flow path.

FFTs are meaningless unless the resulting peak frequencies have converged over the course of the simulation. For those signals that showed a peak frequency of 1068 Hz (the prominent frequency among all signals evaluated), the FFTs generally converged within 4 pulsing cycles after the flow was already at QSS. This was not necessarily the case for less periodic signals like velocity at the Tip and Outer points (see Figure 4.13).

Figure 4.15 provides a sample FFT peak frequency convergence plot for strain rate at the Exit point in the 22.5° plane (see Figure 4.13 for time series). The vertical dashed line is the 4 pulsing cycles mark, and the green star is the final value. Zero-padding was employed, resulting in the discrete step values towards convergence.

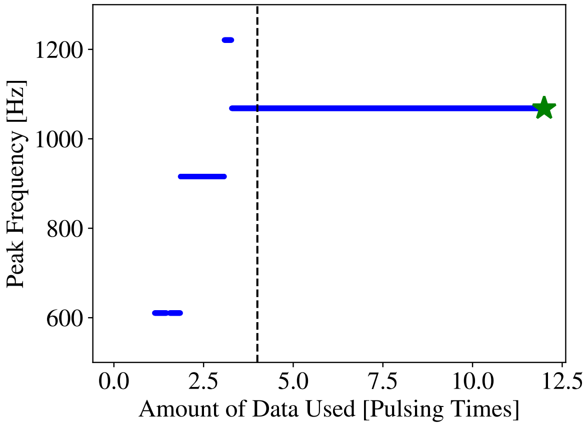

Figure 4.15 Convergence of FFT peak frequency for the strain rate signal at the Exit point monitor in the 22.5° plane.

Figure 4.16 presents two FFT examples, one for velocity at the Inner point (left) and one for strain rate at the Exit point (right). Both are at a 22.5° azimuthal angle, and the time series were shown in Figure 4.13. The Inner point is located at the surface of the wave pool, where waves are being produced. The wave pool surface, then, has a fluctuating velocity at 1068 Hz, which sets the pace for bulk pulsation in the system. Geometric parameters might be varied to determine their influence on pulsing frequency, but that is beyond the scope of this study. The Inner velocity FFT also shows harmonics at roughly 2060 Hz and 3110 Hz, which correspond to the peak frequencies for a minority of signals. The Exit strain rate FFT shows the same peak frequency as the Inner velocity, although it is less pronounced, and no harmonics are evident.

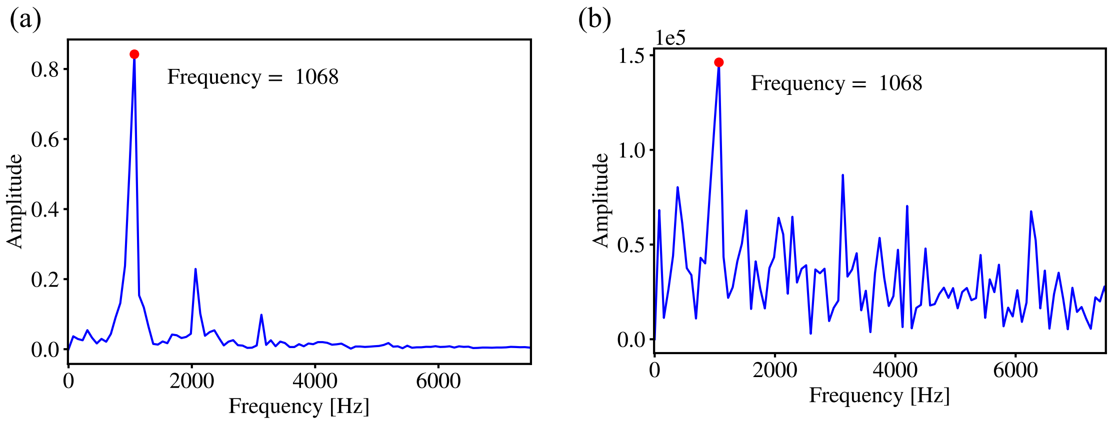

Figure 4.16 FFTs with peak frequency labeled for (a) velocity at the Inner point and (b) strain rate at the Exit point.

As shown, the preponderance of frequencies are close to, or multiples of, approximately 1000 Hz, which results from the wave pool generation process (i.e. KHI working with Bernoulli to amplify surface disturbances). Therefore, the wave-generation process sets up an absolute instability in the system that is likely to be unaffected by upstream turbulence effects. A future study could include evaluations of this.

4.3.3.3 Cross-Correlations

The spread of information in the azimuthal and radial directions can be assessed by determining the cross-correlation between signals; a normalized cross-correlation of 1 indicates that two time-series signals are perfectly correlated and implies 2D (axisymmetric) motion. The time difference between two given locations was accounted for by time-shifting the signals to align them before calculating the normalized cross-correlation. Cross-correlations (calculated using the NumPy package in Python) were normalized by subtracting the means from the signals and dividing the cross-correlation by the number of data points and the standard deviations of the two signals. Figure 4.17 shows the normalized cross-correlation between velocity signals both azimuthally and along the slurry interface trajectory. Correlation is calculated between the velocity signal at a given azimuthal angle or point and the first angle or point. In essence, we are estimating how much the motion at one place in the flow field might be related to the motion at another place in the flow field.

The motion at the inner point monitor appears to be uniform across all angles (indicating its 2D nature), as the signals show almost perfect correlation with the first angle (4.5°). The Middle and Exit points show relatively high correlation, and the correlation remains largely the same across angles. Outside of the nozzle, where the wave and slurry sheet are being ruptured, the tip and outer point monitors show low correlation between angles. The Tip point monitor, which is closer to the nozzle (around the bulging and bursting), shows slightly higher correlation. These results suggest that fluid motion *inside the nozzle* is generally azimuthally similar (2D), but the fluid motion *outside the nozzle* as the slurry bursts is azimuthally unrelated (3D). Furthermore, since the correlation, for a given point monitor, is quite consistent across 45°, we conclude that a 90° mesh is more than sufficient to capture azimuthal variation. The Inner point, which is at the surface of the wave pool, marks the location of wave generation. The Middle and Exit points are well-correlated with the Inner point, but the Tip and Outer points are not. In other words, the velocities at Tip and Outer do not show much relation to wave pool motion.

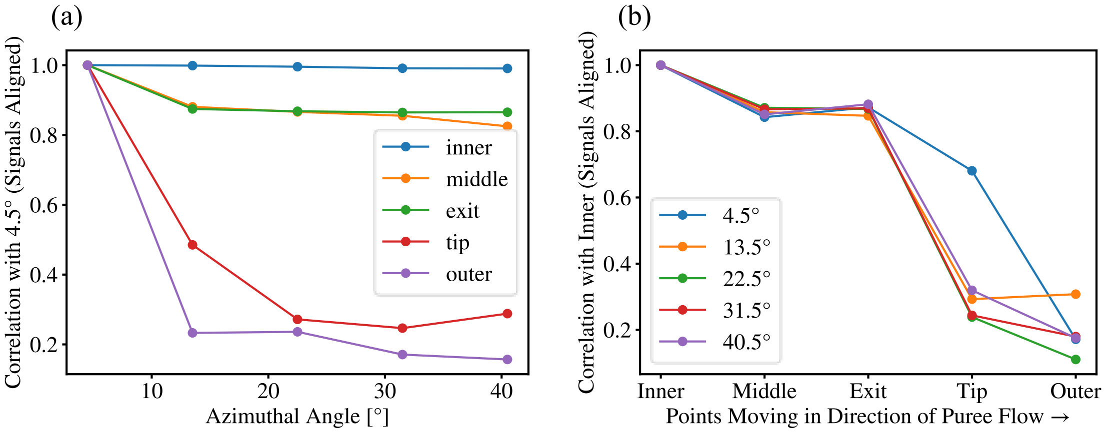

Figure 4.17 Normalized cross-correlation between transient velocity magnitude signals from point monitors at five points along the slurry interfacial flow and five azimuthal angles.

When signals are reasonably correlated, a time lag shows how much the motions are temporally offset. The time lag is calculated as the amount the signals must be time-shifted to produce the maximum cross-correlation. In Figure 4.18, time lags are normalized by the pulsing time, so a given value represents the fraction of a pulse cycle by which the signals are offset. Time lag is meaningless if the signals are not well-correlated, so the Tip and Outer points have been removed from the time lag plot. Figure 4.18 displays the extent to which the Middle and Exit velocity signals lag the Inner velocity signal. These results are communicating where the Middle and Exit points are, temporally, within the wave cycle (which repeats regularly every 1 PT). Velocity fluctuations at the wave pool (Inner point) reach the Middle and Exit points 0.7 and 0.8 PTs, respectively, after the initial wave pool motion. Fluid motion at the nozzle exit then lags the Middle point by 0.1 PT. Velocity spikes again in the wave pool 0.2 PTs after a velocity increase at the Exit point. This cycle is illustrated in Figure 4.18, which shows the percentage of a pulse cycle for velocity fluctuations at Inner (I) to reach Middle (M) and then Exit (E) and then start again at Inner. The majority of a given pulse cycle (70%) involves the wave growing out of the wave pool and reaching the beach. After reaching the beach, the wave travels more rapidly to the nozzle exit and beyond.

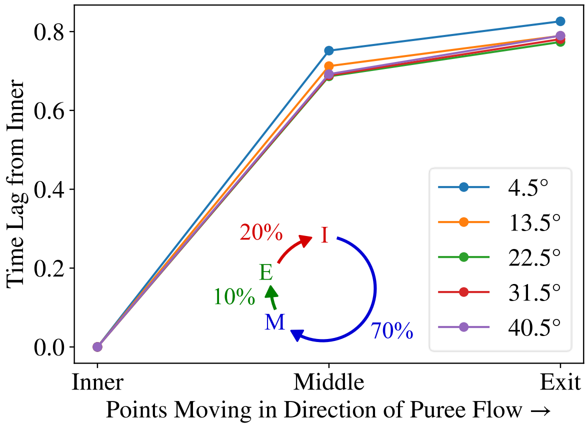

Figure 4.18 Transient velocity signal time lags from the Inner point at five azimuthal angles.

In addition to inter-point correlations for velocity, correlations between different quantities were calculated at all 25 points. Three contour plots in Figure 4.19 summarize these data and show the normalized cross-correlation between 1) velocity magnitude and slurry VF (far left), 2) TKE and strain rate (middle), and 3) velocity magnitude and strain rate (far right). The slurry volume fraction maintains a value of 1 at the Inner points, making any normalized cross-correlation value meaningless. For this reason, the inner points were excluded on the leftmost plot in Figure 4.19. The trend across all 3 sets of correlations is that any two quantities are most highly correlated at the Inner point, and correlation decreases downstream. Correlation between quantities is also fairly azimuthally uniform, particularly inside the nozzle. Velocity and slurry VF are the least well-correlated overall.

The middle plot indicates that, after the Exit point, TKE and strain rate are decoupled; thus, TKE downstream must have been produced by some earlier shear. In summary, we observe the decoupling of quantities exiting the nozzle: strong correlations inside the nozzle and very weak correlations outside the nozzle.

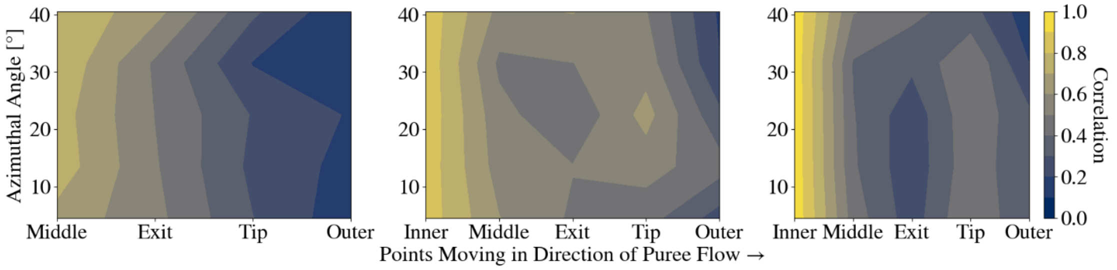

Figure 4.19 Contours across all 25 points for the normalized cross-correlations between 1) velocity magnitude and slurry volume fraction (left), 2) turbulent kinetic energy strain rate (middle), and 3) velocity magnitude and strain rate (right).

4.3.4 Adaptive Mesh Refinement

Up to this point, the Ref-3 mesh has been used entirely for visualization and analysis. It has been noted that Ref-3-AMR, though a more cost-efficient alternative, is the *outlier* to the numerical trends of two point monitor signals,[62] but no visual comparison was provided, and a more rigorous comparison is lacking. A qualitative and quantitative comparison of Ref-3 and Ref-3-AMR is here provided to clarify the differences between the two models. We emphasize again that Ref-3 and Ref-3-AMR have the exact same mesh resolution at the slurry-steam interface. A rigorous VOF gradient criterion and adaption frequency were used, but it should be noted that there are other criteria that can determine the regions of adaption for AMR. It is possible that a different criterion would positively affect AMR results, though we find this doubtful based on the *extensive* AMR refinement in this study. We also acknowledge that any conclusions about AMR as a technique are limited to ANSYS Fluent and its underlying algorithms. All validation efforts were conducted using meshes equivalent to Ref-3 (mostly hexahedral elements swept in the flow direction), and AMR has not been validated experimentally for this work. The differences between Ref-3 and Ref-3 AMR indicate problems with the communication of information through split cells, which are constantly created by AMR.

Figure 4.20, which shows the slurry surface (coloured by slurry viscosity) as it exits the nozzle (flow is generally downward), reveals qualitative differences. The leftmost set of images in Figure 4.20 show that Ref-3-AMR produces a significantly more rippled surface, and slurry viscosity is generally higher. A higher viscosity indicates lower strain rate, perhaps suggesting that the mesh gradients around the slurry-steam interface are affecting velocity gradients. We remind the reader that RTI and viscosity gradients serve to destabilize the annular slurry sheet, priming it for rupture and atomization as the wave crashes into it. The middle and rightmost images in Figure 4.20 reveal Ref-3 rupturing more readily than Ref-3-AMR. In the middle images, little pre-rupture (localized bursting events) in the annular slurry sheet is observed for Ref-3-AMR. Much more can be seen for Ref-3 (corresponding to the preliminary rupture for Ref-3 in frame 5 of Figure 4.4). In the rightmost images, the radial burst of slurry is more violent for Ref-3 than Ref-3-AMR, and Ref-3 is clearly producing smaller droplets at this stage of the pulsing sequence. Interestingly, Ref-3-AMR was found to have slightly larger droplets throughout the domain past the nozzle exit.[19]

Quantitative discrepancies between Ref-3 and Ref-3-AMR are summarized in Figure 4.21, which shows percent differences between azimuthally-averaged quantities.

TKE shows by far the greatest difference between the models, especially outside the nozzle, where a 160% difference is observed. In general, the difference between model outputs is higher outside (shown in Figure 4.20) than inside the nozzle. This follows the trend of an increasing presence of mesh element size gradients as the slurry disintegrates outside the nozzle. Interestingly, the % difference for strain rate (velocity gradients) increases outside the nozzle, but that for velocity does not. This observation indicates that *gradients* are more strongly affected by AMR. We note also that TKE production is driven by velocity gradients. Our conclusion: the AMR technique within ANSYS Fluent 2020R1 is not sufficient to accurately model non-Newtonian wave-augmented atomization in the present system.

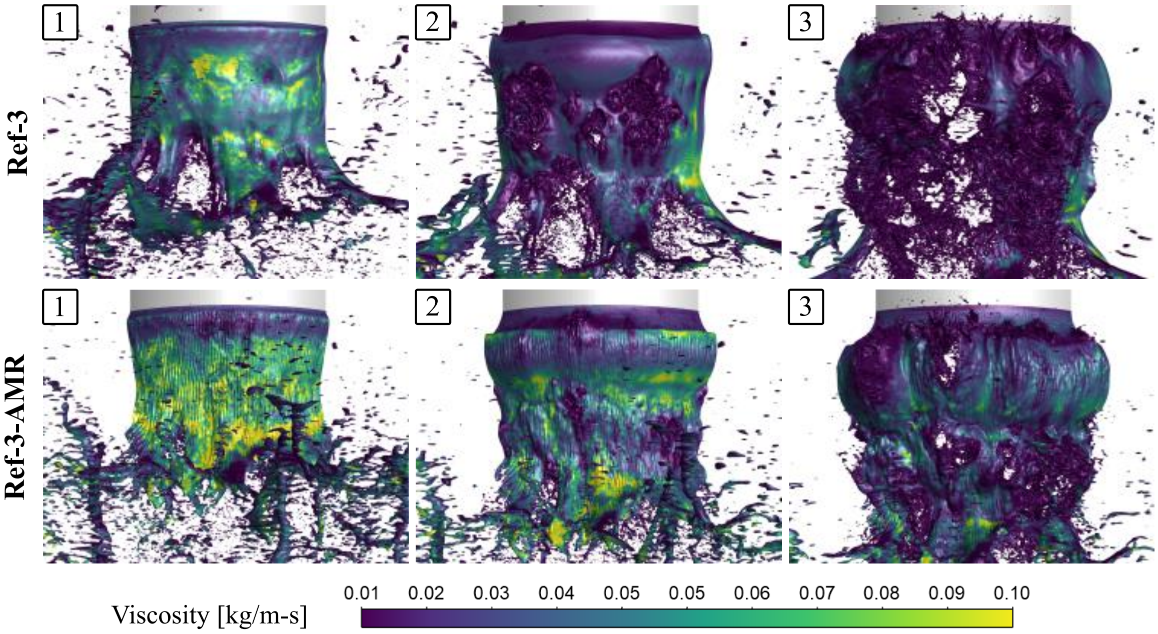

Figure 4.20 Comparison of slurry surface as computed by the Ref-3 (top row) and Ref-3-AMR (bottom row) meshes at three points in the wave cycle.

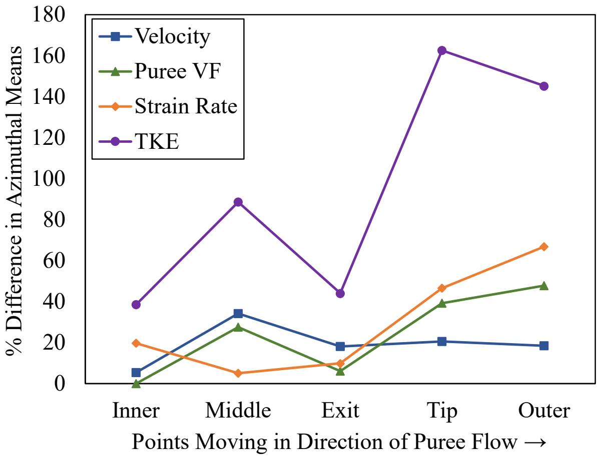

Figure 4.21 The percent difference between azimuthally-averaged quantities at various points along the slurry interface flow path for Ref-3 and Ref-3-AMR.

4.4 Conclusion

Using a computational framework which has been validated and used extensively over the course of the last decade, we have analyzed the spatiotemporal characteristics of the novel WAVE process (Wave-Augmented Varicose Explosions) in which non-Newtonian waves facilitate disintegration in an inverted feed twin-fluid atomizer. Annular slurry waves "rise" into a central hot steam flow, creating a secondary nozzle effect for the steam, as an annular slurry sheet stretches from the nozzle. Waves then collapse as they exit the nozzle, crashing into the slurry sheet in a violent radial burst to enhance droplet formation. The wave birth-death cycle is part of a general bulk system pulsation phenomenon, causing many quantities to fluctuate periodically. Important knowledge gaps from previous studies have been filled to provide a more complete understanding of this efficient atomization phenomenon. A summary of new contributions to the literature is provided in the following paragraphs.

We began by presenting a unique visual perspective: unraveled wave views to elucidate characteristics of the 3D wave cycle. An estimate of RTI time scale showed sufficient time for RTI development, and baroclinic torque on the order of 1×10^{13} 1/s^2 indicates strong RTI activity in the wave. KHI and RTI cause surface variations in the non-Newtonian slurry that then excite the instabilities in a self-amplification cycle. During the early stages of wave growth, stripping is a dominant mechanism for droplet production. Later, as the wave crests, ligaments flicking up into the steam flow at the wave tip facilitate droplet production inside the nozzle. Meanwhile, the radial thrust of the wave allows for steam penetration to increase effervescence and sometimes break off the wave tip. Further disintegration is encouraged as the wave leaves residual ligaments in its wake.

An evaluation of velocity, slurry volume fraction, strain rate, and turbulent kinetic energy at 25 axially and azimuthally spaced points revealed a loss of consistent fluctuation frequency outside of the nozzle. Strain rate, however, cycles with the dominant system frequency at all points. FFT analysis was an important component of this study, and peak frequencies generally converged within 4 pulsing cycles. The nozzle exit marks a significant increase in azimuthal variation of velocities. Velocities show strong azimuthal correlation (2D) in the wave formation region inside the nozzle but are azimuthally unrelated (3D) outside the nozzle, where radial bursting is occurring. Outside the nozzle, fluid motion did not show strong correlation with wave pool motion. Correlations between quantities, though strong in the wave formation region, showed a consistent trend of significant decoupling outside the nozzle. Time lags revealed that, for a given pulse cycle, the wave rising out of the pool to reach the beach takes 70% of the total pulse time.

Azimuthal correlations of velocity demonstrate that a 90° angle is sufficient to capture azimuthal variability, which is important for atomization. Evaluation of Ref-3-AMR, both qualitatively and quantitatively, showed that this particular AMR technique is insufficient for accurately modeling non-Newtonian, wave-augmented atomization in the present system, despite the allure of computational savings. Velocity gradients were more affected by AMR than velocity magnitude. Turbulent kinetic energy differed most drastically between Ref-3 and Ref-3-AMR, particularly outside the nozzle. Future research could evaluate how geometry changes affect the spatiotemporal characteristics of the atomization process, such as pulsing frequency.

CHAPTER FIVE

‘SMART’ TRANSONIC VISCOUS LIQUID SHEET HEATING AND DISINTEGRATION

5.1 Introduction

Academic atomization processes typically entail liquids that have spatially and temporally uniform properties. Consistent atomization becomes challenging when liquid properties like viscosity and surface tension are inconsistent. Industrial slurries, gel fuel, and manure slurry, for example, could have widely varying (temporally or spatially) viscosity, which degrades atomization quality and exacerbates pumping requirements. High viscosity restricts the flow, straining the pump; viscosity’s restraining force prevents smaller ligaments and droplets from forming, thereby reducing atomization quality. How can consistent and efficient atomization of a liquid be achieved under these circumstances?

This question is answered by a Smart atomization framework that incorporates proportional integral derivative (PID) control algorithms into CFD simulations to adjust for changing liquid viscosity. The controllers operate continuously to account for dynamically and continuously varying process fluctuations. Hereafter, Smart atomization with PID control will be referred to simply as “Smart.” PID involves closed-loop feedback control widely used in industrial processes and has been incorporated into CFD models for testing.[71] The PID control is herein applied to WAVE (Wave-Augmented Varicose Explosions) atomization, where a pulsing twin-fluid atomizer utilizes a central hot gas flow (inverse of typical twin-fluid atomizer) and a wave-inducing inner design.[62] WAVE is designed for heating and disintegration of viscous, non-Newtonian slurries with a low gas-liquid mass ratio (GLR) of %2.7 (high efficiency).[19] An atomizer geometry of this type was first shown to be useful for wastewater treatment sludge atomization.[17] In short, annular slurry (cold) waves periodically "rise" into the central heating steam flow (see Figure 5.1) before crashing just outside the nozzle in the form of radial explosions. The high blockage ratio waves significantly contract the exit flow area, accelerating the steam to transonic states and causing temperature and pressure fluctuations at the steam-slurry interface which create a self-sustaining feedback loop of instabilities. Breakup of slurry sheets extending from the nozzle is facilitated by steam heating, wave impact momentum, and windward pressure buildup, while fine droplets are stripped away from the penetrating wave. The physics of WAVE atomization for banana puree have been extensively documented,[19, 20, 62] but the benefits of Smart atomization have never been explored.

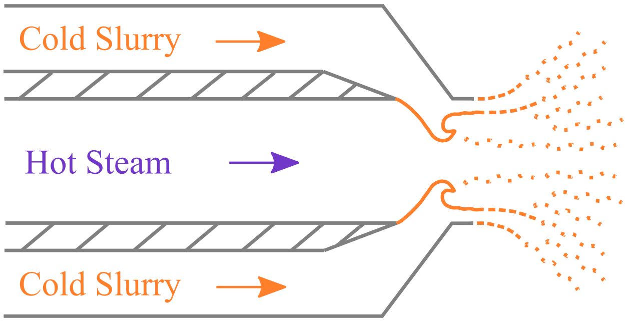

Figure 5.1 Side view of the WAVE atomizer geometry with an instantaneous sketch of the traveling wave.

Two independent controllers are incorporated into our CFD model. The first, henceforth referred to as "C1", adjusts the cold slurry flow based on the atomizer pressure drop. Its objective is to maintain a consistent pressure drop in the face of widely changing liquid viscosity, which translates to ensure consistent slurry feed pumping requirements.

The second, henceforth referred to as “C2”, compensates for the newly resulting gas-liquid momentum ratio (GLMR, defined as $\rho_g u_g^2/\rho_l u_l^2$) and adjusts the hot gas flow based on droplet size. While this description might imply they operate in series, they actually are working constantly in tandem. Here, ρ_g is the gas density, ρ_l is the liquid density, u_g is the gas bulk velocity, and u_l is the liquid bulk velocity. C2’s objective is to maintain consistent droplet sizes while the atomizer experiences widely varying 1) viscosity and 2) liquid flows resulting from C1 influences. C2 thus serves two roles, compensating for both C1 liquid flow (and thus momentum ratio) adjustments and liquid viscosity fluctuations. In short, a coupled controller system is used to protect atomization quality while ensuring slurry feed pump reliability.

An important application for Smart technology is manure slurry atomization for waste-to-energy conversion. Ever increasing energy demands and scarcity of resources drive the need for alternatives to conventional energy production. Manure is nothing if not plentiful and can already be harnessed for energy by processes like digestion, gasification, and pyrolysis.[72] An alternative, and potentially more efficient, means of energy conversion is direct spray injection of a concentrated manure slurry (non-Newtonian) into energy harvesting equipment, such as a steam boiler. This method could reduce processing costs (such as drying) to increase conversion efficiency. Additionally, it is known that shear has cleansing effects for manure slurries, and atomization is generally a high-shear process.[73]

Closed-loop feedback control for atomization technology could provide more robust spray processes for a wide range of applications. For example, active fuel spray control is of great interest for internal combustion engines (ICEs).[74] Despite past studies of control for combustion instabilities,[75-77] a 2019 review article points to the potential technology leap for ICEs and the need to develop new atomization control methods.[74] Most recently, Osuna-Orozco *et al.* demonstrated closed-loop feedback control of an air-water coaxial atomizer.[78, 79] A desired spray structure, defined as a certain liquid distribution, was acheived by adjusting swirl ratio and gas flow.[78] Electrostatic actuation can provide a third input to produce a desired spray liquid distribution.[79] The focus of these methods is adjusting certain input parameters (like swirl ratio) to produce a preferred spray state. In contrast, the focus of this present work is continuous process control to *simultaneously maintain* consistent atomization quality and pumping requirements in the presence of *significant viscosity (orders of magnitude) fluctuations*. We are adjusting uniquely for two measured variables, both droplet diameter and pressure drop in a coupled PID system. Additionally, our transonic pulsatile atomizer is uniquely designed for globally unsteady viscous slurry heating and disintegration, rendering coupled PID control challenging.

To our knowledge, this research represents the first tests of atomization using closed-loop feedback control for variable viscosity feedstock with a coupled PID controller system. A series of three Smart tests will be used to evaluate the efficacy of the coupled controller system for PID-assisted atomization. Test results will also provide guidance for improving the Smart approach. All three tests capture the system response to a pronounced step increase in viscosity, and test model rigor increases progressively. The hot assisting gas is steam for all three tests. Test 1 uses a basic mesh with a Newtonian slurry. Test 2 still uses a Newtonian slurry but with a more refined mesh and greater modeled azimuthal domain extent. For Test 3, Smart is applied to a WAVE model with an even finer mesh, where the impact of viscosity transition and feed rate changes on shear-thinning banana puree WAVE atomization is observed.

5.2 Methods

5.2.1 Computational Methods

An overview of the general computational approach for all three controller tests is provided here; key differences between tests are discussed in Section 2.3. We note again that test model rigor increases progressively from Test 1 to Test 3. For computational efficiency, the full, azimuthally symmetric atomizer geometry was reduced to a wedge with periodic boundary conditions on both azimuthal bounding faces. Almost all cells are hexahedral and swept in the general flow direction. The steam pipe and slurry annulus inlets (left of Figure 4.1) both have PID-controller-varied mass flow boundary conditions, with inlet temperatures of 393 K and 304 K, respectively. The outlet to the right of Figure 4.1 was set to atmospheric pressure. The nozzle exit and steam pipe diameters are both 0.016 m, and the slurry annular gap is 0.0098 m. The nozzle geometry is identical across all three tests, though the computational domain extent varies.

Equations 5.1-5.3 present the governing Navier-Stokes equations for multiphase flow. They are formulated in vector notation, and all properties are arithmetically phase-averaged (α is phase volume fraction). Fluid properties are represented as follows: ρ is density, C_p is constant pressure heat capacity, ζ is laminar conductivity, T is the static temperature, and p is pressure. Other symbols are here defined: t is time, u is the velocity vector, g is gravity, F is the surface tension force vector, μ_t is the turbulent viscosity, Pr_t

is the turbulent Prantdl number, τ is the laminar shear stress tensor, and τ_t is turbulent shear stress tensor.

$$\frac{\partial}{\partial t}(\alpha\rho) + \bar{\nabla} \cdot (\alpha\rho\bar{u}) = 0 \tag{5.1}$$

$$\frac{\partial}{\partial t}(\rho\bar{u}) + \rho\bar{u} \cdot \bar{\nabla}\bar{u} = \bar{\nabla} \cdot (\tau + \tau_t) - \bar{\nabla}\mathrm{p} + \left(\rho - \rho_{ref}\right)\bar{g} + \bar{F} \tag{5.2}$$

$$\frac{\partial}{\partial t}(\rho C_P T) + \bar{\nabla} \cdot [\bar{u}(\rho C_P T)] = \bar{\nabla} \cdot \left[\left(\zeta + \frac{\mu_t}{Pr_t}\right)\bar{\nabla}T\right] \tag{5.3}$$

The computational approach to CFD Smart tests is much the same as that outlined in Ref. 20, and these methods have been extensively validated for transonic, non-Newtonian airblast atomization.[24, 26-33] Ref. 61 provides a summary of validation exercises as well as representative mesh pictures for the different refinement levels. The previous validation exercises, conducted for another non-Newtonian fluid in a multi-stream atomizer, provide confidence in the computational approach. However, atomization experiments with banana puree in the current WAVE geometry are lacking, and these would add much value to the present study.

Despite past methods documentation, the framework used to solve the Reynolds-Averaged Navier-Stokes (RANS) and volume-of-fluid (VOF) equations in the commercial CFD solver ANSYS Fluent 2020 R1 are briefly outlined as follows. A k-ω turbulence model (“standard” or SST, depending on the controller test) and SIMPLE pressure-velocity coupling scheme were utilized. PRESTO! was used for pressure; second order upwind for momentum, energy, and density; and first order upwind for turbulence quantities. Geometric reconstruction (also known as “piecewise linear interface capturing” or PLIC)[25, 26] was used for the volume-of-fluid (VOF) interface. Slurry was modeled as incompressible, and we did not include temperature-induced slurry density changes into our CFD model. Time step varied depending on the model and mesh size, but Courant number was generally kept below 1.

We remind the reader that RANS does not resolve any turbulent structures, and true atomization mesh independence is likely impossible. Based on integral length scale estimates, the largest turbulent structures could affect droplet physics downstream of the waves. The scope of this study is limited to primary atomization physics, and we are ignoring the influence of turbulence on smaller droplets and secondary breakup. The mesh nomenclature is as follows: the coarsest is a “Base” mesh, which is then refined. The only cells not refined were upstream in the steam pipe and slurry annulus, far from any steam-slurry interfacial development. “Ref-1” refers to a single refinement, cutting each cell edge length in half in all three dimensions to increase the cell count by a factor of approximately 8. “Ref-2” refers to a second refinement, reducing cell size (and increasing cell count) yet again.

5.2.2 PID Control Algorithm Implementation

A PID control algorithm was implemented as user-defined functions (UDFs) in ANSYS Fluent 2020 R1 for the two controllers. Equation 5.4 is the discrete velocity PID algorithm used, where c is the controlled variable, e is the controller “error,” n is the discrete time stamp, Δt is the sampling time, and K_c, τ_I, and τ_D are the controller’s proportional, integral, and derivative gain constants, respectively. The error is the difference between the measured variable and setpoint (not an error between CFD and experimental results), where measured values are time-averaged within each Δt sampling period. The sampling time was largely on the order of 1×10^{-3} s; a physical implementation of this system would require a pump to respond at this time scale, which could present challenges. Figure 5.2 illustrates the PID controller feedback loop in the form of a block diagram, where the process (controlled variable) is adjusted to keep the output (measured variable) at setpoint. Proportional gain helps immediately and linearly adjust the controlled variable to reduce the error, integral gain considers the combination of how long the error has been in effect plus to what extent, and the derivative gain takes into account how quickly the error is approaching zero from either the positive or negative directions. In concert, they each contribute components to each controller which drive the respective errors to zero as quickly as is physically possible. It can be thought of as a primitive form of artificial intelligence which does not require training. Processes, which can be thought of as individual physics manifestations within a given control volume, have unique natural response timescales. Controller algorithms should be tuned to accommodate the governing processes of the system.

$$\Delta c_n = c_n - c_{n-1} = K_c\left[(e_n - e_{n-1}) + \frac{\Delta t}{\tau_I}e_n + \frac{\tau_D}{\Delta t}(e_n - 2e_{n-1} - e_{n-2})\right] \quad (5.4)$$

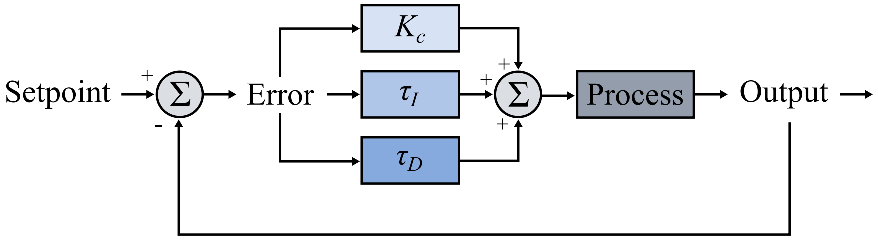

Figure 5.2 PID controller feedback loop illustrated with a block diagram.

For C1, the measured variable is liquid pressure drop, and the controlled variable is liquid mass flow. Pressure at the liquid inlet represents pressure drop, as the outlet is constant at 1 atmosphere, absolute. Since “pressure” and “pressure drop” are functionally the same here, they are used interchangeably in referring to the measured variable for C1 in the following discussions. For C2, the measured variable is droplet size, and the controlled variable is steam mass flow. Droplet size is captured by a UDF as the volume-averaged Sauter mean diameter (SMD) in a series of 10 volumes spaced axially away from the injector.[29] For each test, the PID input variable is one of these 10 volume-averaged SMD measures, about halfway between the nozzle exit and the end of the computational domain. Future efforts ought to record the entire droplet distribution, which would make available other droplet statistics besides SMD. Two protections are added to each controller to maintain a stable and practical system: 1) mass flow rates of either phase cannot be set below zero and 2) measured values outside of three standard deviations (computed instantaneously) are not included in the averaging process. An operating range for GLR could be included as a third protection measure. The steam pipe and slurry annulus inlets both have PID-controller-varied mass flow inlets. For the Smart tests, one, none, or both controllers can be engaged to observe various responses to a step increase in viscosity. “C0” means no controllers are engaged, “C1” implies only C1 is engaged, “C2” designates that only C2 is engaged, and “C12” means both C1 and C2 are engaged. Rather than utilizing C12 against viscosity fluctuations, an alternative use of these controllers for a liquid fuel with constant properties would be to use C2 to hit a target SMD setpoint while

C1 maintains a constant air-fuel ratio. In response to a user change in SMD setpoint, the controllers would modify flow rates to reach a new quasi steady state.

Before discussing C1 and C2 controller mechanics, more clarity surrounding pressure drop is necessary. The subscript “s” will be used for the liquid phase (slurry), and the subscript “g” will be used for the gas phase (steam). The subscript “i” will be used as a placeholder for either phase. The total slurry pressure drop (Δp_s) is made up of two components, $\Delta p_{1,s}$ and $\Delta p_{2,s}$,. $\Delta p_{1,s}$ is the pressure drop as it flows along the slurry annulus, and $\Delta p_{2,s}$ is the interfacial pressure drop at the nozzle exit, i.e., the force required to break through the tangentially flowing steam. Each contributes to Δp_s, but they are affected by different mechanisms. Changes to slurry viscosity, as well as changes to slurry mass flow, will affect *both* $\Delta p_{1,s}$ and $\Delta p_{2,s}$ (that is, Δp_s). Changes to steam mass flow rates will only affect $\Delta p_{2,s}$. Steam also has a $\Delta p_{2,g}$ where it is forced to interact with the slurry wave but not a significant $\Delta p_{1,g}$. Each $\Delta p_{2,i}$ at the interface includes both normal (breakthrough) forces and tangential (frictional) forces as the steam and slurry interact while exiting the nozzle. Furthermore, since the steam is compressible, changes in $\Delta p_{2,g}$ at the nozzle exit will feed pressure back to the steam inlet, which will alter steam velocity (and thus the phase momentum ratio) even if the steam mass flow were fixed.

While the C1 and C2 control algorithms are functionally independent, physical interaction between variables couples the controllers. Figure 5.3 illustrates the relationship between the two controllers and the interrelated physics. As C1 adjusts the slurry mass flow rate ($\dot{m}_{slurry}$) to affect $\Delta p_{1,s}$, droplet size (SMD) and $\Delta p_{2,s}$ are also impacted. Changes in $\dot{m}_{slurry}$ causes a shift in the phase momentum ratio, which is important for the atomization process. Similarly, when C2 adjusts the steam mass flow rate ($\dot{m}_{steam}$) to affect SMD, $\Delta p_{2,s}$ (but not $\Delta p_{1,s}$) is also impacted. Changes to either $\dot{m}_{slurry}$ or $\dot{m}_{steam}$ will alter $\Delta p_{2,s}$ and consequently the steam inlet velocity because of pressure feedback (since the steam is compressible). Thus, coupled physics cause both C1 and C2 to affect each other's outcomes in a coupled controller system. Not shown in Figure 5.3 is the internal physics feedback loop between temperature- and shear-dependent viscosity and interfacial instabilities. Various steam and slurry flows lead to variable interfacial heating dynamics, which affects $\Delta p_{2,s}$ and $\Delta p_{2,g}$.

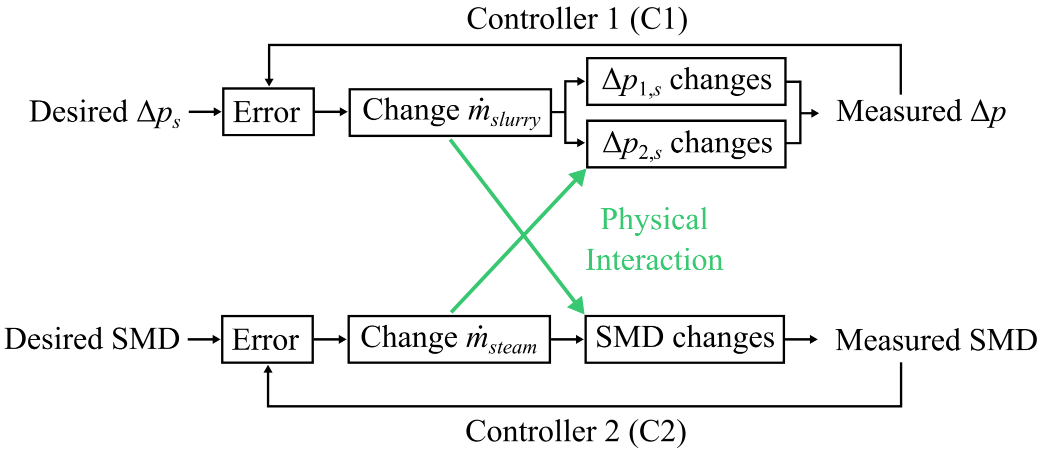

Figure 5.3 Despite independent control algorithms, the C1 and C2 controllers are coupled by physical interactions.

5.2.3 Smart Atomization Test Descriptions

The CFD model for Test 1 employs an unconventionally coarse Base mesh, simply as an initial proof-of-concept. It is understood that this model is *not* for predicting accurate droplet sizes or wave generation physics. The full 360° axisymmetric atomizer geometry was reduced to a 1/32 (11.25°) wedge with a total computational cell count of 250,000.

The slurry is Newtonian, and the steam is modeled as incompressible. The slurry annulus is considerably longer than the steam pipe, extending approximately 10 times farther back. This “long slurry entry” strengthened the correlation between slurry viscosity and pressure drop in the annulus, creating a more realistic scenario for PID control testing, i.e. creating $\Delta p_{1,s}$. The computational domain extends 10 orifice diameters beyond the atomizer orifice in the axial direction.

Test 1 includes the response of all four combinations of controllers to a viscosity shift. For the PID input, SMD is measured 5 nozzle diameters away from the orifice. Slurry viscosity is initially set to a constant 0.05 kg/m-s. The resulting pressure and SMD are used as setpoint values for the controllers. All tests began with steam and slurry flow rates necessary to maintain these “baseline” setpoint values. Viscosity is then suddenly changed to 5 kg/m-s for a 100-fold step increase. After the viscosity shift, four separate simulations model the following scenarios: C0, C1, C2, C12. Each test follows this pattern: a *baseline* simulation models the system at quasi steady state (QSS) with a baseline (lower) viscosity value. After the viscosity is step-increased to a higher value, a *response* simulation is run for each combination of controllers under investigation. The C12 response is of greatest interest since this represents the coupled controller system, but comparisons among the C0/C1/C2 responses alsoprovide valuable insights.

Mesh resolution and azimuthal domain extent are increased for Test 2. The mesh is refined once in the entire atomization domain (Ref-1). The wedge angle is increased from 11.25° to 45° for a total of 2.3 million computational elements. The same Newtonian slurry and steam of Test 1 are used again here, and both are modeled as incompressible. To increase the correlation between the slurry viscosity and pressure drop in the annulus even further than Test 1, the long slurry entry is shorted and includes a section of porous media. The porous media is a proxy for $\Delta p_{1,s}$ over a much longer piping system, and this pressure drop is linear with viscosity in laminar flow based on the well-known Darcy's Law. The computational domain beyond the nozzle orifice is shortened, and SMD for PID input is measured about 2.5 nozzle diameters away from the orifice. Since the computational domain is shortened with each test to reduce computational cost, the SMD measure location moves successively closer to the nozzle. Like Test 1, the baseline viscosity of 0.05 kg/m-s was increased by 100x to 5 kg/m-s. Then, three separate simulations model C0, C2, and C12 responses. The C1 response was not included to minimize computational expenses and run time.

Finally, Test 3 represents PID-assisted WAVE atomization. The mesh is refined twice (Ref-2), and the wedge angle is kept at 45°, with 8.3 million computational elements. Increasing to 90° does not significantly alter droplet sizes.[19] While full mesh independence was established for Ref-3, the Ref-2 axial SMD profile is sufficiently close to mesh independence for controller testing.[19] The full non-Newtonian banana puree viscosity UDF, which uses the Herschel-Bulkley model (shear- and temperature-dependent), is incorporated into the CFD model.[20, 38, 67] As with Test 2, a porous media section in the puree annulus creates a direct linear correlation between viscosity and $\Delta p_{1,s}$. Unlike Tests 1 and 2, the steam is modeled as compressible (ideal gas with temperature- and pressure-dependent density). The SMD for C2 measured value is sampled 1 nozzle diameter away from the orifice. The baseline viscosity, modeled by the standard viscosity UDF, increased by a factor 10, after which the response of C12 is captured. A slight change in the control algorithm for Test 3 made the sampling time Δt a function of the convective time scale. This is important, because atomization dynamics are suppressed as feed flows are adjusted for the higher viscosity.

Table 5.1 provides an overview of the differences across Smart tests.

Table 5.1 Summary of setup and differences between the three Smart tests.

Test Setup	Test 1	Test 2	Test 3
Mesh Resolution	Base	Ref-1	Ref-2
Wedge Angle	11.25°	45°	45°
Annulus	Long	Porous Media	Porous Media
Liquid	Newtonian Slurry	Newtonian Slurry	Non-Newtonian Puree
Steam	Incompressible	Incompressible	Compressible
SMD Control Point	5 diameters	2.5 diameters	1 diameter
Viscosity Shift	100x	100x	10x
Response	C0, C1, C2, C12	C0, C2, C12	C12

5.3 Results and Discussion

5.3.1 Test 1

Figure 5.4 shows the measured and controlled variables for each scenario across the viscosity change at normalized flow time = 0. All data are non-dimensional in this manner: pressure and SMD data are normalized by their respective setpoints (equivalent to starting QSS values), and mass flows are normalized by the starting value just before the viscosity change. Flow time is normalized by the convective time scale for slurry droplets to travel roughly five diameters axially away from the nozzle exit (where SMD is measured for controller Test 1). The bulk velocity is around 150 m/s, making the convective time scale around 4×10^{-4} s.

The slurry inlet pressures for C1 and C12 behave similarly, successfully adjusting to the dramatically higher viscosity level and remaining much lower than those for C0 and C2. Pressure initially doubles in response to the viscosity increase but is driven back down to the setpoint as the slurry mass flow is decreased. For C0 and C2, pressure initially increases by a factor of about 2.5. The C0 pressure then remains constant, while the C2 pressure continues to increase because of the increasing steam flow. Table 5.2 further elucidates the controller responses with time-averaged (TA) pressure and temporal standard deviation statistics. C1 and C12 pressures experience no change in mean and a slight decrease in standard deviation through the viscosity shift (the transition period has been removed for these statistics). C0 and C2 stand in stark contrast; the mean and standard deviation increase dramatically for both. C2 represents the largest change with a 320% increase in mean and a 530% increase in standard deviation. Interestingly, the C1 and C12 slurry flows begin to diverge after beginning near one another. The C12 slurry flow is increasing because of decreasing steam flow, lowering slurry pressure and causing C1 to increase the slurry flow. This phenomenon is part of the interplay between controllers illustrated in Figure 5.3.

C2 and C12 maintain lower and more stable SMD values compared to C0 and C1. While the C2 and C12 TA SMDs remain unchanged through the viscosity change, the C0 and C1 TA SMDs increase by 20% and 40%, respectively (Table 5.2). While appreciable, we expected stronger effects by the viscosity change on the TA SMD without controller intervention. Our preliminary results indicate a surprisingly robust system in terms of average SMD. The most notable change in SMD, as is visually evident from Figure 5.4, is the large increase in variation for C0 and C1. While the SMD standard deviation for C2 and C12 increases moderately, it increases by 450% and 520% for C0 and C1, respectively.

C2 and C12 adjust the steam flow in different ways because of the difference in slurry flow. C2’s behavior is expected: the steam flow increases to decrease the SMD resulting from the changes in momentum ratio. The C12 steam flow swings both above and below the constant C1 value. We thus arrive at a useful and obvious conclusion: engaging C2 allows not only for increased steam usage to maintain the SMD setpoint but also for decreased steam usage as necessary. In other words, the coupled controller system is free to use only what steam it requires to maintain atomization quality. It is clear, however, that the C12 steam flow has not reached QSS. The aforementioned interplay between two controllers seems to be at work and will dictate how the steam flow adjusts moving forward.

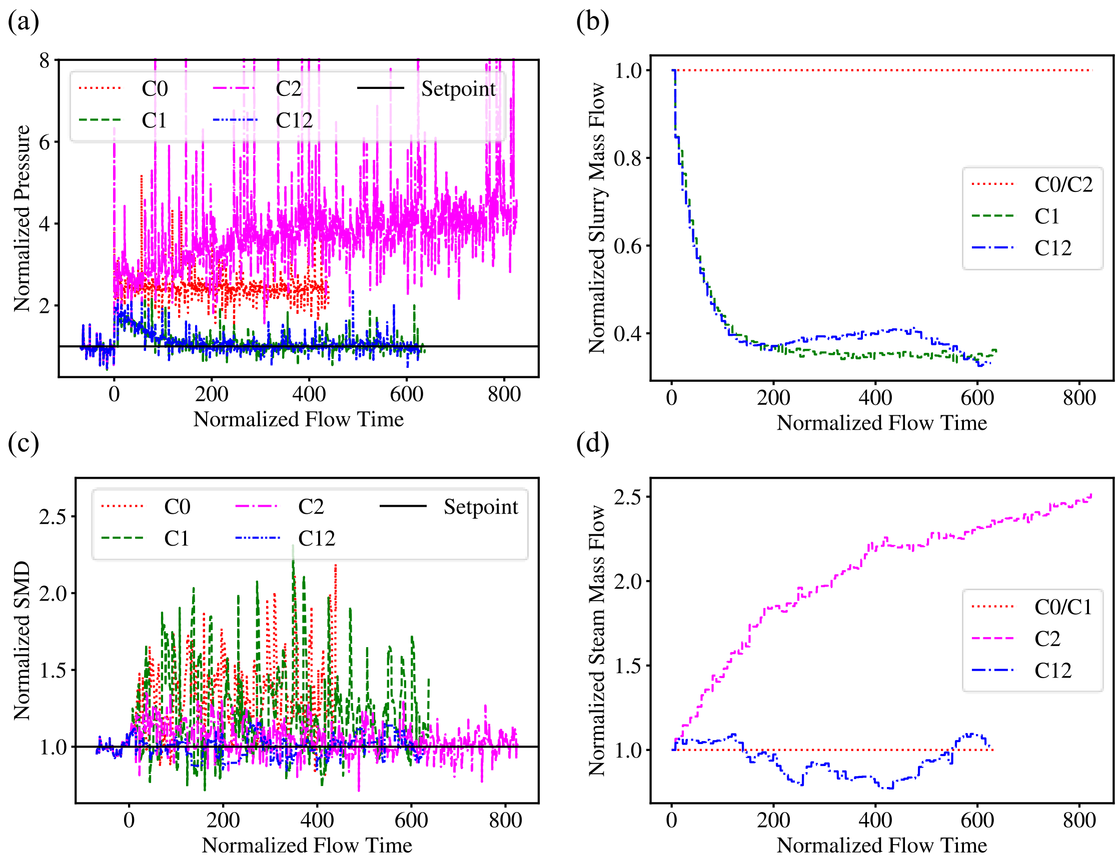

Figure 5.4 Test 1 controller response plots showing (a) slurry pressure (equivalent to pressure drop), (b) slurry mass flow rate, (c) Sauter mean diameter (SMD), and (d) steam mass flow rate.

Table 5.2 Descriptive statistics for SMD and pressure in Test 1 presented as the ratio of a value after the 100x slurry viscosity change to that before the viscosity change (excluding transition regions).

	Ratio of Means		Ratio of Standard Deviations	
Case	SMD	Pressure	SMD	Pressure
C0	1.4	2.5	5.5	1.8
C1	1.2	1.0	6.2	0.9
C2	1.0	4.2	1.5	6.3
C12	1.0	1.0	1.8	0.9

In summary, Figure 5.4 and Table 5.2 provide an initial demonstration of 1) the efficacy of the coupled controller system and 2) the need for *both* controllers. The C1 controller is clearly necessary to maintain a constant slurry pump requirement. Both C0 and C2, individually, would be problematic, as the increase in pressure may be unacceptable. The C2 pressure increases and varies most dramatically; therefore, C2 alone is not a preferred option despite its successfully maintaining an acceptable SMD. The dramatic decrease in slurry flow for C12 resulted in less than the expected increase in steam flow, demonstrating the flexibility of the C2 controller.

Before moving to Test 2, which involves a finer mesh than Test 1, mesh resolution effects are elucidated. Slurry atomization instantaneous snapshots with various meshes are illustrated in Figure 5.5, revealing atomization differences and similarities for three mesh refinement levels (Base, Ref-1, and Ref-2). Figure 5.5 is a cross-section, equivalent to the perspective in Figure 4.1, which shows representative contours of slurry (red) and steam (black). Each case was run with the baseline viscosity of 0.05 kg/m-s. The only distinction between these three models and that used for Test 1 is that these have a 90° azimuthal angle. It must be emphasized that even Ref-1 and Ref-2 do not necessarily predict mesh-independent droplet sizes. These models are intended for preliminary assessment of mesh sufficiency and atomization characteristics.

A comparison of the Base, Ref-1, and Ref-2 cases in Figure 5.5 show that the general characteristics of WAVE atomization remain relatively unchanged as the mesh is refined. The Base case (left in Figure 5.5) represents the mesh element size used for Test 1. While finer meshes do result in production of smaller droplets, the general atomization characteristics are largely the same through 2 refinement levels. Of particular importance to our work is this: if a controller configuration is effective or ineffective for the Base case, it should perform comparably for the Ref-1 or Ref-2 case. In other words, the Base mesh is sufficient for an initial Smart proof-of-concept.

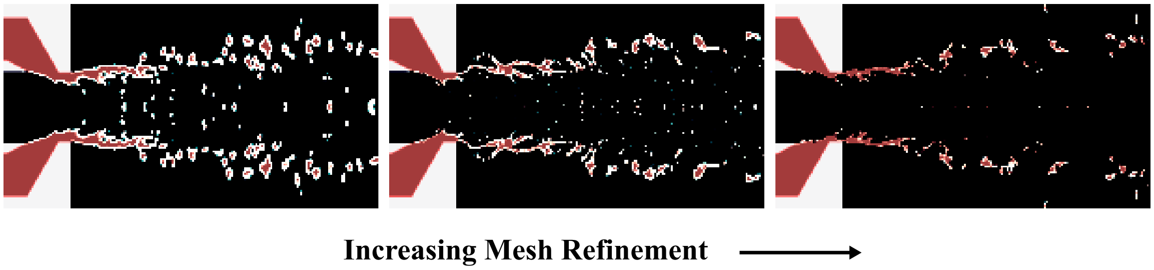

Figure 5.5 Representative contours of slurry (red) and steam (black) with a slurry viscosity of 0.05 kg/m-s, demonstrating the change in droplet resolution as the mesh is refined.

5.3.2 Test 2

The results of Test 2, though similar in some ways to Test 1, brought differences. An important factor in these differences is the strengthened relationship between pressure drop and viscosity. For Test 2, a porous media section replaced the long slurry annulus to create a significantly higher $\Delta p_{1,s}$ and sensitivity of pressure to viscosity changes. Pressure, SMD, and mass flow rates are given in Figure 5.6 in the same normalized manner as Test 1. A slightly different convective time scale of 3×10^{-4} s is used to normalize the flow time, as the location where SMD is measured is closer to the nozzle exit in Test 2.

After the viscosity shift, the pressure initially increases by over 5000%, which is a much greater jump than was observed for Test 1. Again, this was expected because of the porous media addition to the model. However, the pressure only increased by about half the viscosity increase factor of 100 because the viscosity primarily affects $\Delta p_{1,s}$. Pressure contours for the Test 2 baseline in

Figure **5.7** show the two contributing pressure drops ($\Delta p_{1,s}$ and $\Delta p_{2,s}$) were roughly equal. As the interface is dynamic, along with $\Delta p_{2,s}$,

Figure **5.7** only represents only a single realization. Since the porous media only accounted for half of the total pressure drop, a 100x change in viscosity only created a 50x change in pressure drop. More will be highlighted on Δp_s in the next section. The pressure then returns back to setpoint for C12 but remains relatively constant for C0 and C2, as they are not designed to address pressure spikes. Table 5.3 provides TA pressure and SMD statistics. Note in particular the substantial increase in pressure standard deviation for C0 and C2 (by factors of 4.9 and 17, respectively). C12, on the other hand, actually experiences a decrease in pressure variation after the viscosity shift.

After an initial increase, the SMD is brought back to setpoint for both C2 and C12 as designed. The TA SMD increases by about 180% for C0 with a significant increase in variability (see Table 5.3), indicating the necessity of C2 to maintain droplet size. The steam flows for C2 and C12 are briefly similar before diverging. As expected, the C2 steam flow increases to drive down SMD. In contrast, the C12 steam flow begins to plummet and drops below the C0 steam flow. The SMD is slightly below setpoint, even as the steam flow continues its downward trajectory. The low SMD occurs because of the changing system dynamics as the slurry flow is significantly reduced (more on this in the next section). By the end of the test, steam flow had bottomed out at its lower limit, highlighting the need for controller adjustments to accommodate these circumstances.

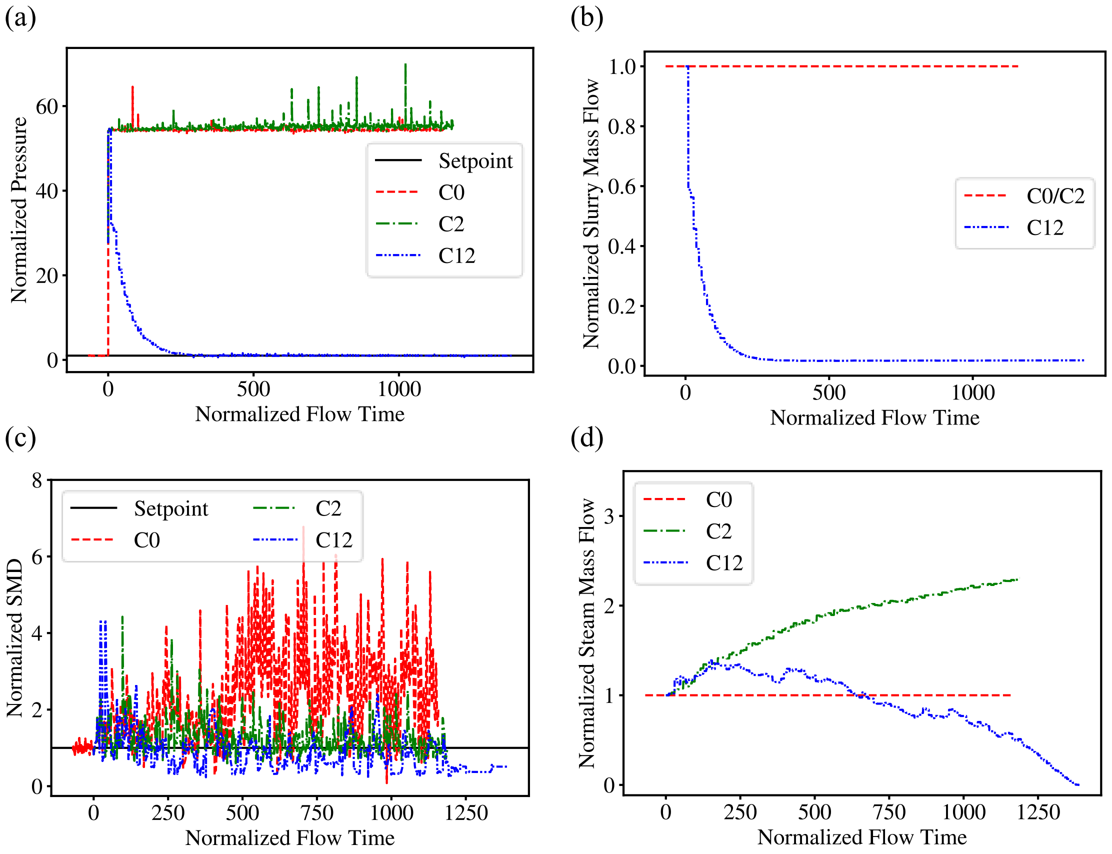

Figure 5.6 Test 2 controller response plots showing (a) slurry pressure (equivalent to pressure drop), (b) slurry mass flow rate, (c) Sauter mean diameter (SMD), and (d) steam mass flow rate.

Table 5.3 Descriptive statistics for SMD and pressure in Test 2 presented as the ratio of a value after the 100x slurry viscosity change to that before the viscosity change (excluding transition regions).

	Ratio of Means		Ratio of Standard Deviations	
Case	SMD	Pressure	SMD	Pressure
C0	2.8	54	13	4.9
C2	1.1	55	3.2	17
C12	0.7	1.0	4.3	0.7

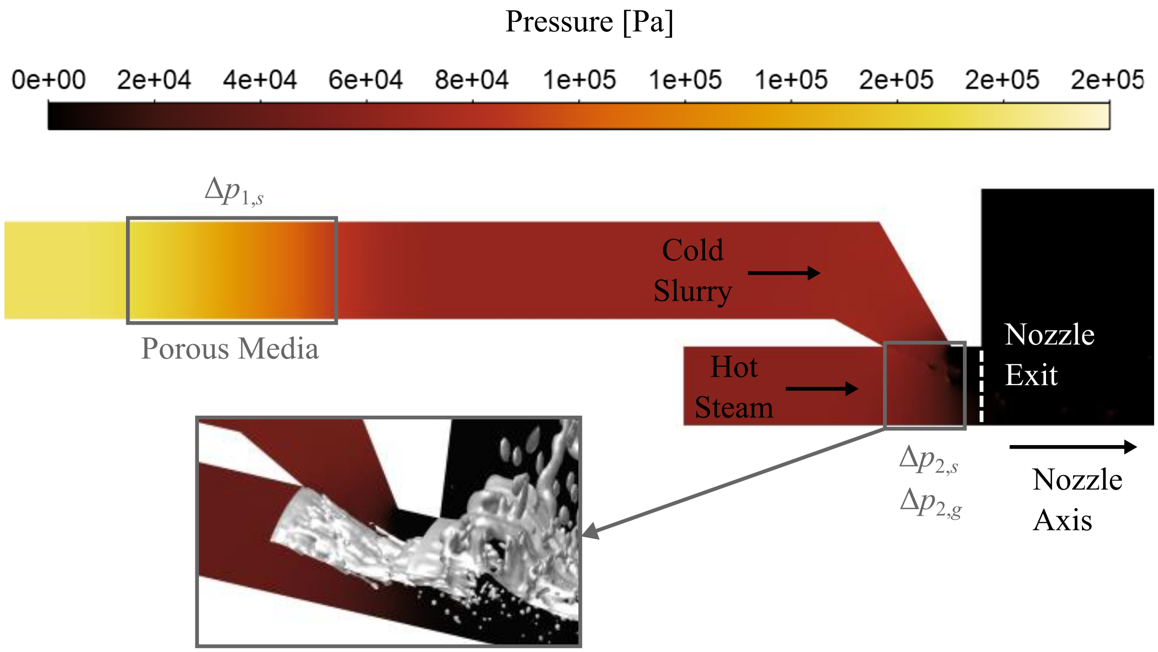

Figure 5.7 Side view of instantaneous pressure contours for half of the axisymmetric geometry (top).

5.3.3 Test 3

Test 3 included the complete WAVE atomization model with shear-thinning banana puree as the slurry and compressible steam. For this test, the viscosity was increased by a factor of 10 rather than a factor 100 like Tests 1 and 2, and only the C12 response is captured. Once again, pressure, SMD are normalized in the same manner as Tests 1 and 2. Rather than convective time scale, the flow time is normalized by the "wave time" of the system.[62] Wave time, which is equivalent to the pulsing time scale and around 0.001 s (about 10 convective times), reflects the frequency at which slurry waves form regularly inside the nozzle, roll up over the nozzle exit lip, and crash back into the proceeding thin slurry film.

The C12 response plots are presented in Figure 5.8. In response to the 10x shift in viscosity, pressure initially increases by about 400%. This increase in pressure is comparable to that for Test 2 (1/10th the viscosity increase produced approximately 1/10th the pressure increase). Thus, modeling the slurry as non-Newtonian roughly maintains the sensitivity of $\Delta p_{1,s}$ to viscosity changes. Pressure returns to setpoint as the slurry flow is reduced. As with Test 2, slurry flow rate is reduced dramatically, ending at just 2.5% of its original value. To keep the pressure moving steadily towards setpoint during this transition, the proportional gains for both controllers were reduced by a factor of 4 at normalized flow time = 24. We suggest that variable gains could improve the controller system; fuzzy logic could provide an effective means of tuning the gains in real time.[80]

The SMD initially increases by 125%. In response, the steam flow increases, and the SMD fluctuates around setpoint. Then the SMD drops far below setpoint, and the steam flow plummets. The flat line towards the end of the test is where the steam flow reaches the lower limit (as imposed in the control algorithm) of 0.0003 kg/s. The reader will notice that the time between steam flow adjustments gradually increases towards the end of the test before the steam flow bottoms out. This is a consequence of the variable sampling time implemented in the control algorithm for Test 3, where sampling time adjusts with the convective time scale. As flow rates reduce towards the end of the test and the convective time scale lowers, the sampling time increases.

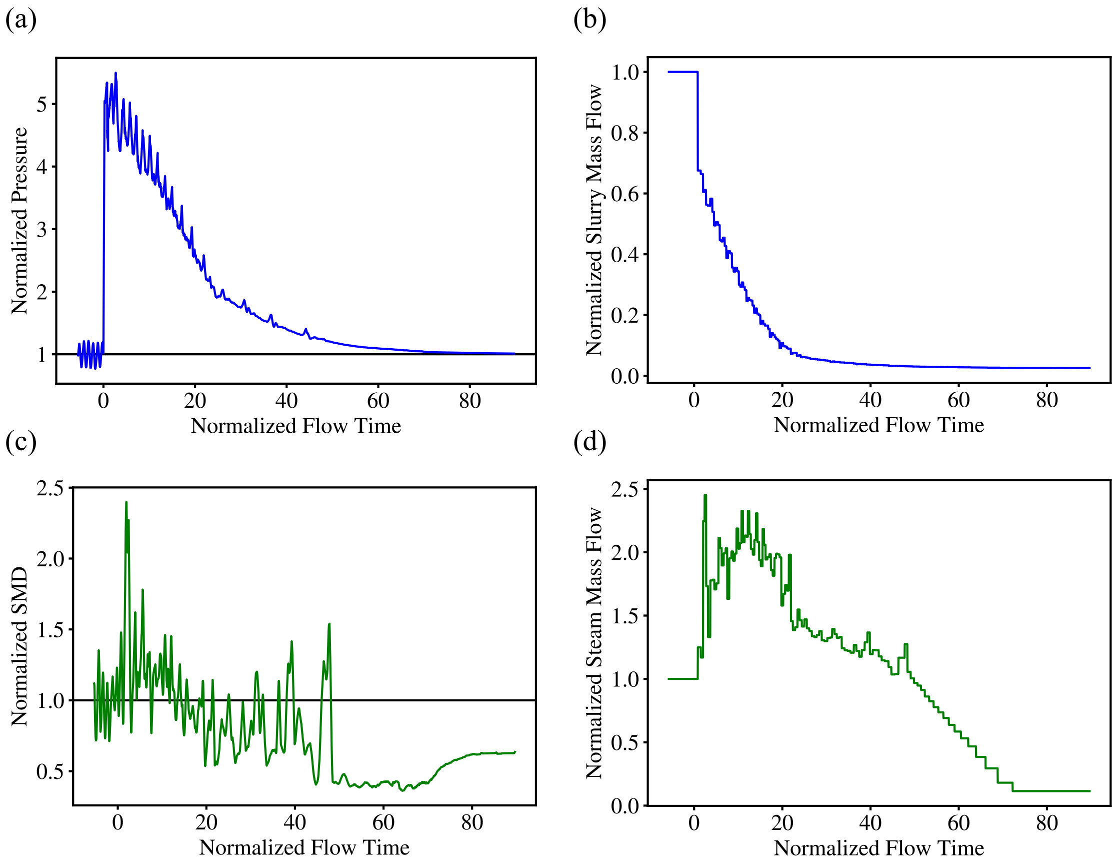

Figure 5.8 Test 3 controller response plots showing (a) slurry pressure drop, (b) slurry mass flow rate, (c) Sauter mean diameter (SMD), and (d) steam mass flow rate.

The outcome for C12 is best explained by the reduction in slurry flow rate. When the pressure increases by 400%, the slurry flow rate plunges down to 2.5% of its original value. Consequently, the atomization characteristics change, as illustrated by Figure 5.9. The top of Figure 5.9 provides an instantaneous snapshot of WAVE atomization as it has been studied.[19] The bottom of Figure 5.9 provides a snapshot of the atomization by the end of Test 3. There, globs of puree burst more slowly from the nozzle. Meanwhile, small droplets are being stripped off, which explains why SMD stays so far below setpoint. It appears that under the Test 3 circumstances (namely, a long piping system), the pressure and SMD setpoints are not simultaneously achievable while operating within the bounds of the current controller configuration. We propose that to accommodate such circumstances as are presented in Test 3, an additional control knob is needed.

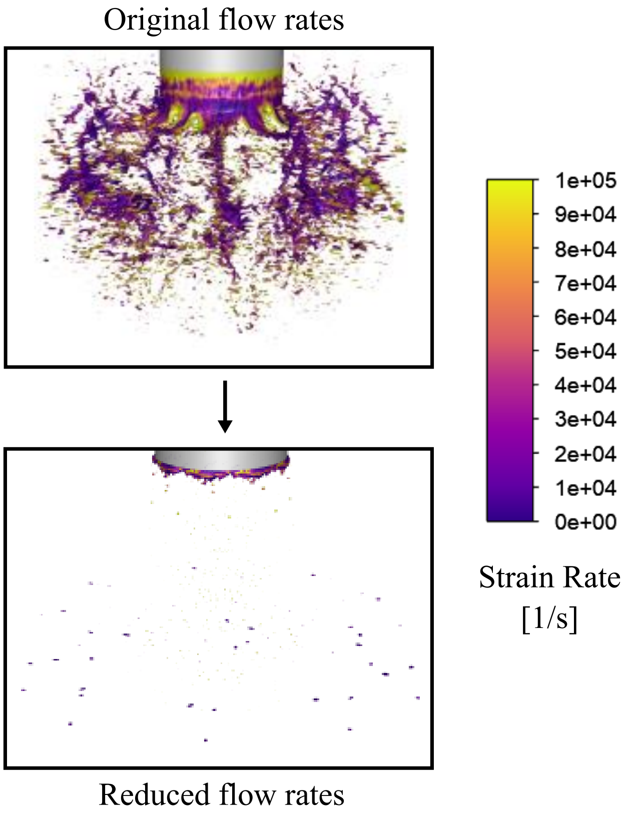

Figure 5.9 Representative snapshots from Test 3 showing atomization before the viscosity shift and at the end of the test.

Important dimensionless numbers from before the viscosity shift (start) and the end of Test 3 are listed in Table 5.4. The numbers are defined as follows: Weber number (We) $= \rho_g V_g^2 D_o / \sigma$ and Reynolds number (Re) $= \rho V_b D_o / \mu_l$. The Ohnesorge number ($Oh = \mu_l / \sqrt{\rho_l D_o \sigma}$) is around 9.4×10^{-3} before and after. Steam Mach number is reported at the steam inlet. Here ρ is the average density across both phases, ρ_g is steam density, ρ_l is the slurry density, V_b is the bulk velocity (both phases), V_g is the steam velocity at the inlet, σ

is surface tension, μ_l is the slurry dynamic viscosity, and D_o is the orifice diameter. We decreases by two orders of magnitude, and Re decreases by one order of magnitude, both largely driven by the reduction of slurry and steam velocities. The Mach number at the steam inlet is reduced to 1/5th the original value. Steam Mach number at the nozzle exit varies within a given wave cycle as the slurry blockage changes; it starts in the transonic range and even touches supersonic with a slurry-reduced exit area but then falls to below Mach 0.1. During the test, the GLR rises from 2.7% to 12% because of the fall in slurry flow rate (although both flows fall significantly). Meanwhile, the gas-liquid momentum ratio increases from 52% to 1500%.

Table 5.4 Dimensionless numbers describing the flow before the viscosity increase (start) and at the end of Test 3.

	Start	End
We	3.2×10^3	60
Re	1.1×10^5	1.8×10^4
Mach	0.22	0.043
GLR	2.7%	12%
GLMR	52%	1500%

Figure 5.10 illustrates the change in wave character from the beginning to the end of Test 3. By the end of the test, some waves are still observed, but they are smaller and less frequent. The annular slurry sheet that stretches out from the nozzle before the wave crashes largely disappears. While a pulsing characteristic is maintained, the frequency is lower. As the wave blockage ratio decreases, steam acceleration above the wave and pressure buildup behind the wave both decrease as well. Two important atomization

mechanisms are abated: wave impact momentum and pressure buildup. Additionally, droplets are primarily stripped from the waves as opposed to the flicking, buckling, and breaking of wave crests in the steam flow.[19, 20, 62]

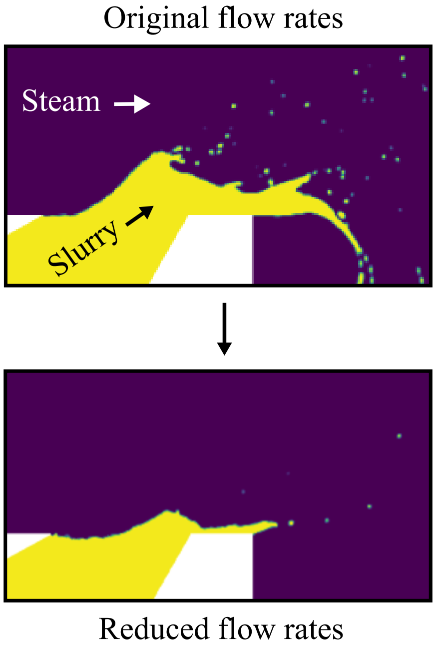

Figure 5.10 Representative instantaneous snapshots from Test 3 showing a side view of wave formation inside the nozzle.

During the course of the test, $\Delta p_{1,s}$ becomes the dominant contributor to the total Δp_s. At the same time, $\Delta p_{2,s}$ and $\Delta p_{2,g}$ both fall by an order of magnitude. Figures 11 and 12 illustrate changes in the interfacial pressure drop ($\Delta p_{2,i}$) for slurry and steam, respectively. The left of each figure is $\Delta p_{2,i}$ before the viscosity shift, and the right is $\Delta p_{2,i}$ at the end of Test 3. The “before” (left) slurry and steam driving pressures are roughly equal, and four distinct wave cycles are observed. The “after” (right) slurry and steam pressures are again roughly equal, though an order of magnitude lower. The slurry is having to work less to move into the steam flux (i.e., $\Delta p_{2,s}$ falls), and the steam is not being blocked any longer by large slurry waves (i.e., $\Delta p_{2,g}$ falls). $\Delta p_{2,g}$ falls slightly more due to the drop in steam density. As flow rates are reduced, wave frequency falls to less than a quarter of the original frequency.

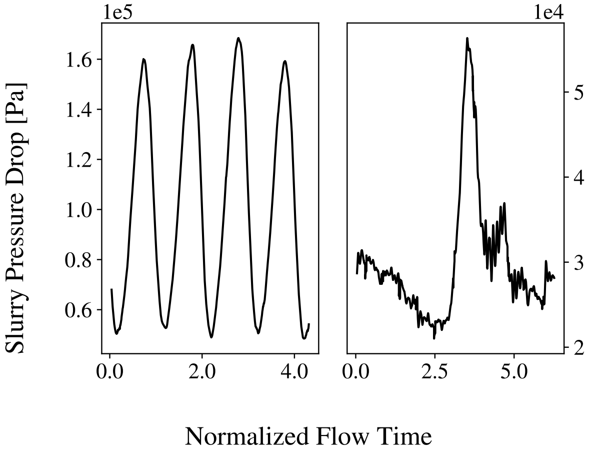

Figure 5.11 Slurry interfacial pressure drop ($\Delta \boldsymbol{p_{2,s}}$) at the nozzle exit before the viscosity shift (left) and at the end of Test 3 (right).

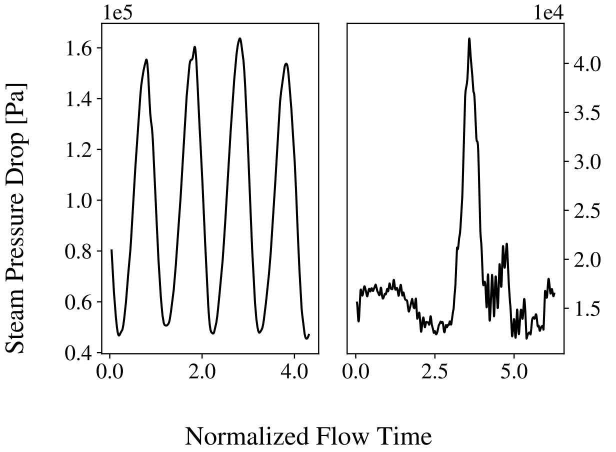

Figure 5.12 Steam interfacial pressure drop ($\Delta p_{2,g}$) at the nozzle exit before the viscosity shift (left) and at the end of Test 3 (right).

Figure 5.13 shows an unraveled view of the wave with representative snapshots before the viscosity shift (left) and at the end of Test 3 (right). The annular wave, whose shoreline is curved, has been unraveled onto a flat shoreline, similar to waves on a beach.

Both pictures in Figure 5.13 show instantaneous realizations where the wave is roughly peaking. The slurry surface is colored by directional derivative of pressure normal to the surface ($-\overline{\nabla}\mathrm{p} \cdot \overline{\nabla}\alpha_s$, where p is pressure and α_s is the slurry phase volume fraction). Positive and negative values represent gas decelerating and accelerating toward the slurry, respectively.

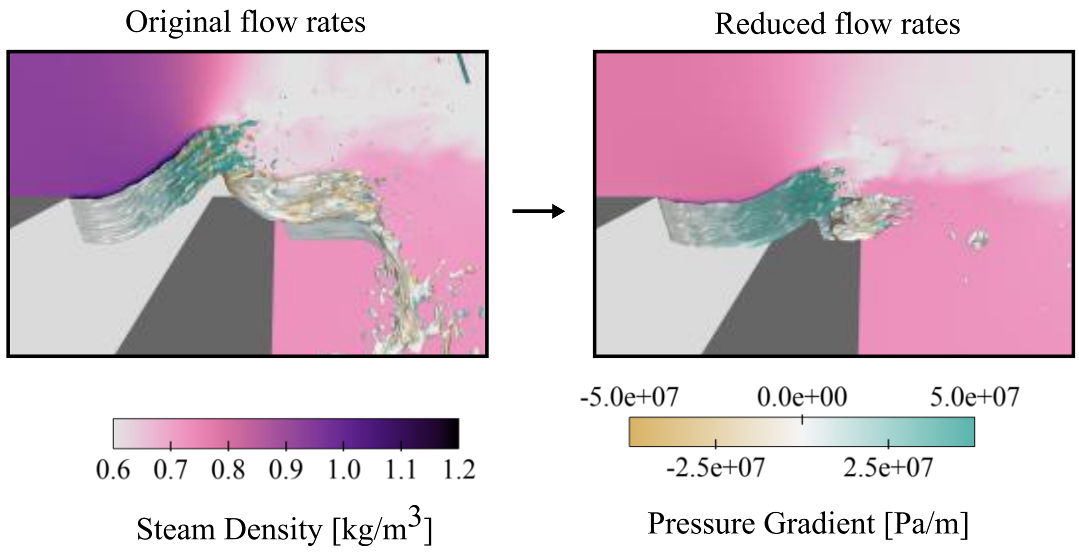

Figure 5.13 Representative snapshots of the unraveled wave with slurry surface colored by directional derivative of pressure normal to the surface and contours of steam density in the background.

Both before and after the test, the pressure gradient is largely neutral in the wave's wake and positive its windward side. In other words, the steam is decelerating as it hits the windward side of the wave. Especially before the viscosity shift, a negative pressure gradient, or "suction," appears on the leeward side of the wave as it curls up. The variation in gradient direction (both positive, blue, and negative, brown) on the windward side highlights the presence of Rayleigh-Taylor instabilities (RTI).[20] A visual inspection shows reduced RTI activity by the end of the test, with a less rippled windward wave surface and a mostly positive pressure gradient. Steam density fluctuates with the wave cycle as steam is compressed and decompressed, which feeds back to the inlet to affect steam pressure. Both parts of Figure 5.13 show a thin region of higher density steam (more compressed and cooled by the slurry) over the windward surface of the wave. The compression and cooling could lead to steam condensation here, but phase change is not included in our modeling approach. Future work ought to include a more thorough heat transfer analysis, as steam condensation could be important. As slurry and steam flow rates subside and wave dynamics become less influential towards the end of the test, overall steam density falls.

5.4 Conclusion

We have presented demonstrations of Smart atomization for variable-viscosity slurry heating and disintegration in a transonic pulsatile twin-fluid atomizer. PID control algorithms were incorporated into CFD simulations to model the Smart coupled controller system (both C1 and C2, referred to as "C12"). Smart continuously and simultaneously adjusts the cold slurry and hot gas flow rates to maintain a consistent slurry pressure drop (C1) and droplet SMD (C2). Coupling allows both to occur simultaneously, resulting in complex physics interactions related to heating and interfacial breakup. In addition to the total Δp_s, changes to slurry flow alter the gas-liquid momentum ratio, which impacts the SMD. On the other hand, gas flow changes will impact the momentum ratio, $\Delta p_{2,g}$, and $\Delta p_{2,s}$,which represents the interfacial contribution to Δp_s. C12 thus compensates for several interacting variables, including an internal physics-based feedback loop within the slurry-steam environment. While we demonstrate Smart WAVE atomization for pronounced (orders of magnitude) viscosity changes, it is broadly designed to achieve consistent, reliable atomization for viscous, non-Newtonian slurries with any temporal property changes.

The initial proof-of-concept (Test 1) demonstrated the necessity and efficacy of the coupled controller system. An additional benefit of C2 is providing for flexibility with steam usage: rather than a fixed (and potentially excessive) steam flow rate, steam is only used as necessary to keep droplet sizes at setpoint. A comparison of meshes showed that general atomization characteristics remain largely unchanged through refinement, even though droplet size decreases. Adding a porous media section in the slurry annulus (Test 2) significantly increased the sensitivity of pressure drop to viscosity, resulting in an initial 5000% pressure drop increase for a 100x increase in viscosity. The pressure drop showed a similar sensitivity to viscosity with the non-Newtonian slurry in Test 3. Because of this high sensitivity and the resulting reduction in slurry flow rate, the system's atomization characteristics changed drastically. Small droplets being stripped off kept the SMD below setpoint and caused the steam flow to bottom out near zero.

As presented, Smart was mesh-independent and multiphase physics-independent; however, there is room for improvement. In the future, we note the need for variable controller gains, perhaps using fuzzy logic, as the relationship between measured and controlled variables changed during Test 3. A third control knob might also improve results for the Test 3 scenario. Though SMD proved to be a sufficient single metric for atomization quality, other droplet size statistics could replace SMD as a measured variable.

CHAPTER SIX

CONCLUSION

We have presented a series of studies on WAVE atomization, detailing its associated mechanisms, instabilities, and characteristics. We have also presented a study on the response of WAVE to Smart atomization through a sudden pronounced shift in viscosity. Both WAVE and Smart are new concepts that have never been studied before. WAVE uses a novel injector design with a low GLR of 2.7%; the conventional outer gas flow and inner liquid flow is reversed, providing an annular wave bool and beach region before the nozzle exit. The resulting periodic wave formation and bulk transonic pulsation are characteristic of the system, the central feature being high-blockage ratio waves that augment the slurry heating and disintegration process in a transonic flow. The cold working fluid in these studies is banana puree, for which the viscosity is temperature- and shear-thinning and described by the Herschel-Bulkley model, and steam is the hot assisting gas. However, WAVE is broadly designed for atomization of viscous, non-Newtonian slurries. Smart improves upon basic WAVE atomization by providing a mechanism to account for dynamically changing slurry properties, particularly viscosity. The Smart system could provide efficient and consistent atomization for gelled propellants or manure slurries for energy conversion. Each of the following paragraphs summarizes major points from one of the four studies (Chapters II-V).

Chapter II focused on wave formation inside the nozzle. Waves with a high blockage ratio form periodically at a frequency of 1000 Hz, where the collapse of one wave corresponds to the formation of another (i.e., no wave train). Wave formation and collapse occur at very regular intervals, while instabilities result in distinctly unique waves each cycle. The average wave angle and wavelength are 50° and 0.7 nozzle diameters, respectively. Annular injection of the cold slurry into the hot steam channel provides a wave pool, allowing KHI to deform the surface; then, steam shear and acceleration from decreased flow area lift the newly formed wave. The onset of flow separation appears to occur as the waves' rounded geometry transitions to a more pointed shape. Steam compression caused by wave sheltering increases pressure and temperature on the windward side of the wave, forcing both pressure and temperature to cycle with wave frequency. Wave growth peaks at the nozzle exit, at which point the pressure build-up overcomes inertia and surface tension to collapse and disintegrate the wave. Truncation of wave life by pressure build-up and shear-induced slurry viscosity reduction is a prominent feature of the system. The wave birth-death process creates bulk system pulsation, which in turn affects wave formation.

Chapter III focused on atomization as dictated by wave-induced mechanisms. The pulsing slurry flow develops with three distinct stages: stretch, bulge, and burst, leading to an annular slurry sheet stretching down from the nozzle exit. Rayleigh-Taylor instabilities and viscosity gradients destabilize the surface. During wave collapse, the slurry sheet bulges radially outward and ruptures violently in a radial burst. Near-nozzle dynamics propagate axially as periodic Sauter mean diameter fluctuations in a wave pattern. Three atomization mechanisms have been revealed in simulations: 1) wave impact momentum, 2) pressure buildup, 3) and droplet breakaway. Waves collapse into the slurry sheet with a radial momentum flux of 1.7×10^5 kg/m-s^2, and wave-induced pressure buildup creates a large pressure gradient across the slurry sheet. Both contribute to the rupture of the slurry sheet. The third mechanism is driven by cold slurry penetration deep into the hot steam flow, where increased steam-slurry interaction results in bundles of small droplets breaking away from each wave.

Chapter IV focused on spatiotemporal characteristics of WAVE atomization and the onset of three-dimensional instabilities. A closer study of wave disintegration revealed that droplet production inside the nozzle is enhanced by ligaments radially flicking up from the slurry wave into the steam flow with radial:axial velocity ratios exceeding 0.5. The wave also leaves residual ligaments in its wake, which facilitate further disintegration. Effervescence is introduced as hold steam penetrates the cold wave and again as steam is sandwiched between the slurry sheet and the crashing wave. After birth, a wave spends 80% of the wave cycle period building up to peak height at the nozzle exit. Baroclinic torque drives the development of Rayleigh-Taylor instabilities and reaches values on the order of 1×10^{13} 1/s^2. Velocities inside the nozzle (wave formation region) are generally azimuthally similar (two-dimensional), but those outside the nozzle (radial bursting region) are azimuthally uncorrelated (three-dimensional). Inter-variable correlations show significant decoupling of quantities beyond the nozzle exit, and local strain rate fluctuations were found to correlate particularly well with bulk system pulsation. Although adaptive mesh refinement (AMR) can provide computationally efficient resolution of gas-liquid interfaces, this technique produced different results than an equivalent non-dynamic mesh when modeling WAVE. Gradients were particularly affected by AMR, and turbulent kinetic energy showed differences greater than 150% outside the nozzle.

Chapter V focused on testing and demonstration of Smart atomization to maintain consistent atomization through drastic step changes in slurry properties with the WAVE process. Two PID controllers were employed to maintain consistent slurry atomization and pumping demands. The first adjusts cold slurry flow based on pressure drop, and the second modulates hot steam flow based on droplet size. Though their algorithms are separate, it was shown that the controller actions are unavoidably linked due to the interrelated physics of pressure drop, droplet size, flow rates, and steam density. A series of three progressively rigorous tests revealed the capabilities of the current Smart system. During controller compensation, slurry and steam flows were significantly altered and drastically changed atomization characteristics, which may or may not be advantageous. Despite this, controller objectives were maintained through a 100-fold increase in slurry viscosity. To avoid unnecessary steam use, which could reduce overall process efficiency (in the case of waste incineration, for example), the second controller provides the flexibility to only use what assisting gas is required to maintain atomization quality. Though algorithmic improvements are encouraged, the control methodology was shown to be mesh-independent and to operate across multiple atomization regimes.

REFERENCES

1 Nick Pizzo, Luc Deike and Alex Ayet, "How does the wind generate waves?" Physics Today 74 (11), 38-43 (2021).

2 Harold Jeffreys, "On the Formation of Water Waves by Wind," Proceedings of the Royal Society of London. Series A, Containing Papers of a Mathematical and Physical Character 107 (742), 189-206 (1925).

3 John W. Miles, "On the generation of surface waves by shear flows," Journal of Fluid Mechanics 3 (2), 185-204 (1957).

4 O. M. Phillips, "On the generation of waves by turbulent wind," Journal of Fluid Mechanics 2 (5), 417-445 (1957).

5 Erin L. Hult, Cary D. Troy and Jeffrey R. Koseff, "Laboratory images of breaking internal waves," Physics of Fluids 18 (9), 091107 (2006).

6 G. K. Pedersen *et al.*, "Runup and boundary layers on sloping beaches," Physics of Fluids 25 (1), 012102 (2013).

7 Markus Dauth and Nuri Aksel, "Breaking of waves on thin films over topographies," Physics of Fluids 30 (8), 082113 (2018).

8 Kuang-An Chang and Philip L. -F Liu, "Experimental investigation of turbulence generated by breaking waves in water of intermediate depth," Physics of Fluids 11 (11), 3390-3400 (1999).

9 Gang Chen *et al.*, "Two-dimensional Navier–Stokes simulation of breaking waves," Physics of Fluids 11 (1), 121-133 (1999).

10 Chang (林呈) Lin *et al.*, "Novel similarities in the free-surface profiles and velocities of solitary waves traveling over a very steep beach," Physics of Fluids 32 (8), 083601 (2020).

11 S. Millet *et al.*, "Wave celerity on a shear-thinning fluid film flowing down an incline," Physics of Fluids 20 (3), 031701 (2008).

12 N. J. Balmforth, R. V. Craster and C. Toniolo, "Interfacial instability in non-Newtonian fluid layers," Physics of Fluids 15 (11), 3370-3384 (2003).

13 E. Mogilevskiy, "Stability of a non-Newtonian falling film due to three-dimensional disturbances," Physics of Fluids 32 (7), 073101 (2020).

14 Sumit Tripathi *et al.*, "Lubricated Transport of Highly Viscous Non-newtonian Fluid as Core-annular Flow: A CFD Study," Procedia IUTAM 15, 278-285 (2015).

15 Sergey V. Alekseenko *et al.*, "Study of formation and development of disturbance waves in annular gas–liquid flow," International Journal of Multiphase Flow 77, 65-75 (2015).

16 Mikhail V. Cherdantsev *et al.*, "Development and interaction of disturbance waves in downward annular gas-liquid flow," International Journal of Multiphase Flow 138, 103614 (2021).

17 Wayne Strasser, "Towards Atomization for Green Energy: Viscous Slurry Core Disruption by Feed Inversion," AAS 31 (6), 23-43 (2021).

18 Daniel M. Wilson and Wayne Strasser, "Smart Atomization: Implementation of PID Control in Biosludge Atomizer," 5-6th Thermal and Fluids Engineering Conference , (2021).

19 D. M. Wilson and W. Strasser, "A Spray of Puree: Wave-Augmented Transonic Airblast Non-Newtonian Atomization," Physics of Fluids 34 (7), (2022).

20 D. M. Wilson, W. Strasser and R. Prichard, "Spatiotemporal Characterization of Wave-Augmented Varicose Explosions," International journal of multiphase flow 161, 104352 (2023).

21 M. Lagha *et al.*, "A numerical study of compressible turbulent boundary layers," Physics of Fluids 23 (1), 015106 (2011).

22 Akanksha Baranwal, Diego A. Donzis and Rodney D. W. Bowersox, "Asymptotic behaviour at the wall in compressible turbulent channels," Journal of Fluid Mechanics 933, (2022).

23 Suhas V. Patankar, Numerical Heat Transfer and Fluid Flow, edited by Anonymous 1st ed. (CRC Press, London, 1980), .

24 Wayne Strasser and Francine Battaglia, "Identification of Pulsation Mechanism in a Transonic Three-Stream Airblast Injector," Journal of Fluids Engineering 138 (11), (2016).

25 David Youngs, Time-Dependent Multi-material Flow with Large Fluid Distortion, in Numerical Methods in Fluid Dynamics, edited by K. W. Morton and M. J. Baines, (Academic Press, 1982), pp. 273-285.

26 Wayne Strasser and Francine Battaglia, "The effects of pulsation and retraction on non-Newtonian flows in three-stream injector atomization systems," Chemical Engineering Journal 309, 532-544 (2017).

27 Wayne Strasser and Francine Battaglia, "The Influence of Retraction on Three-Stream Injector Pulsatile Atomization for Air–Water Systems," Journal of Fluids Engineering 138 (11), (2016).

28 Wayne Strasser, "Towards the optimization of a pulsatile three-stream coaxial airblast injector," International Journal of Multiphase Flow 37 (7), 831-844 (2011).

29 Wayne Strasser, "Oxidation-assisted pulsating three-stream non-Newtonian slurry atomization for energy production," Chemical Engineering Science 196, 214-224 (2019).

30 Wayne Strasser, Francine Battaglia and Keith Walters, "Application of a Hybrid RANS-LES CFD Methodology to Primary Atomization in a Coaxial Injector," Volume 7A: Fluids Engineering Systems and Technologies , (2015).

31 Wayne Strasser and Francine Battaglia, "The Effects of Prefilming Length and Feed Rate on Compressible Flow in a Self-Pulsating Injector ," AAS 27 (11), (2017).

32 W. Strasser and F. Battaglia, "Pulsating Slurry Atomization, Film Thickness, and Azimuthal Instabilities," Atomization and Sprays 28 (7), 643-672 (2018).

33 Wayne Strasser, "The war on liquids: Disintegration and reaction by enhanced pulsed blasting," Chemical Engineering Science 216, 115458 (2020).

34 Alan George Wonders, Howard Wood Jenkins Jr, Lee Reynolds Partin, Wayne Scott Strasser, Marcel De Vreede, US Patent No. 7589231 2009).

35 Santanu Kumar Sahoo and Hrishikesh Gadgil, "Large scale unsteadiness during self-pulsation regime in a swirl coaxial injector and its influence on the downstream spray statistics," International journal of multiphase flow 149, 103944 (2022).

36 Wayne Strasser, "Toward Atomization for Green Energy: Viscous Slurry Core Disruption by Feed Inversion," AAS 31 (6), (2021).

37 Manisha B. Padwal and D. P. Mishra, "Effect of Air Injection Configuration on the Atomization of Gelled Jet A1 Fuel in an Air-Assist Internally Mixed Atomizer ," Atomization and Sprays 23 (4), 327-341 (2013).

38 Cynthia Ditchfield *et al.*, "Rheological Properties of Banana Puree at High Temperatures," International Journal of Food Properties 7 (3), 571-584 (2004).

39 J. H. Tsen, 金安兒 and V. A. E. King, "Density of banana puree as a function of soluble solids concentration and temperature," Journal of Food Engineering 55 (4), 305-308. (2002).

40 W. Mostert, S. Popinet and L. Deike, "High-resolution direct simulation of deep water breaking waves: transition to turbulence, bubbles and droplets production," Journal of fluid mechanics 942 (A27), (2022).

41 Reid Prichard and Wayne Strasser, "Optimizing Selection and Allocation of High-Performance Computing Resources for Computational Fluid Dynamics," 7th Thermal and Fluids Engineering Conference (under review) , (2022).

42 W. H. R. Chan *et al.*, "Formation and dynamics of bubbles in breaking waves: Part II. The evolution of the bubble size distribution and breakup/coalescence statistics," Center for Turbulence Research , (2018).

43 Todd A. Oliver *et al.*, "Estimating uncertainties in statistics computed from direct numerical simulation," Physics of fluids (1994) 26 (3), (2014).

44 Alberto Vela-Martín and Marc Avila, "Deformation of drops by outer eddies in turbulence," Journal of Fluid Mechanics 929, (2021).

45 Abhijeet Kumar and Srikrishna Sahu, "Large scale instabilities in coaxial air-water jets with annular air swirl," Physics of Fluids 31 (12), 124103 (2019).

46 Kiumars Khani Aminjan *et al.*, "Study of pressure-swirl atomizer with spiral path at design point and outside of design point," Physics of Fluids 33 (9), 093305 (2021).

47 Shirin Patil and Srikrishna Sahu, "Air swirl effect on spray characteristics and droplet dispersion in a twin-jet crossflow airblast injector," Physics of Fluids 33 (7), 073314 (2021).

48 Erkki Laurila *et al.*, "Numerical study of bubbly flow in a swirl atomizer," Physics of Fluids 32 (12), 122104 (2020).

49 Mayukhmali Chakraborty, Aravind Vaidyanathan and S. L. N. Desikan, "Experiments on atomization and spray characteristics of an effervescent strut injector," Physics of Fluids 33 (1), 017103 (2021).

50 Chenwei (张宸玮) Zhang *et al.*, "Atomization of misaligned impinging liquid jets," Physics of Fluids 33 (9), 093311 (2021).

51 Aisha Qi, Leslie Y. Yeo and James R. Friend, "Interfacial destabilization and atomization driven by surface acoustic waves," Physics of Fluids 20 (7), 074103 (2008).

52 J. M. Meacham *et al.*, "Droplet formation and ejection from a micromachined ultrasonic droplet generator: Visualization and scaling," Physics of Fluids 17 (10), 100605 (2005).

53 Georgios Charalampous, Constantinos Hadjiyiannis and Yannis Hardalupas, "Proper orthogonal decomposition of primary breakup and spray in co-axial airblast atomizers," Physics of Fluids 31 (4), 043304 (2019).

54 Hao (武浩) Wu, Fujun (张付军) Zhang and Zhenyu (章振宇) Zhang, "Droplet breakup and coalescence of an internal-mixing twin-fluid spray," Physics of Fluids 33 (1), 013317 (2021).

55 Abhijeet Kumar and Srikrishna Sahu, "Liquid jet disintegration memory effect on downstream spray fluctuations in a coaxial twin-fluid injector," Physics of Fluids 32 (7), 073302 (2020).

56 Y. Ling *et al.*, "A two-phase mixing layer between parallel gas and liquid streams: multiphase turbulence statistics and influence of interfacial instability," Journal of fluid mechanics 859, 268-307 (2019).

57 Hui Zhao *et al.*, "Secondary breakup of coal water slurry drops," Physics of Fluids 23 (11), 113101 (2011).

58 Jin-Peng (郭瑾朋) Guo *et al.*, "Instability breakup model of power-law fuel annular jets in slight multiple airflows," Physics of Fluids 32 (9), 094109 (2020).

59 Li-jun Yang *et al.*, "Linear Stability Analysis of a Non-Newtonian Liquid Sheet," Journal of propulsion and power 26 (6), 1212-1225 (2010).

60 Manisha B. Padwal and Debi Prasad Mishra, "Performance of Two-Fluid Atomization of Gel Propellant," Journal of propulsion and power 38 (1), 30-39 (2022).

61 Manisha B. Padwal and D. P. Mishra, "Interactions among synthesis, rheology, and atomization of a gelled propellant," Rheol Acta 55 (3), 177-186 (2016).

62 D. M. Wilson and W. Strasser, "The Rise and Fall of Banana Puree: Non-Newtonian Annular Wave Cycle in Transonic Self-Pulsating Flow," Physics of Fluids 34 (7), (2022).

63 M. Pilch and C. A. Erdman, "Use of breakup time data and velocity history data to predict the maximum size of stable fragments for acceleration-induced breakup of a liquid drop," International Journal of Multiphase Flow 13 (6), 741 (1987).

64 Grant B. Deane and M. Dale Stokes, "Scale dependence of bubble creation mechanisms in breaking waves," Nature 418 (6900), 839-844 (2002).

65 Santanu Kumar Sahoo and Hrishikesh Gadgil, "Dynamics of Self-Pulsation in Gas-Centered Swirl Coaxial Injector: An Experimental Study," Journal of Propulsion and Power 37 (3), 450-462 (2021).

66 Sergey V. Alekseenko *et al.*, "Study of formation and development of disturbance waves in annular gas–liquid flow," International Journal of Multiphase Flow 77, 65-75 (2015).

67 Subramanian Easwaran Iyer *et al.*, "Methods and apparatus for coating substrates," US Patent 8734909 , (2014).

68 G. Seropian, A. C. Rust and R. S. J. Sparks, "The Gravitational Stability of Lenses in Magma Mushes: Confined Rayleigh-Taylor Instabilities," Journal of geophysical research. Solid earth 123 (5), 3593-3607 (2018).

69 P. K. Senecal *et al.*, "Modeling high-speed viscous liquid sheet atomization," International journal of multiphase flow 25 (6), 1073-1097 (1999).

70 Yue Ling *et al.*, "Spray formation in a quasiplanar gas-liquid mixing layer at moderate density ratios: A numerical closeup," Physical review fluids 2 (1), (2017).

71 Shin-Yee Wong, Weibiao Zhou and Jinsong Hua, "Designing process controller for a continuous bread baking process based on CFD modelling," Journal of food engineering 81 (3), 523-534 (2007).

72 Jumoke Oladejo *et al.*, "A Review of Sludge-to-Energy Recovery Methods," Energies (Basel) 12 (1), 60 (2018).

73 Zong Liu *et al.*, "Centrifuge separation effect on bacterial indicator reduction in dairy manure," Journal of environmental management 191, 268-274 (2017).

74 Masataka Arai, "The Possibility of Active Attitude Control for Fuel Spray," Engineering 5 (3), 519-534 (2019).

75 C. M. Jones, J. G. Lee and D. A. Santavicca, "Closed-Loop Active Control of Combustion Instabilities Using Subharmonic Secondary Fuel Injection," Journal of propulsion and power 15 (4), 584-590 (1999).

76 ADAM COKER *et al.*, "Active Instability Control Effectiveness in a Liquid Fueled Combustor," Combustion science and technology 178 (7), 1251-1261 (2006).

77 T. Conrad *et al.*, "Feasibility of “intermittent” active control of combustion instabilities in liquid fueled combustors using a “smart” fuel injector," Proceedings of the Combustion Institute 31 (2), 2223-2230 (2007).

78 Rodrigo Osuna-Orozco *et al.*, "Feedback Control of Coaxial Atomization Based on The Spray Liquid Distribution," Atomization and sprays 29 (6), 545-551 (2019).

79 Rodrigo Osuna-Orozco *et al.*, "Feedback Control of The Spray Liquid Distribution of Electrostatically Assisted Coaxial Atomization," AAS 30 (1), (2020).

80 Eric M. Turman and P. E. Wayne Strasser, "Leveraging Fuzzy Logic PID Controllers for Accelerating Chemical Reactor CFD," Chemical engineering science 262, 118029 (2022).